ELECTRIFICATION OF DIESEL-BASED POWERTRAINS FOR HEAVY VEHICLES

by

Tyler Swedes

A Thesis

Submitted to the Faculty of Purdue University

In Partial Fulfillment of the Requirements for the degree of

Master of Science in Mechanical Engineering

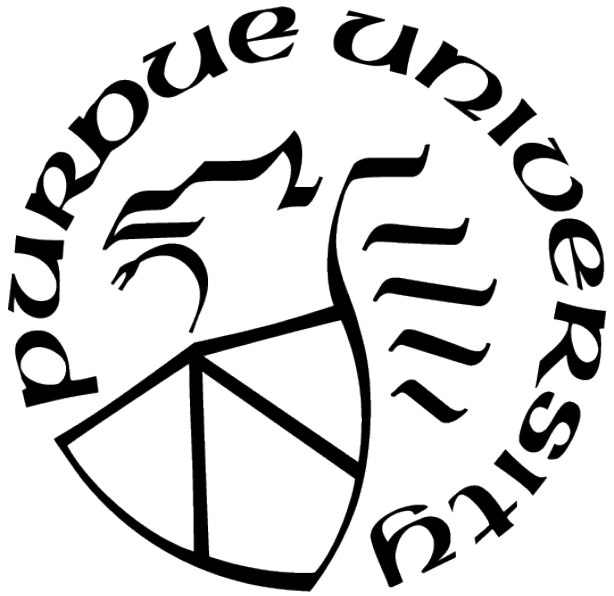

School of Mechanical Engineering

West Lafayette, Indiana

August 2021

THE PURDUE UNIVERSITY GRADUATE SCHOOL
STATEMENT OF COMMITTEE APPROVAL

Dr. Greg Shaver, Chair

School of Mechanical Engineering

Dr. Peter Meckl

School of Mechanical Engineering

Dr. Oleg Wasynczuk

School of Electrical and Computer Engineering

Approved by:

Dr. Nicole L. Key

To my parents, Dave and Carmen Swedes, and my brother, Christopher Swedes.

ACKNOWLEDGMENTS

I would like to thank the Lord for being my foundation and constant source of hope, and my parents for their love, support, and encouragement in every part of my life. I also want to recognize my advisor, Dr. Greg Shaver, especially for his guidance in academia and in transitioning to industry, as well as Dr. Oleg Wasynczuk and Dr. Peter Meckl for their instruction both in the classroom and in research. Finally I want to thank my colleagues in Dr. Shaver's research group for their friendship and their help in completing my work, especially Harsha Rayasam, Weijin Qui, Chisom Emegoakor, and Shubham Agnihotri.

TABLE OF CONTENTS

LIST OF TABLES

LIST OF FIGURES

LIST OF SYMBOLS

A	Area
A, B, C, D, F	Linear State Space System Matrices
a	Acceleration (Chapter 2 - hybrid electric powertrain)
a	Regression Fit Constants (Chapter 3 & 4 - engine modeling)
B	Bore Diameter (Chapter 3 & 4 - engine modeling)
C_{d}	Vehicle Drag Coefficient (Chapter 2 - hybrid electric powertrain)
C_{d}	Discharge Coefficient (Chapters 3 & 4 - engine modeling)
C_{eng}	Engine Torque Coefficient (Chapters 3 & 4 - engine modeling)
C	capacitance (Chapter 2 - hybrid electric powertrain)
c_{p}	Constant Pressure Specific Heat
Λ	Relative Gain Array Matrix (Chapters 3 & 4 - engine modeling)
d	Diameter
γ	Specific Heat Ratio
E	Energy
F	Fraction
G	Transfer Function
h	Elevation (Chapter 2 - hybrid electric powertrain)
h	Convective Heat Transfer Coefficient (Chapters 3 & 4 - engine modeling)
η	Efficiency (Chapters 3 & 4 - engine modeling)
I	Inertia
m	Mass
μ	Rolling Resistance Coefficient (Chapter 2 - hybrid electric powertrain)
N_{cyl}	Number of Cylinders (Chapters 3 & 4 - engine modeling)
N_{red}	Reduced Engine Speed (Chapters 3 & 4 - engine modeling)
q	Mass Specific Heat Transfer Rate (Chapters 3 & 4 - engine modeling)
P	Power (Chapter 2 - hybrid electric powertrain)
P	Pressure (Chapters 3 & 4 - engine modeling)
θ	Grade angle (Chapter 2 - hybrid electric powertrain)

R	Mass specific gas constant
ρ	Density
S	Cylinder Stroke Length (Chapter 3 & 4 - engine modeling)
S_{p}	Mean Engine Speed (Chapter 3 & 4 - engine modeling)
s	Complex Variable (Chapter 3 & 4 - engine modeling)
T	Temperature
$\mathcal{T}$	Time Constant
t	Time
τ	Time (Chapter 2 - hybrid electric powertrain)
τ	Torque (Chapters 3 & 4 - engine modeling)
u	State Input (Chapters 3 & 4 - engine modeling)
V	Voltage (Chapter 2 - hybrid electric powertrain)
V	Volume (Chapters 3 & 4 - engine modeling)
v	Speed
W	Flow Rate (Chapters 3 & 4 - engine modeling)
w	Average Cylinder Gas Velocity (Chapters 3 & 4 - engine modeling)
ω	Shaft Speed
ω	Frequency
x	Distance Travelled (Chapter 2 - hybrid electric powertrain)
x	State Variable (Chapter 3 - engine modeling)
y	State Input (Chapters 3 & 4 - engine modeling)
Z	Power (Chapters 3 & 4 - engine modeling)

ABBREVIATIONS

AFR	Air-Fuel Ratio
aero	Aerodynamic (subscript)
amb	Ambient conditions (subscript)
bat	Battery (subscript)
bd	Blowdown (subscript)
bv	Bypass Valve (subscript)
BMS	Battery Management System
BSFC	Brake Specific Fuel Consumption
CAC	Charge Air Cooler
comp	Compressor (subscript)
compis	Compressor interstage (subscript)
cyl	Cylinder Inlet (subscript)
cylout	Cylinder Outlet (subscript)
ECM	Engine Control Module
ECR	Effective Compression Ratio
EGR	Exhaust Gas Recirculation
EOC	End of Combustion
EVO	Exhaust Valve Opening
em	Exhaust Manifold (subscript)
et	Exhaust Throttle (subscript)
ex	Exhaust (subscript)
FFT	Fast Fourier Transform
gen	Generator (subscript)
GPS	Global Positioning System
GVW	Gross Vehicle Weight
IC	Internal Combustion
im	Intake Manifold (subscript)
LHV	Lower Heating Value

MIMO	Multi-Input Multi-Output (control method)
mot	Motor (subscript)
PR	Pressure Ratio
regen	Regenerative Braking (subscript)
RGA	Relative Gain Array
rpm	Revolutions per Minute
rr	Rolling Resistance (subscript)
SISO	Single-Input Single-Output (control method)
SOC	Battery State of Charge
tc	Turbocharger (subscript)
TDC	Top Dead Center
turb	Turbine (subscript)
VFD	Variable Frequency Drive
wg	Wastegate (subscript)

ABSTRACT

In recent decades as environmental concerns and the cost and availability of fossil fuels have become more pressing issues, the need to extract more work from each drop of fuel has increased accordingly. Electrification has been identified as a way to address these issues in vehicles powered by internal combustion engines, as it allows existing engines to be operated more efficiently, reducing overall fuel consumption. Two applications of electrification are discussed in the work presented: a series-electric hybrid powertrain from an on-road class 8 truck, and an electrically supercharged diesel engine for use in the series hybrid power system of a wheel loader.

The first application is an experimental powertrain developed by a small start-up company for use in highway trucks. The work presented in this thesis shows test results from routes along (1) Interstate 75 between Florence, KY, and Lexington, KY, and (2) Interstates 74 and 70 east of Indianapolis, during which tests the startup collected power flow data from the vehicle's motor, generator, and battery, and three-dimensional position data from a GPS system. Based on these data, it was determined that the engine-driven generator provided an average of 15% more propulsive energy than required due to electrical losses in the drivetrain. Some of these losses occured in the power electronics, which are shown to be 82% - 92% efficient depending on power flow direction, but the battery showed significant signs of wear, accounting for the remainder of these electrical losses. Overall, most of the system's fuel savings came from its regenerative braking capability, which recaptured between 3% and 12% of the total drive energy output. Routes with significant grade changes maximize this energy recapture percentage, but it is shown minimizing drag and rolling resistance with a more modern truck and trailer could further increase this energy capture to between 8% and 18%.

In the second application, an electrified air handling system is added to a 4.5L engine, allowing it to replace the 6.8L engine in John Deere's 644K hybrid wheel loader. Most of the fuel savings arise from downsizing the engine, so in this case an electrically driven supercharger (eBooster) allows the engine to meet the peak torque requirements of the larger, original engine. In this thesis, a control-oriented nonlinear state space model of the modified

4.5L engine is presented and linearized for use in designing a robust, multi-input multi-output (MIMO) controller which commands the engine's fueling rate, eBooster, eBooster bypass valve, exhaust gas recirculation (EGR) valve, and exhaust throttle. This integrated control strategy will ultimately allow superior tracking of engine speed, EGR fraction, and air-fuel ratio (AFR) targets, but these performance gains over independent single-input single-output control loops for each component demand linear models that accurately represent the engine's gas exchange dynamics. To address this, a physics-based model is presented and linearized to simulate pressures, temperatures, and shaft speeds based on sub-models for exhaust temperature, cylinder charge flow, valve flow, compressor flow, turbine flow, compressor power, and turbine power. The nonlinear model matches the truth reference engine model over the 1200 rpm - 2000 rpm and 100 Nm - 500 Nm speed and torque envelope of interest within 10% in steady state and 20% in transient conditions. Two linear models represent the full engine's dynamics over this speed and torque range, and these models match the truth reference model within 20% in the middle of the operating envelope. However, specifically at (1) low load for any speed and (2) high load at high speed, the linear models diverge from the nonlinear and truth reference models due to nonlinear engine dynamics lost in linearization. Nevertheless, these discrepancies at the edges of the engine's operating envelope are acceptable for control design, and if greater accuracy is needed, additional linear models can be generated to capture the engine's dynamics in this region.

1. INTRODUCTION

1.1 Motivation

In recent decades as environmental concerns and the cost and availability of fossil fuels have become more pressing issues, the need to extract more work from each drop of fuel has increased accordingly. In the on- and off-road commercial vehicle space, no energy source has been identified which can match diesel fuel's energy density, ease of distribution, and ubiquity, so at least for the near term, development efforts have focused on reducing the amount of fuel required to do the same total work.

Electrification has emerged as one way to reduce total fuel consumption in vehicles powered by internal combustion (IC) engines, because electrical systems allow the designer to distance the engine from the inherently non-steady operational profile that characterizes commercial vehicles' power requirements. IC engines, and specifically compression ignition engines, can produce power over a wide range of speeds, which initially suited them for vehicles which operate over a wide speed range, but their efficiency "sweet spot" which maximizes the energy extracted per unit mass of fuel is a much narrower range of speeds and torques. As a result, significant fuel savings can be realized by selecting an engine that meets a vehicle's average power requirement when operating in its sweet spot where brake specific fuel consumption (BSFC) is minimized. However, an engine selected this way typically cannot meet a vehicle's peak transient power requirements, so the electrical system provides additional assistance, allowing the complete electrified powertrain package to output sufficient power.

The commercial vehicle industry has successfully employed a variety of electrified drivetrains, but two common approaches are series-electric powertrain hybridization and engine air handling electrification. Series-electric powertrains are particularly popular, because they eliminate the mechanical connection between the engine and drive wheels, they are relatively simple to understand and design, and they allow braking energy that would normally be lost in friction brakes to be recaptured. Electrified air handling systems are also straightforward to implement, because electrically driven compression stages can typically be bolted onto existing engines to increase torque output, and they typically require smaller, lower voltage

electrical systems than those used in full hybrid drivetrains. As a result, these systems are typically employed to allow smaller engines to replace larger, less efficient engines without sacrificing power output. However, both approaches can reduce the fuel quantity necessary to meet a given drivetrain's required power output.

1.2 Summary and Objectives of Work Presented

The work presented in this thesis covers two distinct applications of hybrid powertrains in commercial vehicles:

Application 1: The first application is a series electric hybrid class 8 truck designed and built by a small startup company to provide fuel efficiency gains on a highway drive cycle. The work on this application, presented in Chapter 2, builds on the results discussed in [1] with objectives of (1) confirming that electrical components operate as expected, (2) identifying the mechanisms through which the hybrid drivetrain can provide efficiency improvements over a conventional drivetrain, and (3) demonstrating that potential efficiency improvements from a hybrid drivetrain on a highway drive cycle are significant enough to merit further development. The modeling and analysis toward objectives 2 and 3 was conducted in cooperation with Shubham Agnihotri, so this work is omitted, but the results are summarized briefly in Section 2.5.

Application 2: The second application is a diesel engine with an electrically driven supercharger for a John Deere 644K hybrid wheel loader. The objective of the work on this application, presented in Chapters 3 and 4, is to develop a mean-value, control oriented, linear state space model of the engine's gas exchange dynamics which can be used in robust, multi-input multi-output controller development. The controller design is beyond the scope of this thesis distribution, but its purpose is to allow coordinated control of the electric supercharger, valves in the air handling system, and fueling rate to track engine speed, exhaust gas recirculation fraction, and air-fuel ratio targets.

1.3 Background and Literature Review

The automotive industry has implemented numerous hybrid electric drivetrain configurations, but all architectures feature a conventional internal combustion (IC) engine, at least one electric machine, and an optional electrical energy storage device in the form of batteries or capacitors. With the exception of plug-in hybrids, all hybrid electric vehicles still rely on the IC engine to be the source of energy in the powertrain, but the electric machine(s) provide efficiency gains by allowing the engine's operation to be optimized. Additionally, depending on the configuration, an electric machine can act as a generator to recapture braking energy that would otherwise escape as heat through the friction brakes.

1.3.1 Series Electric Hybrid Powertrain Description

Hybrid drivetrains can be grouped by basic configuration into parallel and series architectures. In its most basic form, a parallel hybrid drivetrain mechanically connects both the engine and electric machine to the wheels, effectively summing the electric machine and IC engine output to meet the vehicle's mechanical power requirements. This configuration minimizes the number of electrical components and allows a smaller engine and motor to be used, but it also requires a complex control system and mechanical linkage to implement [2].

In a series hybrid powertrain, shown in Figure 1.1, no mechanical linkage exists between the engine and the wheels. This means that the motor must be sized to meet the vehicle's mechanical power requirements alone, but the IC engine operation can be optimized much more readily, since engine operation is mechanically independent of the wheels. In this configuration, the generator, the battery, or both can provide electrical power to the motor while driving, and the generator or the drive motor can charge the battery.

Additionally, because this architecture is straightforward to understand, analyze, and control, it accomodates a wide range of battery and engine sizes. For example, vehicles with small batteries or even ultracapacitors can use the engine to supply most of the tractive power. This minimizes battery weight and wear, but requires the engine to supply most of the vehicle's transient power requirements. Alternatively, a large battery which can meet most of the vehicle's power requirement allows a smaller engine to be selected which primarily

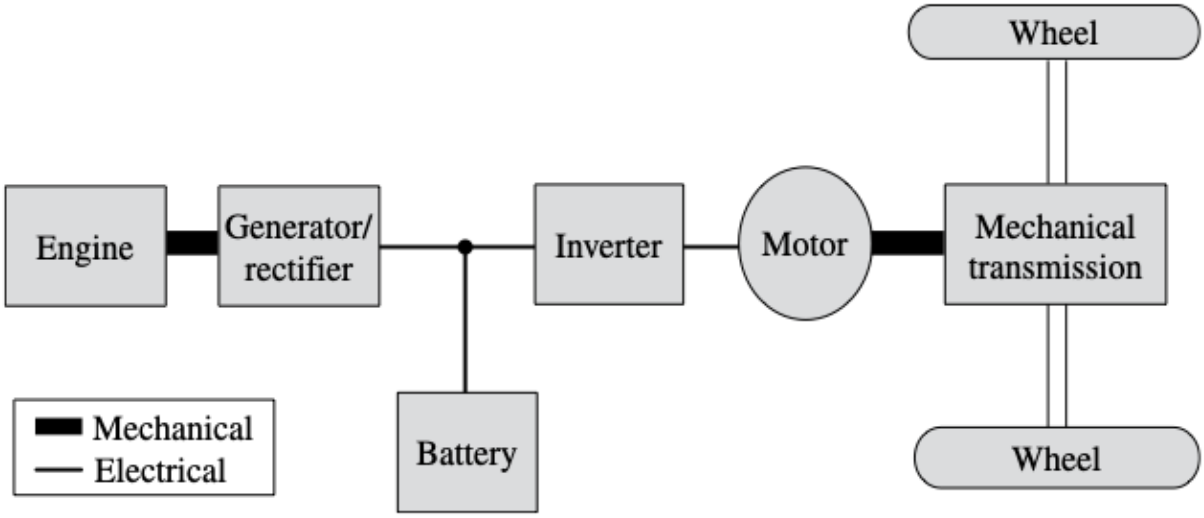

Figure 1.1. Series hybrid powertrain architecture.

charges the battery. This allows the engine and generator to operate as a genset, where the engine can operate almost entirely at its minimum BSFC point. Finally, for commercial vehicles, this system's mechanical simplicity and upgradability can allow longer vehicle life.

1.3.2 Fuel Savings Due to Hybridization of Class 8 Truck

The commercial vehicle industry has employed hybrid powertrains extensively in vehicles with highly transient drive cycles, such as off-road construction equipment, city busses, and delivery trucks, because electric motors can re-capture significant energy during the frequent braking events, and meet high transient power requirements, alleviating the need to use oversized, less efficient engines simply to meet the vehicle's power demand [3]. In contrast, little work been given to hybrid powertrains for on-highway class 8 trucks, because their drive cycle is inherently relatively steady with minimal speed and grade changes.

However, highway truck drive cycles do present some braking opportunities from mild highway grade changes, and because of class 8 trucks' significant mass, even brief or light braking events can recapture enough energy to reduce fuel consumption by at least 5% [1], [3], [4]. To explore the fuel economy improvement hybridization allows on highway truck routes in practice, a small startup company has designed and built a series electric hybrid

truck, which shows potential for significant fuel savings based from testing on Interstates 71 and 70 between Florence, Kentucky and Cambridge, Ohio. Fuel economy results from these initial tests are plotted in Figure 1.2 for several runs with the hybrid test vehicle (blue and red points) and one run with a conventionally powered truck (green point, test 3).

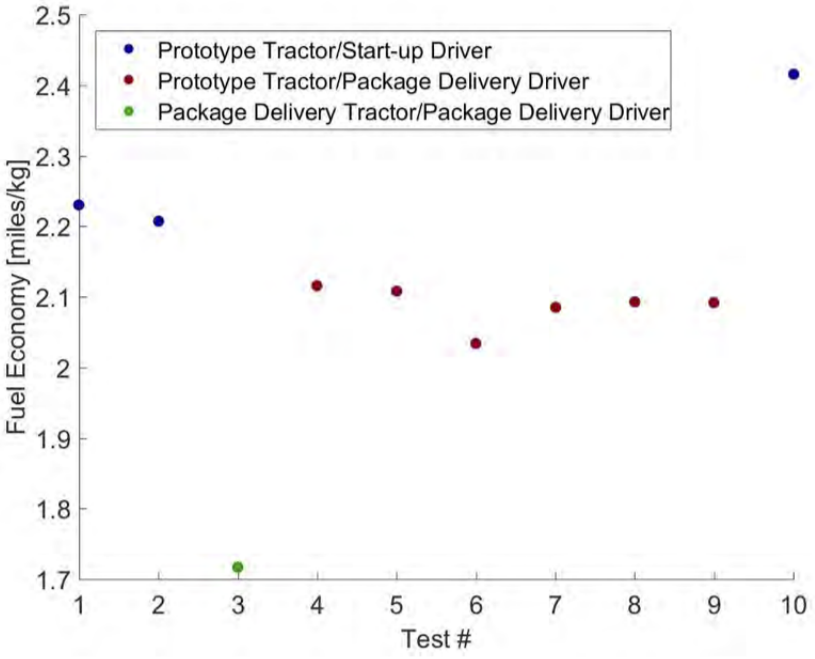

Figure 1.2. Average fuel economy over Florence-Cambridge route [1].

These results show a nearly 18% increase in fuel economy between the one test of the standard truck, and even the most inefficient test with the hybrid powertrain. However, gross vehicle weight and speed profile were not consistent among the tests conducted, the standard truck was driven at a much faster average speed than the hybrid truck, and the standard truck was a different model altogether from the platform used to build the hybrid vehicle. As a result, the effects of the hybrid powertrain alone on fuel economy cannot be concluded, because too many other factors varied among the tests.

A comparison study between a standard class 8 truck and the hybrid drivetrain was conducted using the the vehicle simulation software, Autonomie, but initial results showed that the experimental hybrid powertrain would actually be less efficient over the tested drive cycles. These results cannot be taken as conclusive however, because the supervisory

control method of controlling power flows in the vehicle was not known, and adjustments to the hybrid component sizes in Autonomie yielded 5% efficiency improvements over a standard powertrain for the tested drive cycles. Consequently, this work demonstrates that hybridization can allow efficiency gains over highway drive cycles, but due to inconsistent testing and a lack of power flow data from the hybrid drivetrain itself, no conclusions could be drawn about the experimental vehicle's efficiency gains over a standard class 8 truck.

1.3.3 Electrified Air Handling System Description

Hybrid powertrains can also be classified by "degree of hybridization", which is determined by the size of the electric motor and the vehicle's dependence on the electric machine for propulsion. A series electric hybrid for example can be considered a full hybrid, because the electric motor must provide all of the vehicle's tractive power requirement at any given instant. At the other end of the spectrum, an engine with an electrified air-handling system can be considered a type of micro hybrid, because the electrical part of the power train provides a boost to the engine, but cannot power the vehicle on its own [2].

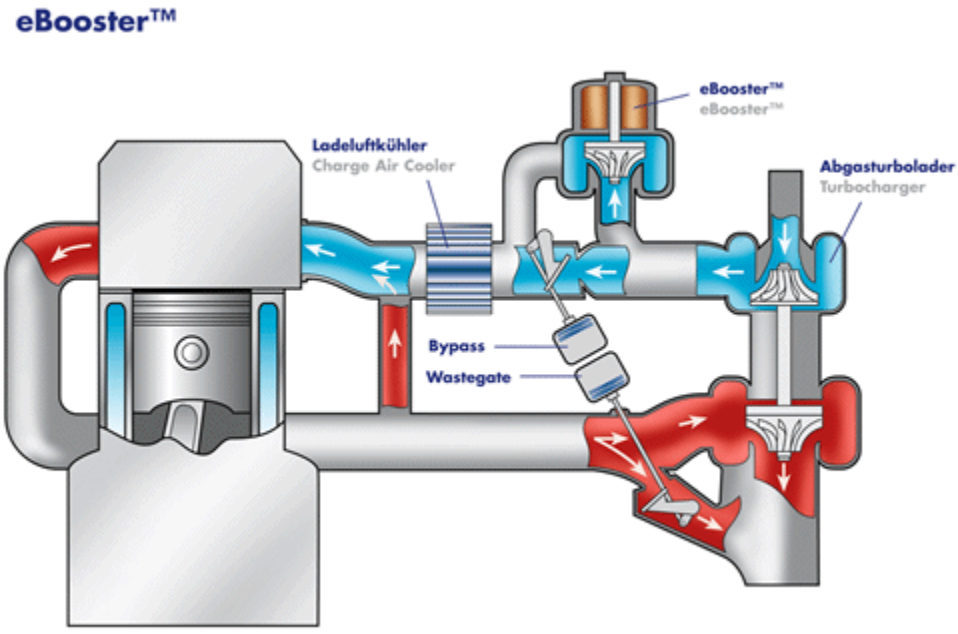

Figure 1.3. Engine air handling system with BorgWarner eBooster [5].

Engines with electrified air handling systems are typically standard IC engines with at least one electrically driven supercharger (eBooster) or turbocharger (eTurbo) providing additional boost pressure to the intake air supply. An eBooster is simply an electric motor connected to a compressor, which allows a controller to directly command compressor speed and by extension intake boost pressure, but unlike a standard supercharger, a valve will typically allow intake air to bypass the eBooster entirely, allowing the eBooster to idle and consume minimal power. An air handling system with an eBooster is shown in Figure 1.3, where the eBooster and bypass valve are placed downstream of the standard turbocharger compressor. An eTurbo is effectively a standard turbocharger with an electric motor attached to the same shaft as the turbine and compressor. This allows the motor to (a) provide additional assistance in spinning the compressor if exhaust flow is insufficient to provide the necessary intake boost pressure, or (b) extract energy from the exhaust flow as electricity if the turbine is driving more intake boost pressure than necessary.

Both of these components increase engine performance by increasing intake air flow more quickly than would be possible with an equivalent turbocharger or supercharger, which in turn allows engine downsizing without sacrificing power output and responsiveness. Additionally, because eBoosters and eTurbos run on much lower voltage electrical systems than a typical traction motor, the battery and power electronics necessary are also relatively small. As a result, electrified air handling offers a convenient drop-in solution for standard IC engines which operate in any kind of standard or hybrid drivetrain, and their performance and efficiency benefits are widely recognized [6]–[17].

1.3.4 Robust $\mathcal{H}_\infty$ Multi-Input Multi-Output Control Design

Electric air handling components will yield performance gains as drop-in components with standalone single-input single output (SISO) control loops, which typically use intake manifold pressure ([9], [16]), intake manifold oxygen fraction ([11]), or air-fuel ratio ([12]) for feedback. For many production engine applications, independent, non-model based, SISO controllers such as PID compensators are good solutions for engine control, because they are straightforward to implement and intuitive to tune [18]. This control approach works

well for engines with few actuators to control or decoupled system dynamics, but as more actuators and tracking parameters are added to an engine, independent SISO loops become more cumbersome. Non-model based controllers often need to be tuned to every specific engine, and each SISO control loop's response effects every other control loop's performance, so re-tuning one loop can require a cascade of re-tuning. Additionally, each actuator will only ever respond based on its particular feedback parameter, so coupling among actuators and parameters can lead to mediocre overall control performance that does not take full advantage of the available actuators. Consequently, the coupled nature of engine gas exchange dynamics calls for a more integrated approach.

A robust $\mathcal{H}_\infty$ multi-input multi-output (MIMO) controller requires more development time, but addresses all of these issues. First, a MIMO controller wraps multiple actuators, feedback parameters, and targets into a single controller, allowing it to coordinate actuators to track target parameters. Second, an $\mathcal{H}_\infty$ controller uses a linear plant model as the foundation for controller design, so for minor engine architecture changes, the controller can be updated simply by updating the engine model, without necessarily re-tuning the entire controller. Third, a robust controller accounts for uncertainty around the nominal plant model, so as long as the physical engine's response lies within the uncertainty region specified, the controller will meet its stated performance targets [19].

An $\mathcal{H}_\infty$ controller is a linear controller, K, obtained from the $\mathcal{H}_\infty$ norm of a controlled linear plant model. Specifically, an optimization problem is set up to find K, (a matrix in general), that minimizes the $\mathcal{H}_\infty$ norm of the closed-loop transfer function from exogenous (uncontrolled) inputs to exogenous outputs [19], [20]. The performance of the resulting controller depends heavily on the accuracy of the linear plant model used in design, and because an IC engine is a nonlinear system, multiple linear models are often necessary to represent an engine's dynamics over its entire operating range. Consequently, the full engine controller often consists of several linear controllers, each of which governs a portion of the engine's operating envelope [21].

1.3.5 Mean Value Engine Modeling for Control

A wide variety of modeling approaches exist for obtaining a control-oriented engine model, but they typically fall into three major categories: crank angle resolved, black box, and mean-value. Crank angle resolved models offer the highest fidelity, and capture high frequency engine dynamics up to 5-15 kHz by modeling in-cylinder dynamics that vary within each cycle, making them ideal for combustion and emissions analysis, but these models are complex and computationally intense, making them unsuitable for gas exchange control [18], [22]. Black box state models are a much faster option and are widely used for control ([23]) because of their simplicity, but they require large amounts of data to generate, and they cannot be generalized to apply to modified engine architectures, because the internal parameters have little if any physical significance.

Mean value models offer a flexible alternative however, because they model physical interactions in the engine, so internal parameters and states represent physical conditions, making them relatively intuitive to tune, validate, and adjust. Because they typically do not model combustion dynamics in detail, mean value models are also simpler and faster than crank angle resolved models, allowing them to capture flow dynamics in the 0.1-50 Hz range, where gas exchange control is achievable. Finally nonlinear mean value state space models are relatively straightforward to linearize, making them ideal for designing gas exchange controllers using the model-based $\mathcal{H}_\infty$ design method.

2. EFFICIENCY ANALYSIS OF SERIES ELECTRIC HYBRID POWERTRAIN

2.1 System Description

The hybrid electric powertrain used in the experimental vehicle for highway testing is a conventional series hybrid system. A 6.7-liter diesel engine runs at constant speed during vehicle operation, driving a three-phase synchronous AC generator, to act as a genset system. The three-phase 200 HP induction motor provides all tractive power, and two 85-kWh Tesla battery packs connected in series provide energy storage. This configuration is shown in

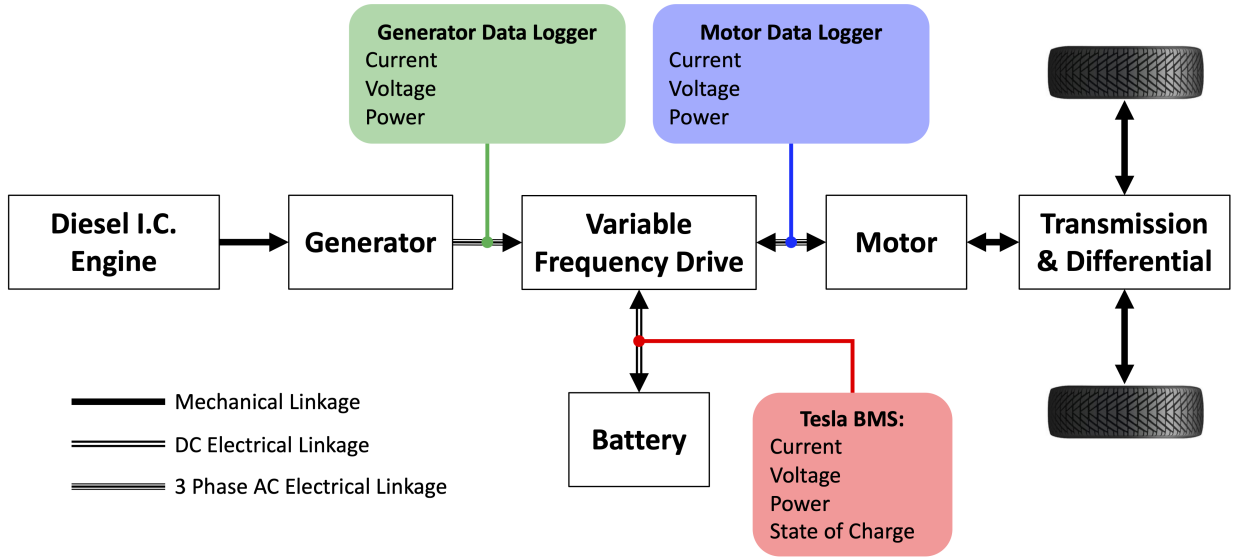

Figure 2.1. Series hybrid system diagram

Figure 2.1, along with the positioning of three data loggers to capture power flows within the elctrical components of the drivetrain. The motor and generator data loggers are identical, recording current, voltage, and power for each electric machine's three phases, and the Tesla battery management system (BMS) tracks the battery's current, voltage, power, and state of charge. A GPS logger also tracks the truck's position in three dimensions and calculates its velocity and elevation.

A simplified system diagram, shown in Figure 2.2, highlights the important electrical energy paths and establishes the power flow convention as positive when the battery is

discharging and the motor is driving the wheels. In this system, the generator cannot back-drive the engine, so its power is always positive. For simplicity of analysis and due to the positioning of data loggers in the system, the power electronics block encompasses both the variable frequency drive and power controller, which commands the magnitude and direction of power to and from the motor and battery.

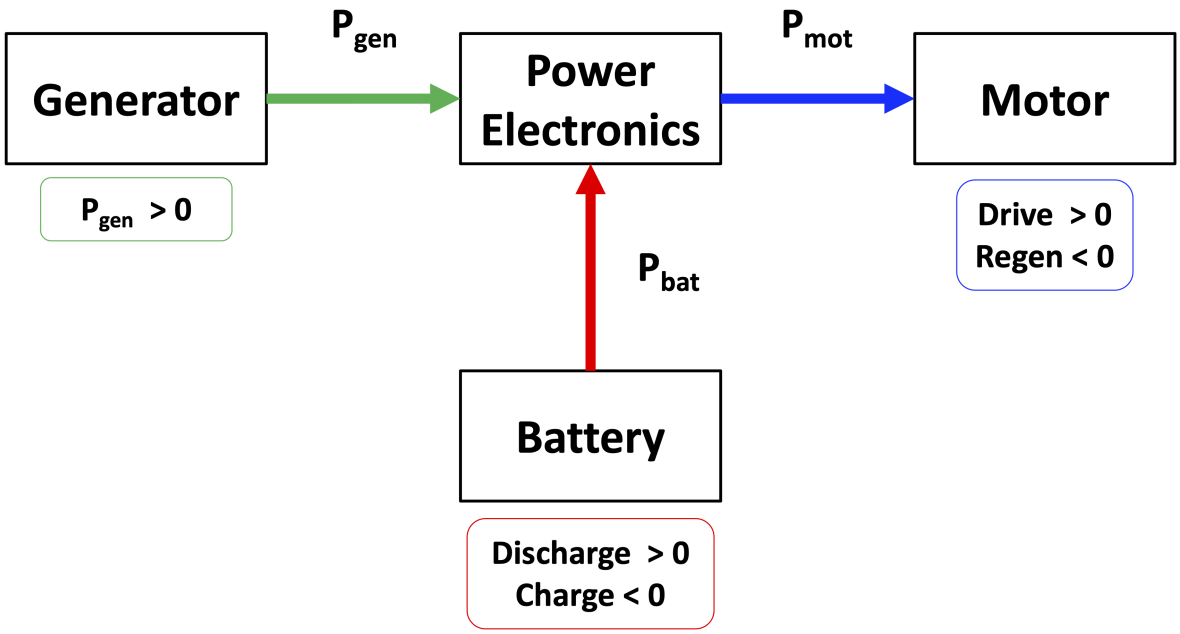

Figure 2.2. Simplified system block diagram and selected reference directions

2.2 Data Collection

In this phase of testing, the startup collected data from 21 test runs along two test routes between October 2019 and January 2020. Gross vehicle weight (GVW was varied throughout the tests, but the same trailer was used in all test cases, and each payload weight was used for several test runs. Several tests exhibited anomalies in the data collected, so not all data was used for every analysis step, but all test runs are summarized in Table 2.1, along with the relevant data anomalies.

Table 2.1. List of test data sets

Run #	Date	Route	GVW [lb]	Data Anomalies
1	27 September 2019	Lexington	52,720	
2	10 October 2019	Lexington	52,720	
3	14 October 2019	Lexington	52,720	
4	15 October 2019	Lexington	55,800	
5	16 October 2019	Lexington	55,800	BMS timestamp jumps
6	17 October 2019	Lexington	55,800	BMS timestamp jumps
7	18 October 2019	Lexington	55,800	BMS timestamp jumps
8	19 October 2019	Lexington	55,800	BMS timestamp jumps
9	20 October 2019	Lexington	55,800	BMS timestamp jumps
10	22 October 2019	Lexington	55,800	
11	23 October 2019	Lexington	55,800	
12	24 October 2019	Lexington	60,120	
13	28 October 2019	Lexington	60,120	BMS timestamp jumps
14	29 October 2019	Lexington	60,120	BMS timestamps rounded to nearest minute
15	1 November 2019	Lexington	60,120	BMS timestamp jumps
16	2 November 2019	Lexington	60,120	BMS timestamp jumps
17	4 November 2019	Lexington	60,120	GPS data missing after 2.5 hours
18	9 January 2020	Indianapolis	58,200	
19	13 January 2020	Indianapolis	55,800	
20	14 January 2020	Indianapolis	55,800	BMS timestamp jumps & missing generator data after 1 hour
21	20 January 2020	Indianapolis	55,800	BMS timestamp jumps & generator data doesn't appear to match

2.2.1 Test Routes

The first 17 test runs were conducted along a roughly 100 km stretch of I-75 in Kentucky between Florence and Lexington, shown in Figure 2.3. This route is optimal for vehicle testing, because it avoids congestion in Cincinnati and Lexington, and gentle grade changes provide significant energy recapture opportunities without stressing the powertrain on long uphill or downhill stretches. Road grade varies regularly within 2° (3.5%) of level throughout the test section, shown in Figure 2.4.

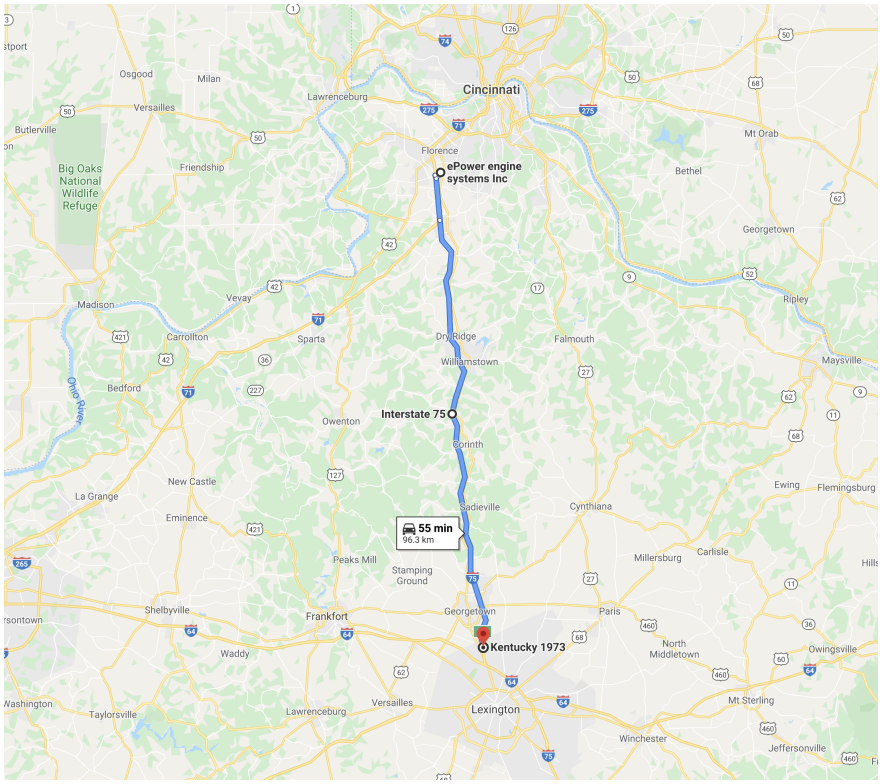

Figure 2.3. Lexington test route map

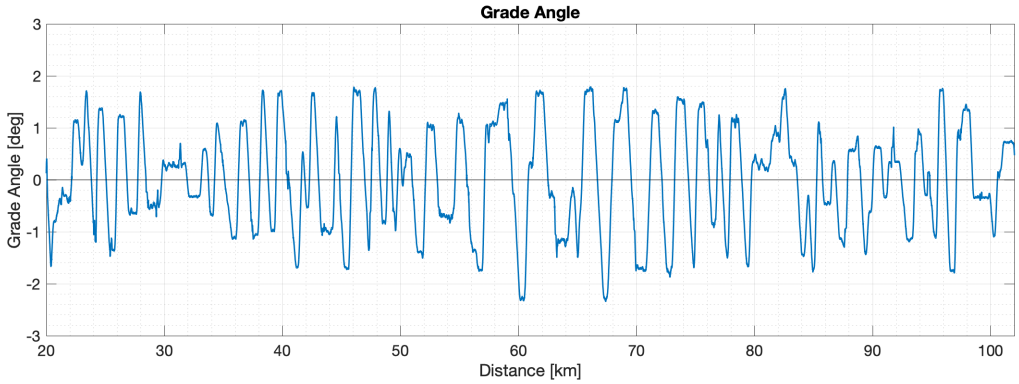

Figure 2.4. Lexington test route grade angle (degrees)

The remaining four tests were conducted along a 140 km section of highway between two rest stops on I-74 and I-70 in Indiana. Traffic along this route, shown in Figure 2.5, is busy at the interchange with the I-465, but otherwise generally light. However, unlike the Kentucky route, this stretch of highway is significantly flatter, as shown in Figure 2.6. Consequently, there are fewer downhill sections of roadway to provide energy recapture opportunities, which does not favor the hybrid drivetrain's architecture.

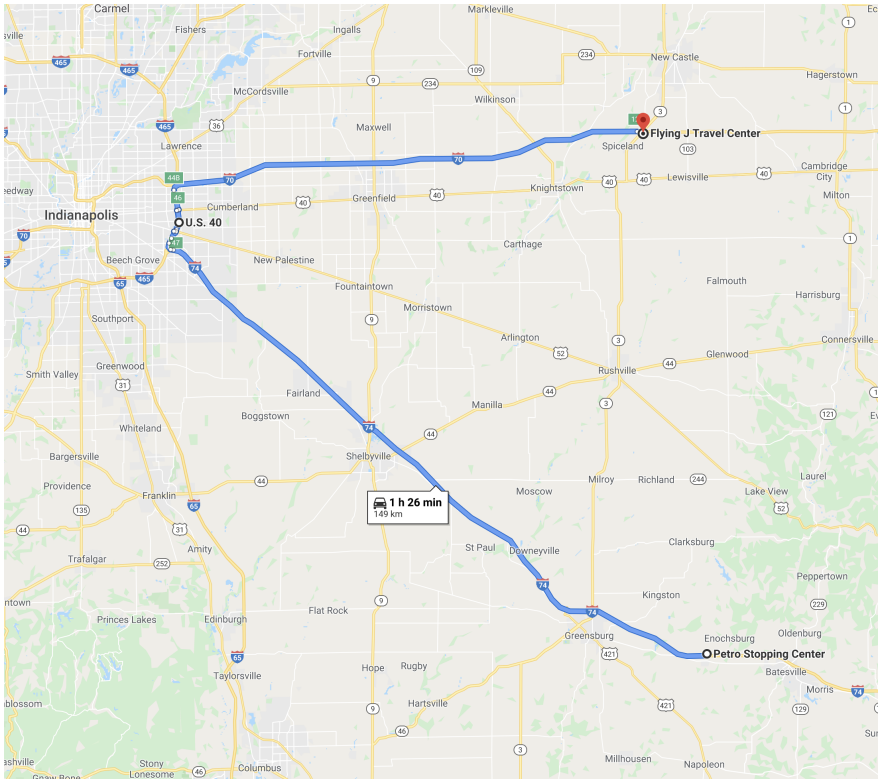

Figure 2.5. Indianapolis test route grade angle (degrees)

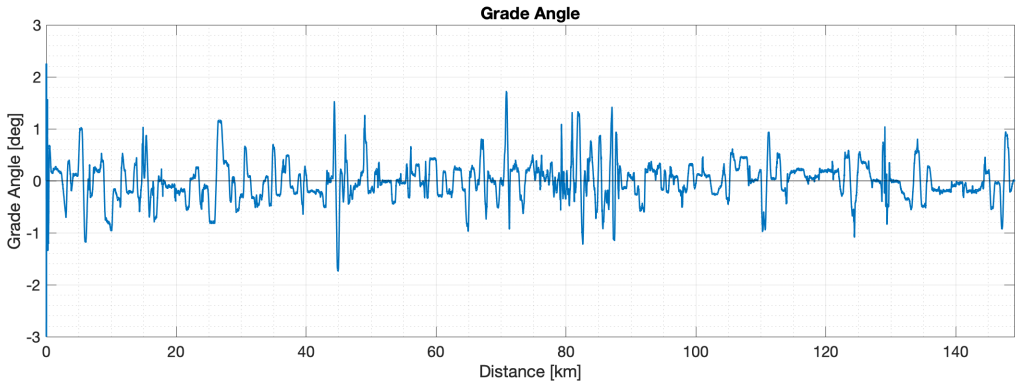

Figure 2.6. Indianapolis test route grade angle (degrees)

2.2.2 Data Filtering

The raw data obtained during testing was is clean, especially from the motor and battery data loggers, but GPS data captures more noise due to a higher sample rate. Additionally, the discrete time derivative is taken of the GPS's elevation and velocity data to obtain grade angle and truck acceleration, and this amplifies any noise in the original data. To combat this problem, a moving average filter capturing 20 samples, or 2 seconds of data on either side of each sample point, is applied to the elevation and velocity data streams, providing the best compromise between smoothness and resolution for the filtered data.

Grade angle along the truck's route is calculated as a function of the raw velocity and elevation data from the GPS, as shown in Equations 2.1 - 2.4, where h is the truck's elevation, v is its velocity, x is the distance travelled, and θ is the grade angle. These data streams are sufficiently clean without filtering, so a filter is only applied to the derivative of elevation with respect to distance, dh/dx.

$$\left(\frac{\Delta h}{\Delta t}\right)_k = \frac{h_{k+1} - h_k}{t_{k+1} - t_k} \tag{2.1}$$

$$\left(\frac{\Delta h}{\Delta x}\right)_k = v_k \left(\frac{\Delta h}{\Delta t}\right)_k \tag{2.2}$$

$$\overline{\left(\frac{\Delta h}{\Delta x}\right)}_k = \text{average}\left[\left(\frac{\Delta h}{\Delta x}\right)_{k-20}, \left(\frac{\Delta h}{\Delta x}\right)_{k-19}, \ldots, \left(\frac{\Delta h}{\Delta x}\right)_{k+20}\right] \tag{2.3}$$

$$\text{Grade Angle} = \theta = \arctan\overline{\left(\frac{\Delta h}{\Delta x}\right)}_k \tag{2.4}$$

The grade angle profiles and Fast Fourier Transform (FFT) magnitude plots are shown in Figures 2.7 and 2.8 before and after filtering. As expected, the grade angle data is significantly cleaner, with no appreciable loss in resolution.

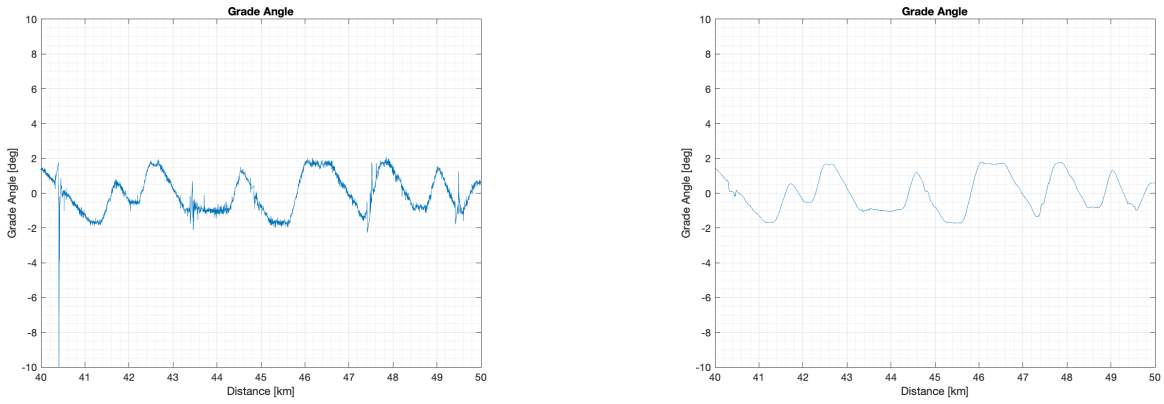

(a) Raw (b) Filtered

Figure 2.7. Grade angle for 10-km stretch of Lexington route on 10 October with and without filtering.

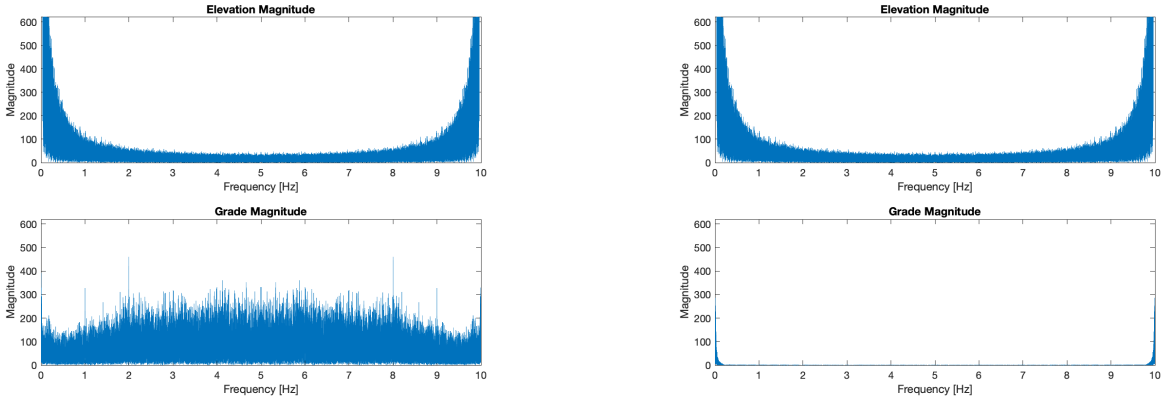

(a) Raw (b) Filtered

Figure 2.8. FFT plots for elevation and grade angle data with and without filtering.

The truck's acceleration profile can also be calculated from GPS velocity data as shown in Equations 2.5 and 2.6.

$$a_k = \frac{v_{k+1} - v_k}{t_{k+1} - t_k} \tag{2.5}$$

$$\overline{a}_k = \text{average}\left[a_{k-20}, a_{k-19}, \ldots, a_{k+20}\right] \tag{2.6}$$

The acceleration profiles and Fast Fourier Transform (FFT) magnitude plots are shown in Figures 2.9 and 2.10 before and after filtering. Because the acceleration data is much noisier than the grade angle data to begin with, the final filtered acceleration profile is not as smooth, but more aggressive filtering obscures the vehicle's dynamics.

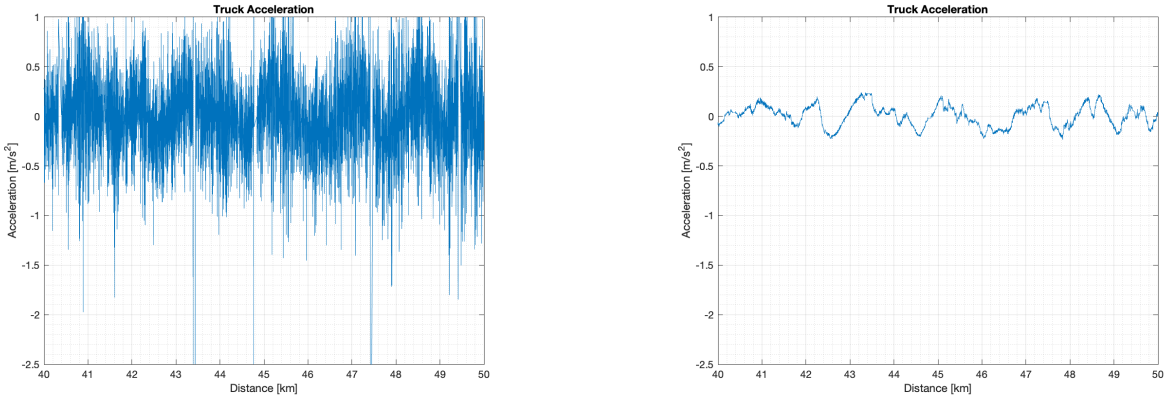

(a) Raw (b) Filtered

Figure 2.9. Acceleration profile for 10-km stretch of Lexington route on 10 October with and without filtering.

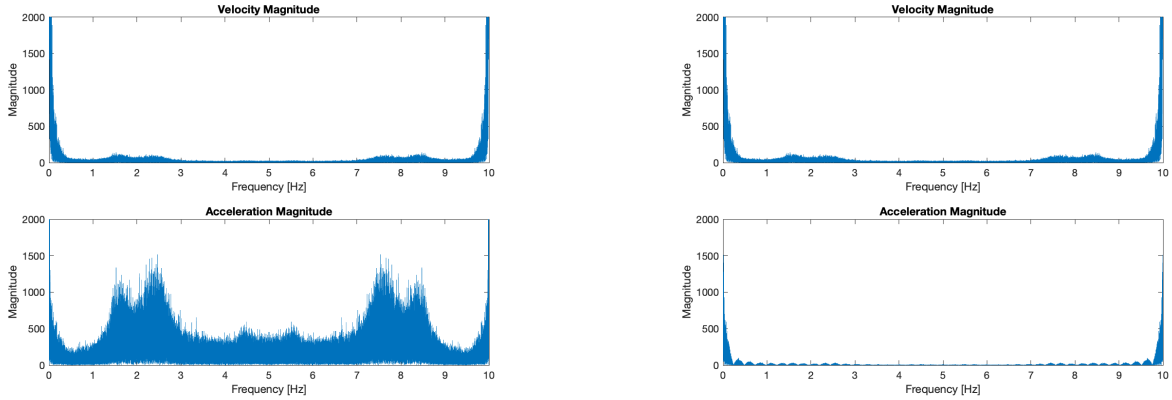

(a) Raw (b) Filtered

Figure 2.10. FFT plots for velocity and acceleration data with and without filtering.

2.2.3 Distance Traveled Calculation

To facilitate direct comparisons between test runs and routes, it is useful to plot parameters against the distance the truck has traveled from an arbitrary starting point. However, all data is recorded against a time array, so a master array of distances traveled is generated from the GPS data as shown by Equation 2.7.

$$x_k = \sum_{\mathrm{i}=0}^{k} v_\mathrm{i} \Delta t_\mathrm{i} \tag{2.7}$$

Multiplying velocity, v_i, by the sample duration, Δt_i, for the i^{th} sample yields the distance traveled during this sample. The sum of these products from sample $\mathrm{i} = 0$ to sample $\mathrm{i} = k$ is the distance from the arbitrary start to time t_k. This new array of distances can then be used as an independent plotting variable instead of time for any of the measured parameters.

2.3 Component Energy Inputs and Outputs

To provide a broad understanding of each powertrain component's contribution to vehicle propulsion and the associated mechanisms for fuel savings, the power flows for each component are analyzed independently. During normal highway operations, the power electronics direct most of the engine-driven generator's energy to the traction motor. The regenerative

braking energy captured by the traction motor is sufficient to keep the battery charged, so the generator does not provide power to the battery, other than during low speed stop-and-go operations. Sample sets of power flow, road grade, and velocity data are shown for 4-km sections of the Lexington route in Figure 2.11 and the Indianapolis route in Figure 2.12.

Each component's net energy contribution is then determined from the power flow data by integration according to Equation 2.8, where $P(\tau)$ is the measured power flow, $d\tau$ is the time step between samples, which was typically 1 second, and $E(t)$ is the cumulative energy delivery from the beginning of the run to time t.

$$E(t) = \int_0^t P(\tau) d\tau \tag{2.8}$$

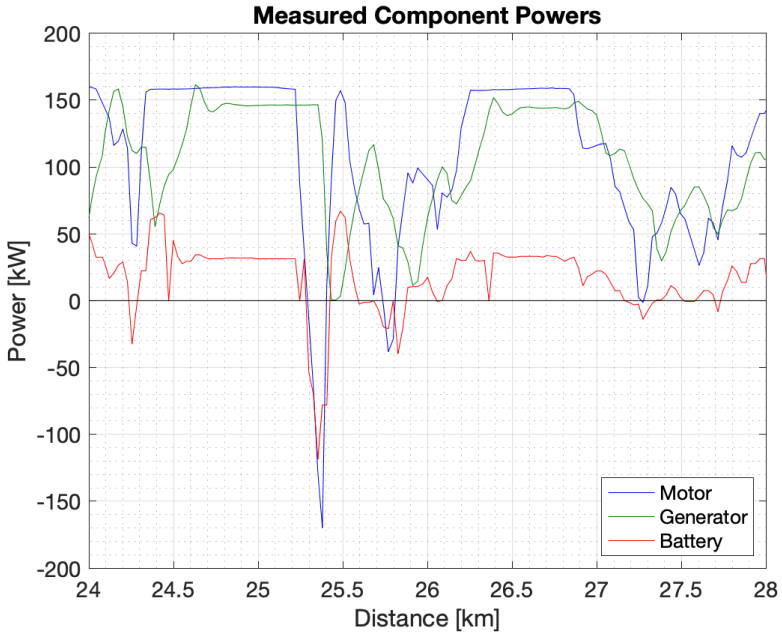

(a) Motor, generator, and battery power

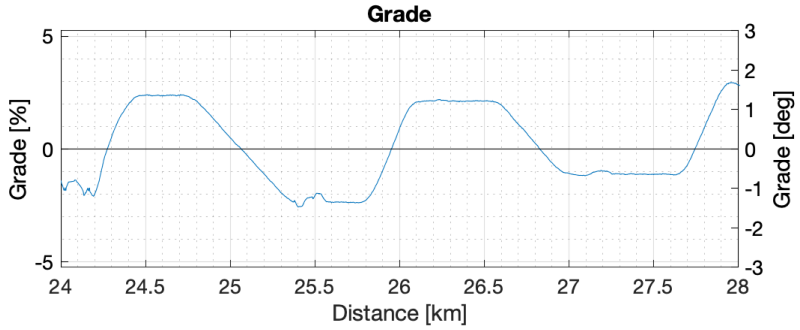

(b) Grade

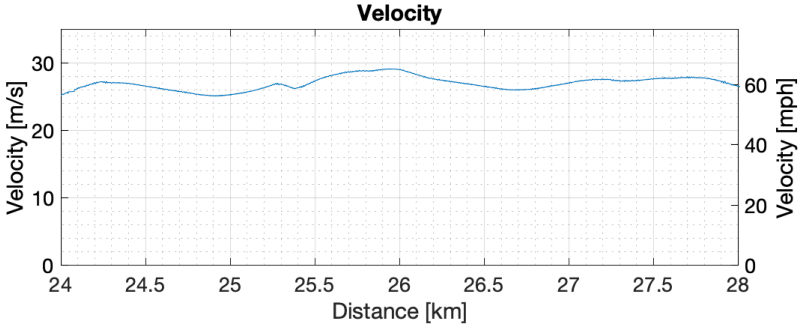

(c) Velocity

Figure 2.11. Power flows and drive cycle conditions for 4 km of Lexington route on 10 October

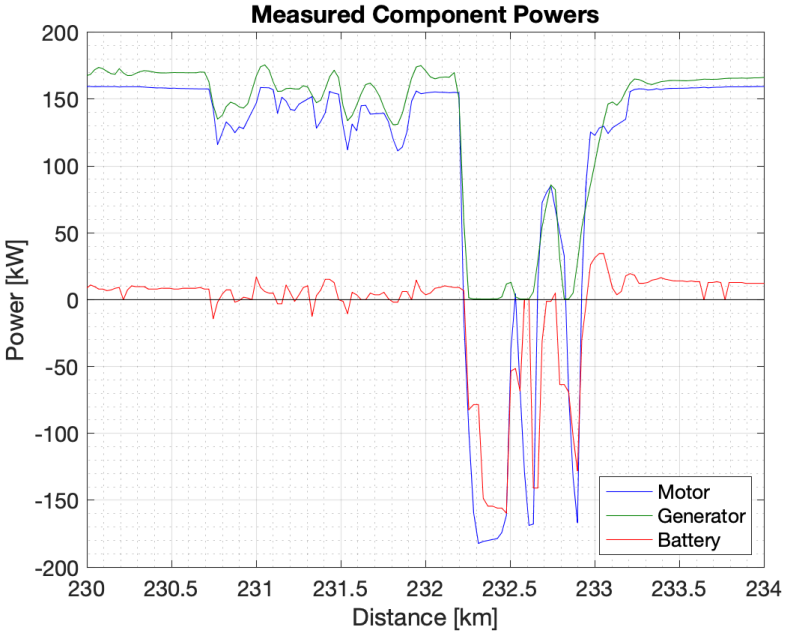

(a) Motor, generator, and battery power

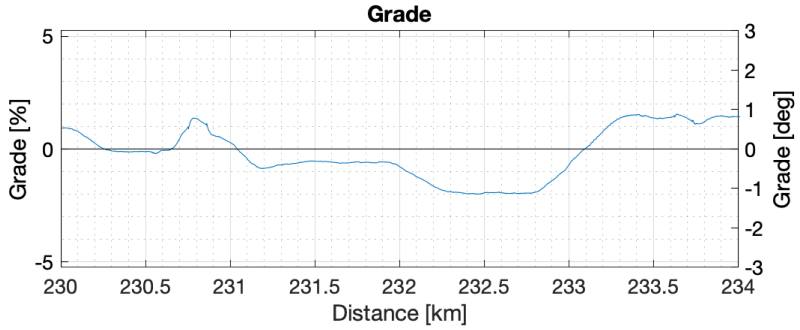

(b) Grade

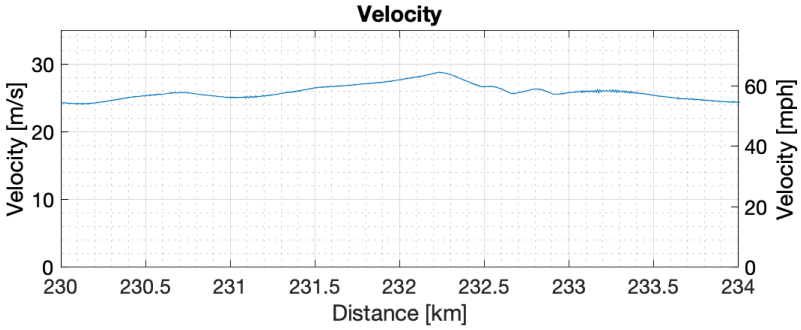

(c) Velocity

Figure 2.12. Power flows and drive cycle conditions for 4 km of Lexington route on 9 January

2.3.1 Engine and Generator

The generator satisfies most of the vehicle's propulsive power requirement, and as a result, the engine, generator, and motor power are closely tied. The diesel engine's fueling controller maintains shaft speed within 100 rpm of the 1800 rpm setpoint to maximize efficiency, while the generator varies the load torque on the engine. No direct mechanical power measurement was taken from the engine, but the speed and load data from the engine control module (ECM) are shown in Figure 2.14. The generator power output, shown in Figure 2.13, varies between 0 and 160 kW, closely matching the traction motor's power demand range when driving. The battery accounts for any discrepancy, as the battery also contributes to the tractive power requirement during discharge.

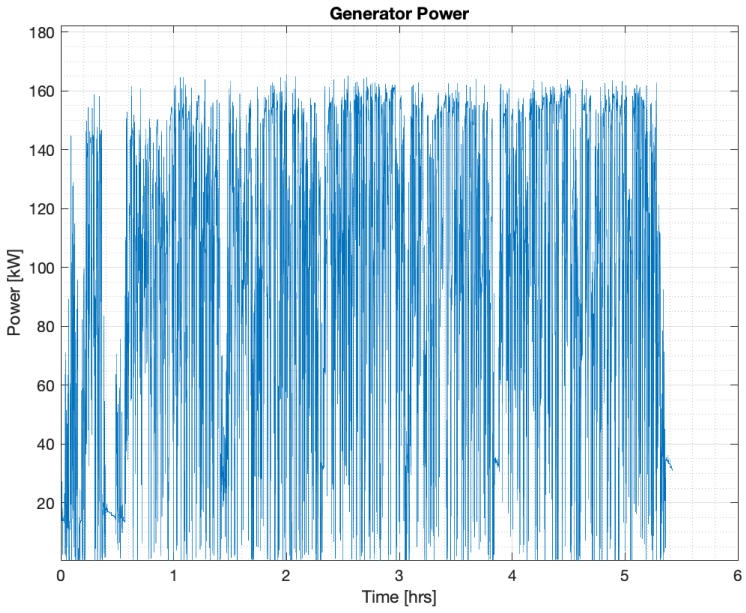

Figure 2.13. Generator power output from Lexington test on 10 October

The energy curves for the generator are shown in Figure 2.15 for the four primary weight and route configurations, and within each weight, total generator energy supply was reasonably consistent within each test category. Tests conducted at heavier vehicle weights tend to require more energy from the generator, but other environmental differences among tests such as wind cause similar magnitude variations. For example, the October 14$^{\text{th}}$ Lexington

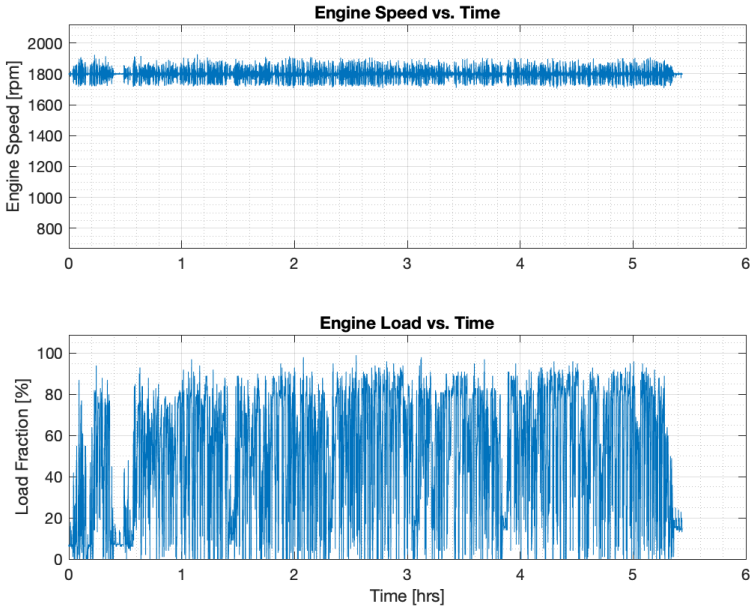

Figure 2.14. Diesel engine rpm and load

test at 52,720 lbs, shown in yellow in Figure 2.15a, was conducted in gusty 15 mph cross-winds, causing a much greater energy demand from the generator compared to the September 27^{th} and October 10^{th} tests.

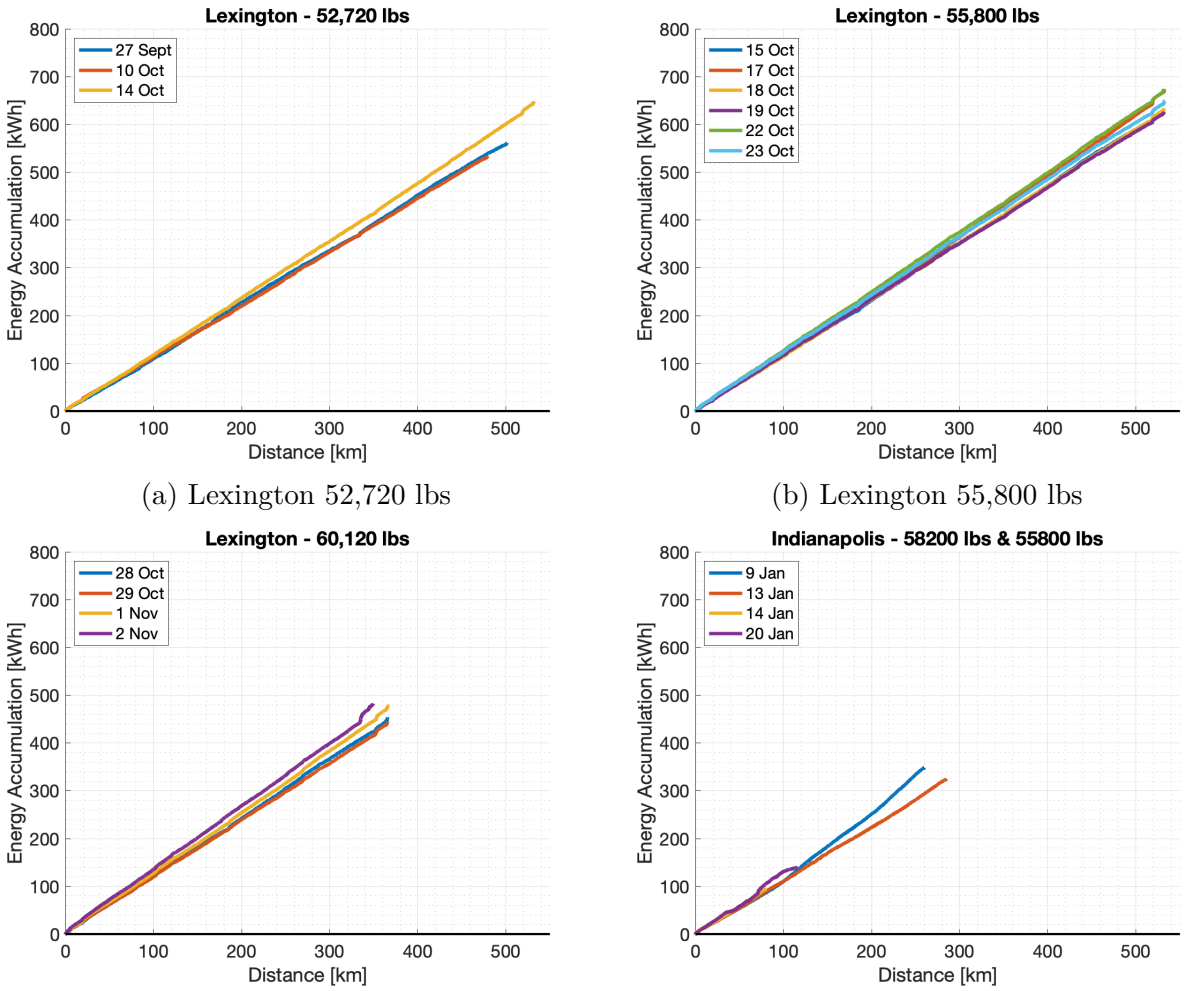

(a) Lexington 52,720 lbs

(b) Lexington 55,800 lbs

(c) Lexington 60,120 lbs

(d) Indianapolis 58,200 & 55800 lbs

Figure 2.15. Generator energy accumulation functions

2.3.2 Traction Motor

In the test vehicle's series hybrid configuration, the motor is the only drivetrain component mechanically connected to the wheels, so it supplies all of the truck's mechanical power. Like the generator, the motor operates up to a maximum positive electrical power of 160 kW, shown in Figure 2.16, but it spends more time at this upper power limit, indicating that the battery makes up the deficit. Additionally, due to losses mainly in the power electronics, the motor power, P_{mot}, consistently exceeds the sum of the battery and generator powers, $P_{\text{bat}} + P_{\text{gen}}$, by 5% - 15% during steady operation, as plotted in Figure 2.17 for a 5-km stretch of the Lexington test route. The traction motor can also act as a generator to

capture braking energy, shown as a negative power measurement in Figures 2.16 and 2.17. These regenerative braking events can cause spikes up to 200 kW and match the battery charge spikes in Figure 2.17.

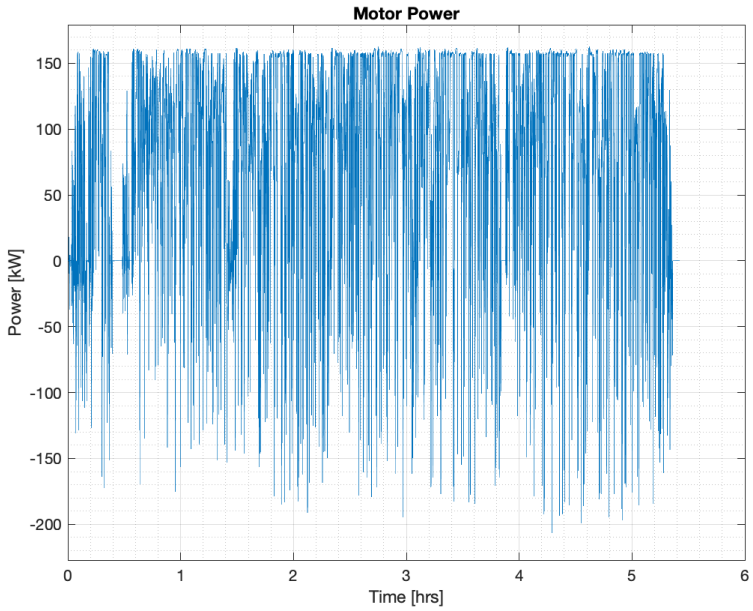

Figure 2.16. Motor power from Lexington from 10 October test run

The drive and regeneration energy accumulation functions for the motor are consistent throughout testing and are plotted as solid, positive and negative, dotted lines in Figure 2.18.

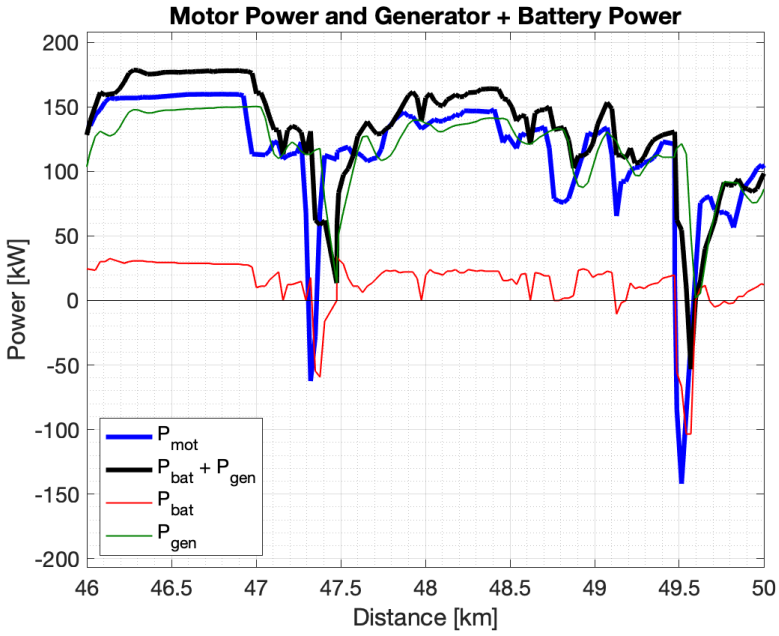

Figure 2.17. $P_{\text{bat}} + P_{\text{gen}}$ from Lexington from 10 October test run

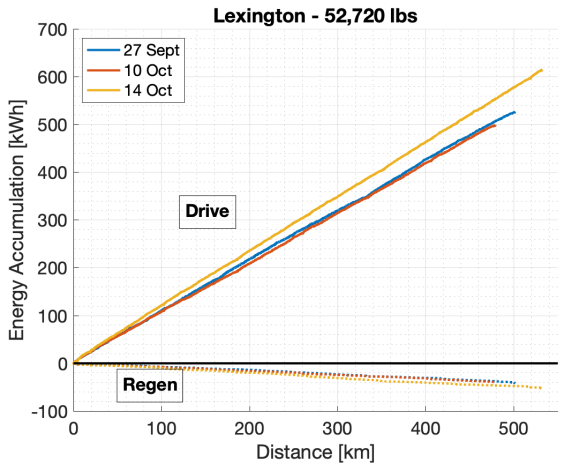

(a) Lexington 52,720 lbs

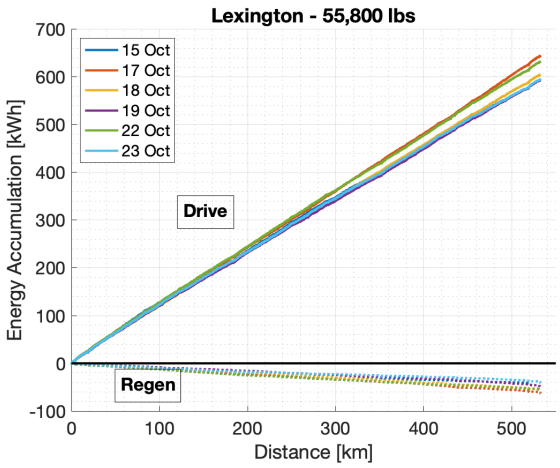

(b) Lexington 55,800 lbs

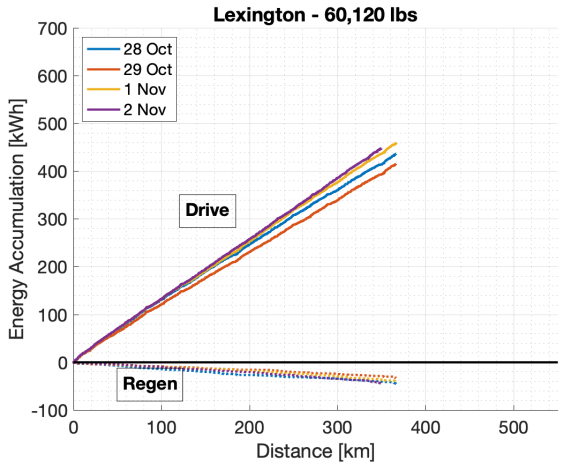

(c) Lexington 60,120 lbs

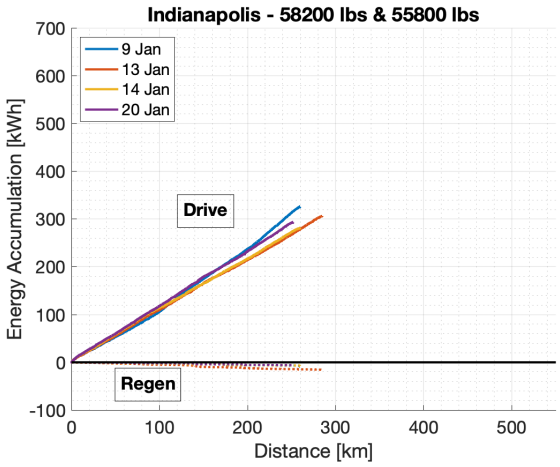

(d) Indianapolis 58,200 & 55800 lbs

Figure 2.18. Motor energy accumulation functions

2.3.3 Battery

In the test vehicle powertrain, the traction motor delivers large power spikes back to the power electronics during regenerative braking events, and the generator and diesel engine absorb most of the transient traction power fluctuations over a drive cycle. Consequently, as shown in Figure 2.19, the battery's state of charge does not vary significantly over time, but it must accept and deliver large current spikes.

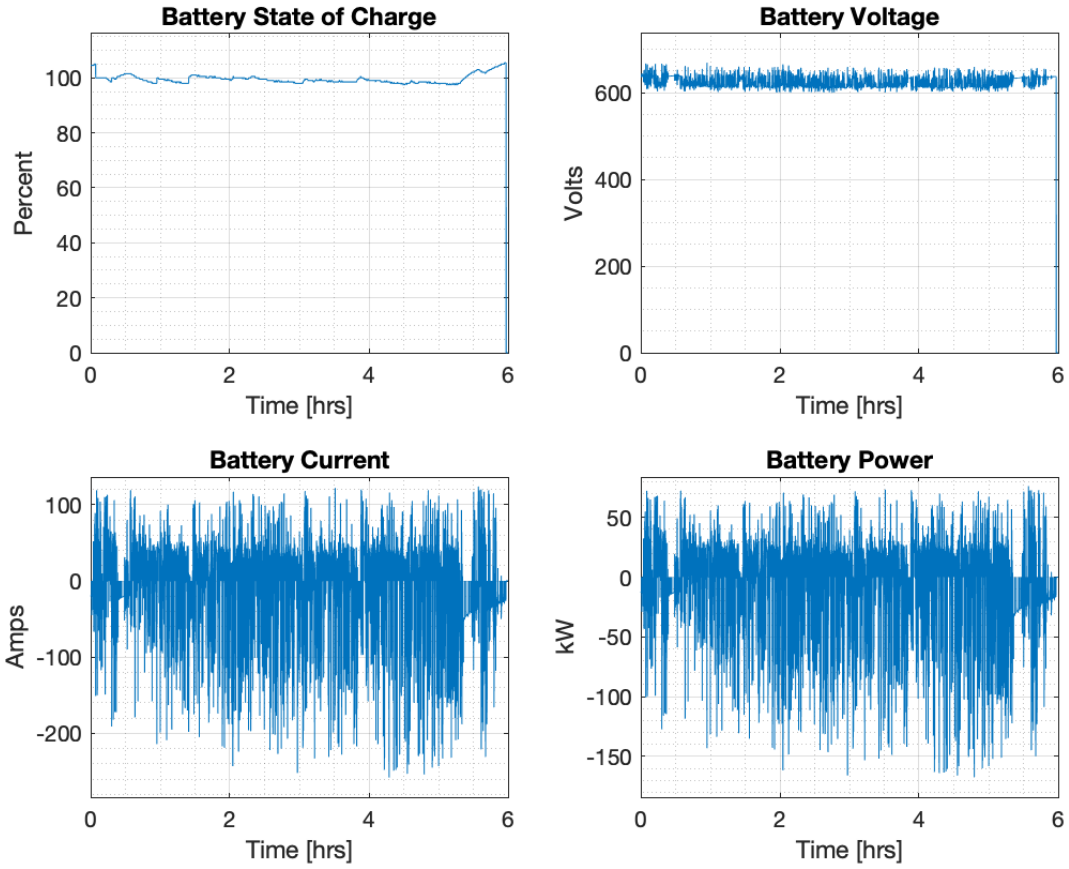

Figure 2.19. Battery power, current, voltage, and state of charge from 10 October test run

Because the batteries used in the test vehicle were purchased second-hand to reduce cost, and they were used aggressively during truck testing, significant signs of wear are apparent from these data. First, a battery management system (BMS) will typically reset the state of charge (SOC) to 100% when allowable cell voltages are suddenly exceeded, as would occur

during aggressive use. During some periods of high current charging or discharge in testing, the BMS recorded physically impossible jumps up to 100% SOC, which is consistent with one of these reset events. Second, the BMS reported an overall battery SOC consistently near 100%, even though randomly sampled cells were closer to the nominal 3.8 V expected from a cell at 50% SOC. Third, the measured terminal voltage was approximately 110 V below the nominal 750 V expected from two Tesla battery packs connected in series, indicating that some modules in the battery are not contributing to the overall battery voltage.

However, the battery still stores sufficient regenerative braking energy to provide drive energy and reduce the energy demand on the generator. The battery's charge (negative), discharge (positive), and net energy accumulation functions are shown in Figure 2.20 as dotted, bold, and thin lines respectively. The battery consistently shows a small net discharge (positive) over most of the test runs, which is consistent with the BMS reported SOC if the non-physical jumps to 100% are removed. However, gross charge and discharge energy depends heavily on payload and route. With 15% weight increase of 7,500 lbs, the truck captures 50% more energy from regenerative braking over the Lexington route, although the power management algorithm was also adjusted to rely more heavily on the battery for these runs, accounting for some of these gains (Figures 2.20a & 2.20c). In contrast, the shallower grade of the Indianapolis route provides only half the energy that the battery stores and returns on the first 250 km of the Lexington route.

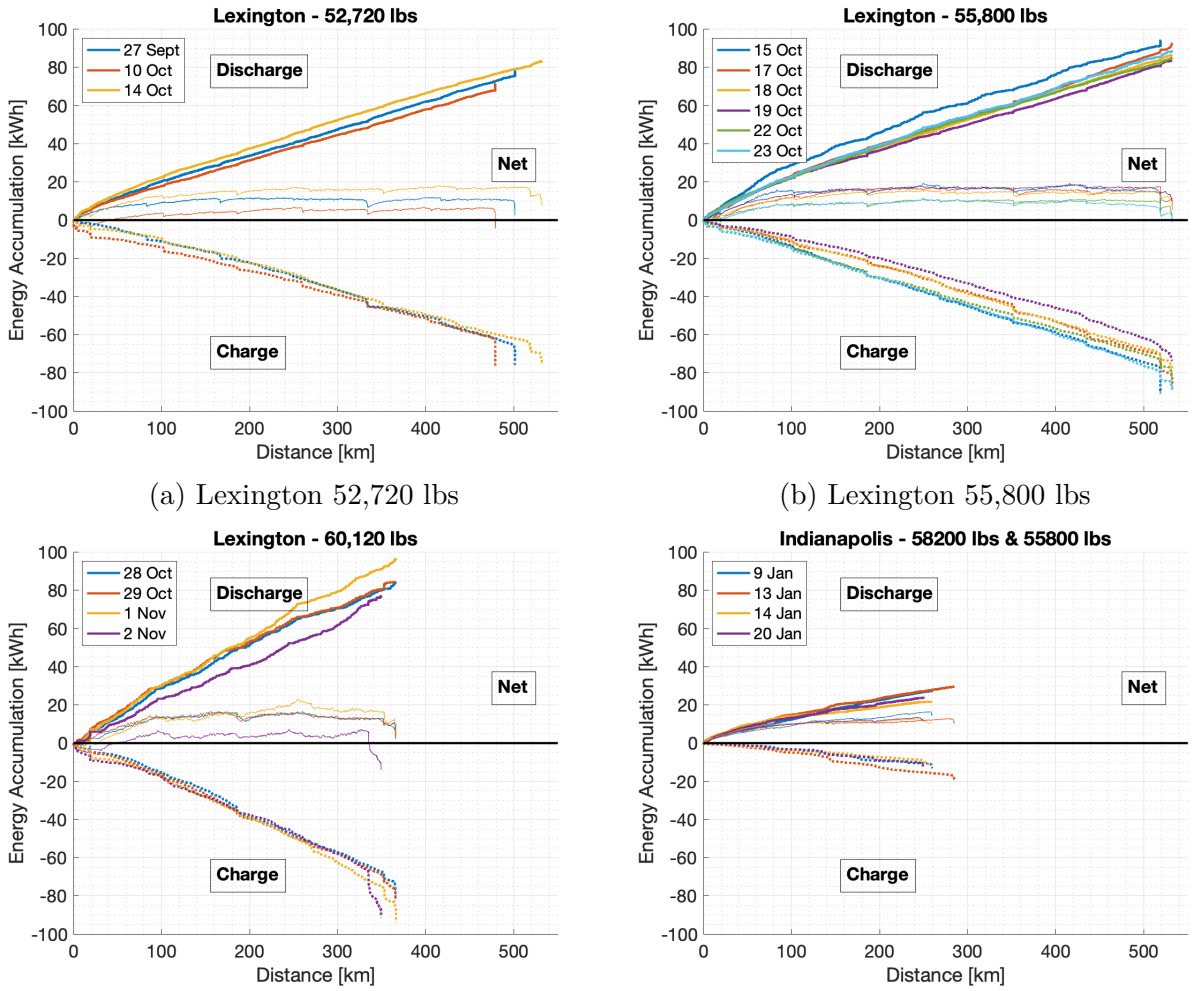

(a) Lexington 52,720 lbs

(b) Lexington 55,800 lbs

(c) Lexington 60,120 lbs

(d) Indianapolis 58,200 & 55,800 lbs

Figure 2.20. Battery energy accumulation functions

2.3.4 Contribution of Each Component to Vehicle Work Performed

The energy accumulation curves for the test vehicle's generator, battery, and traction motor highlight each component's contribution to the tractive energy requirement of a full drive cycle. The October 10th Lexington route test at 52,720 lbs represents the trends observed throughout the data sets, and these energy accumulation curves are plotted in Figure 2.21. Two notable observations from these results regarding battery operation and system losses are discussed below.

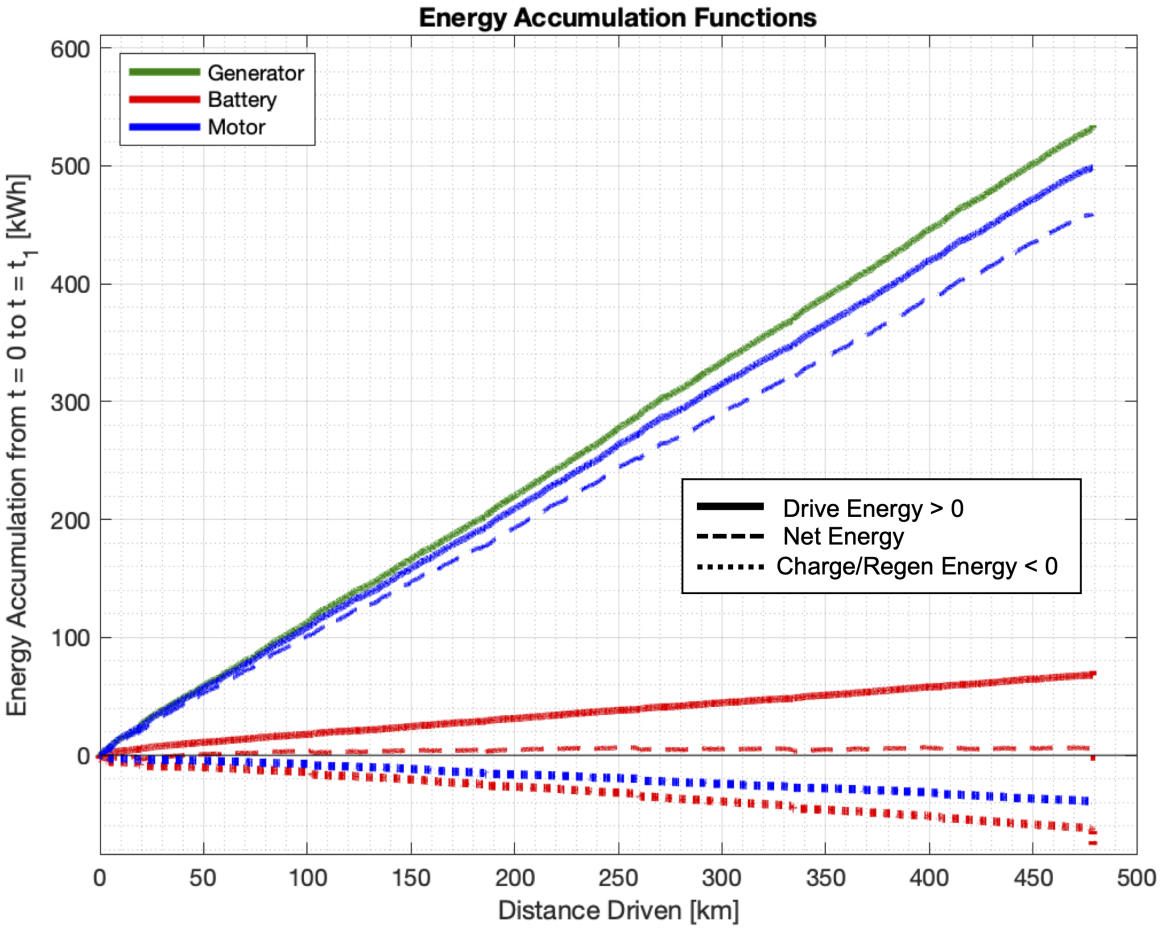

Figure 2.21. Component energy accumulation curves for 10 October test run

Battery Operation

During normal highway operation, the traction motor supplies most of the battery charge energy through regenerative braking, but as shown in Figure 2.21, the battery charge energy ($E_{\text{bat,charge}} < 0$, red dotted curve) exceeds the motor regeneration energy ($E_{\text{mot,regen}} < 0$, blue dotted curve). The generator must make up this difference, and although it does provide some energy to the battery during highway operation, most of the the energy transfer from the generator to the battery occurrs at low speed. Every 80 km, the driver slows to turn the truck around, and during this maneuver, the truck operated at low or zero speed for around one minute. For this brief period, the motor stops producing regeneration energy, and the

generator supplies energy to the battery and the motor, causing the total battery charge energy to exceed the motor regeneration energy.

This behaviour would not matter in a perfect system with no electrical losses, but in the real powertrain, losses occur in both the battery and the power electronics. As a result, when the generator charges the battery, power must flow through the power electronics on its way into and out of the battery, (see Figure 2.2) incurring losses in each component. It is much more efficient for the generator to supply energy straight to the drive motor, and since the battery's total capacity of 170 kWh is more than double its discharge energy over a single test run, the generator arguably does not need to charge the battery, assuming it can be charged outside the vehicle's normal drive cycle.

The battery itself is also oversized for the application in order to keep the C-rate near a reasonable range during aggressive charge and discharge spikes. Even though the battery's SOC does not vary significantly, and a fully charged battery would supply more than enough energy for the entire test without recharging, the Tesla battery pack requires relatively low charging rates as a fraction of total capacity. A chemistry optimized for power delivery instead of total capacity would allow a significantly smaller battery to replace the relatively sensitive Tesla battery, and a battery without the wear signs exhibited in testing would reduce electrical losses during both charge and discharge modes.

System Losses

In an ideal powertrain with no electrical losses, the generator would deliver precisely the motor's net energy requirement, and the battery would return all regenerative braking energy to the traction motor, satisfying the remaining propulsive energy requirement. This would place the green line in Figure 2.21 on top of the blue dashed line. However, in testing, the generator delivers 15% more energy than the net propulsive energy requirement and actually exceeds the total propulsive energy requirement due to losses primarily in the battery and power electronics. The power electronics losses, discussed in detail in Section 2.4, are expected and unavoidable, but a newer battery designed to handle the high charge and discharge currents observed could substantially improve this efficiency.

Summary of Component Energy Contributions

The total energy contributions of each component, equal to the final values on the energy accumulation curves, are divided by total distance traveled for each test to allow direct comparison among tests of different lengths. The BMS recorded time stamps incorrectly for significant portions of tests 5, 9, 12, and 17 (Oct. 16, Oct. 20, Oct. 24, and Nov. 4), so these runs are omitted from these results.

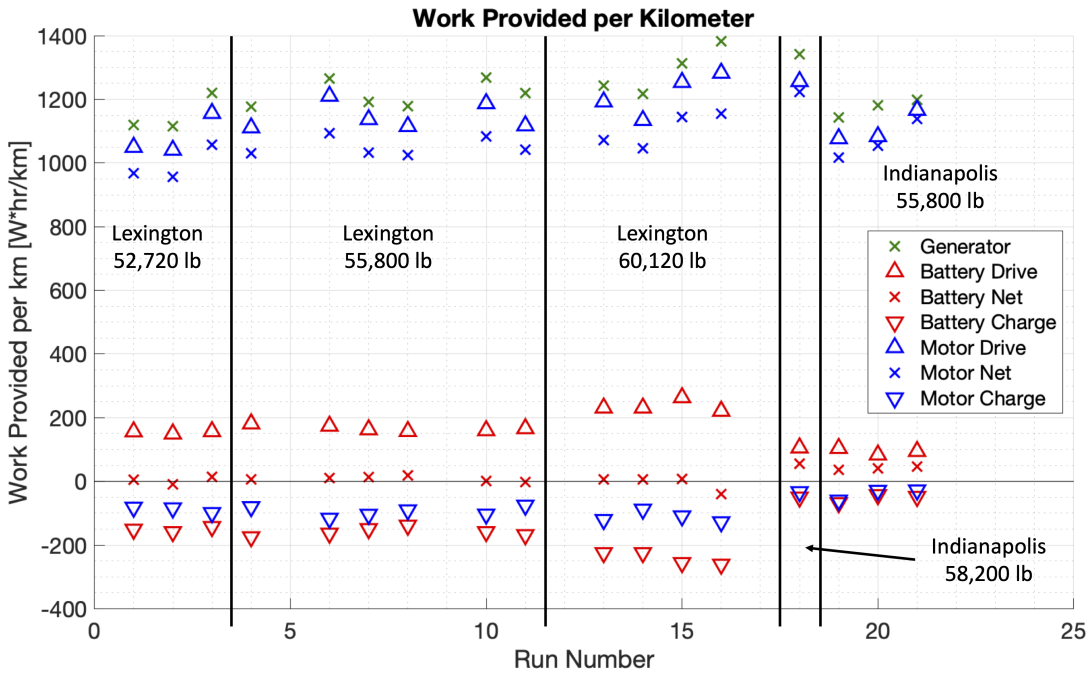

Figure 2.22. Work contributed by each component per km for all data sets

Increases in payload mass generally require increased power flow to and from the motor and battery, although component energy contributions vary with similar magnitude from run to run, indicating that environmental factors such as weather and traffic significantly effect propulsive energy requirements as well. Additionally, in all test runs, the battery delivers near zero net energy, and the battery charge energy is greater than the motor regeneration energy, affirming the conclusion that some of the generator output contributes to charging the battery. Finally, the relatively flat grade along the Indianapolis route as compared to the

Lexington route requires much less energy flow through all system components, especially the battery.

2.4 Power Electronics Efficiency Analysis

In series hybrid electric powertrains, electrical losses arise in all four of the major components shown in Figure 2.1. No mechanical power measurements were taken in the experimental drivetrain, which precludes calculation of the generator and motor efficiencies, but these components have well documented efficiencies around 90% - 95% that cannot be easily improved, so they are not considered in this analysis. Also, the battery is known to have losses due to wear, and since the startup plans to replace the battery in future prototypes, its efficiency is not calculated.

However, the energy flows into and out of the power electronics were measured, allowing separate efficiency calculations for each energy flow path. Regardless of the path of flow, the power electronics efficiency is the ratio of total input energy to total output energy over a given sample time, with the assumption that energy cannot be stored in the power electronics. Figure 2.23 illustrates the system boundary in the simplified system, and Figure 2.24 represents where the data loggers measure power flows in the power electronics circuitry. These measurement points are assumed to be the only points of energy flow across the system boundary defined in Figure 2.23. The energy sums can be calculated from the power data recorded at these points according to the energy accumulation integral, shown in Equation 2.8.

2.4.1 Power Modes

Power can flow through the power electronics in three fundamental ways. Although the generator only provides energy input to the power electronics, both the battery and the motor can either provide energy input to or accept energy output from the power electronics, so the signs of the power flows to and from the motor and battery reveal which mode of operation the vehicle is in at any given moment. Figure 2.25 describes the three modes that result from these different energy flow directions. Battery power never remains near zero for

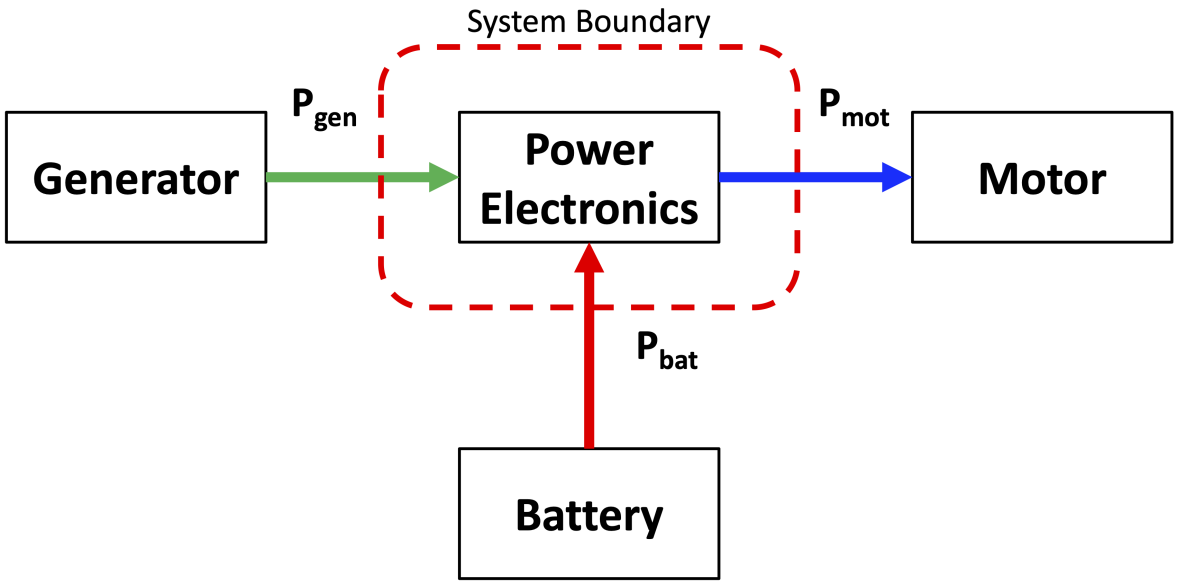

Figure 2.23. Power electronics system definition and energy inputs/outputs

more than a few seconds at a time, and motor power only remains near zero when the truck is stopped, so these cases are not considered in the efficiency analysis. In Mode 1 (drive mode), both the generator and the battery are providing drive power to the motor, so the input and output energies can be calculated according to Equations 2.9 and 2.10.

$$E_{\text{in}} = |E_{\text{bat}}| + |E_{\text{gen}}| \tag{2.9}$$

$$E_{\text{out}} = |E_{\text{mot}}| \tag{2.10}$$

In Mode 2 (regen mode), the generator and the motor are providing charging power to the battery, so the input and output energies can be calculated according to Equations 2.11 and 2.12.

$$E_{\text{in}} = |E_{\text{mot}}| + |E_{\text{gen}}| \tag{2.11}$$

$$E_{\text{out}} = |E_{\text{bat}}| \tag{2.12}$$

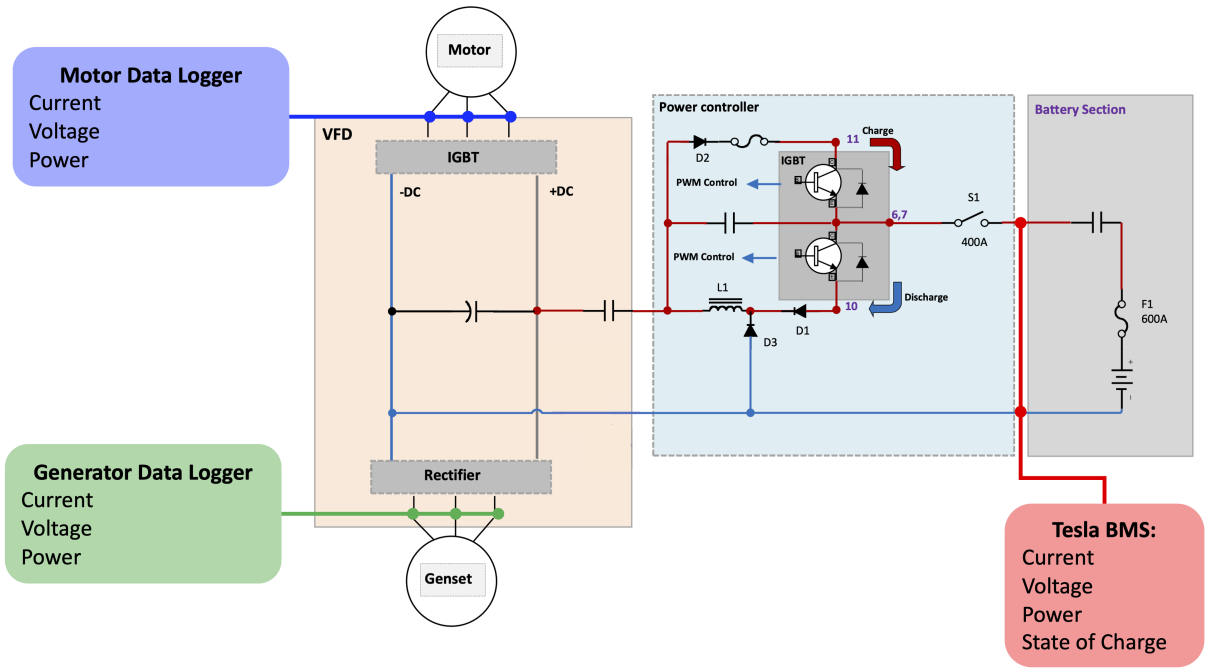

Figure 2.24. Power electronics diagram

Finally, in Mode 3 (drive + charge mode), the generator is providing energy to both the motor and the battery simultaneously, so the input and output energies can be calculated according to Equations 2.13 and 2.14.

$$E_{\text{in}} = |E_{\text{gen}}| \tag{2.13}$$

$$E_{\text{out}} = |E_{\text{mot}}| + |E_{\text{bat}}| \tag{2.14}$$

The fourth combination of power flows, where the battery is providing power and the motor is providing regeneration energy, is not physically possible under the assumption that energy cannot accumulate in the power electronics, so this case is not considered.

These power modes are apparent in the data because of the signs of the battery and motor power flows. As a result, energy flow can be calculated during periods of operation in a given mode, ultimately yielding a short-term efficiency estimate for the power electronics for each period examined.

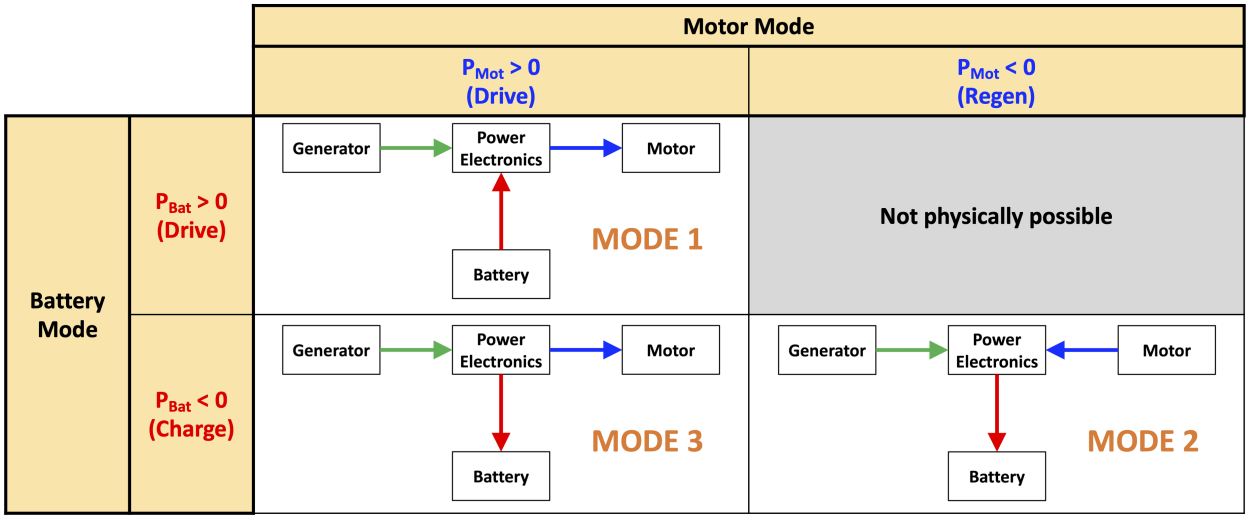

Figure 2.25. Energy flow modes

2.4.2 Energy Accumulation in Power Electronics

As shown in Figure 2.24, the variable frequency drive contains a bank of capacitors between its DC lines to absorb power spikes. The energy stored in this capacitor at any given moment is described in Equation 2.15, where C is capacitance and V is the voltage across the capacitor.

$$E_{\text{capacitor}} = \frac{1}{2}CV^2 \tag{2.15}$$

Because the power flow through the DC portion of the VFD, and by extension the voltage across the capacitor, changes with time, the energy stored in the capacitor also varies with time, yielding the energy balance relation in Equation 2.16.

$$E_{\text{out}} = E_{\text{in}} + \Delta E_{\text{capacitor}} - E_{\text{losses}} \tag{2.16}$$

However, the voltage across the capacitor was not measured, so the capacitor energy storage term, $\Delta E_{\text{capacitor}}$, cannot not be calculated. Over sufficiently long time spans, the change in energy stored in the capacitor is negligible compared to the magnitude of the energy flowing in and out of the power electronics, so the ratio of output energy to input energy is a

good approximation of efficiency, but as sample time is reduced, this approximation becomes less valid, and more outlying efficiency values appear.

All the efficiency values calculated in a single test run are plotted against their sample durations for a Lexington and Indianapolis test run respectively in Figures 2.26 and 2.27. As sample duration increases, efficiency values converge to the mode average, and periods where the vehicle remains in one power mode for less than 15 seconds were not considered, because these results were too unreliable.

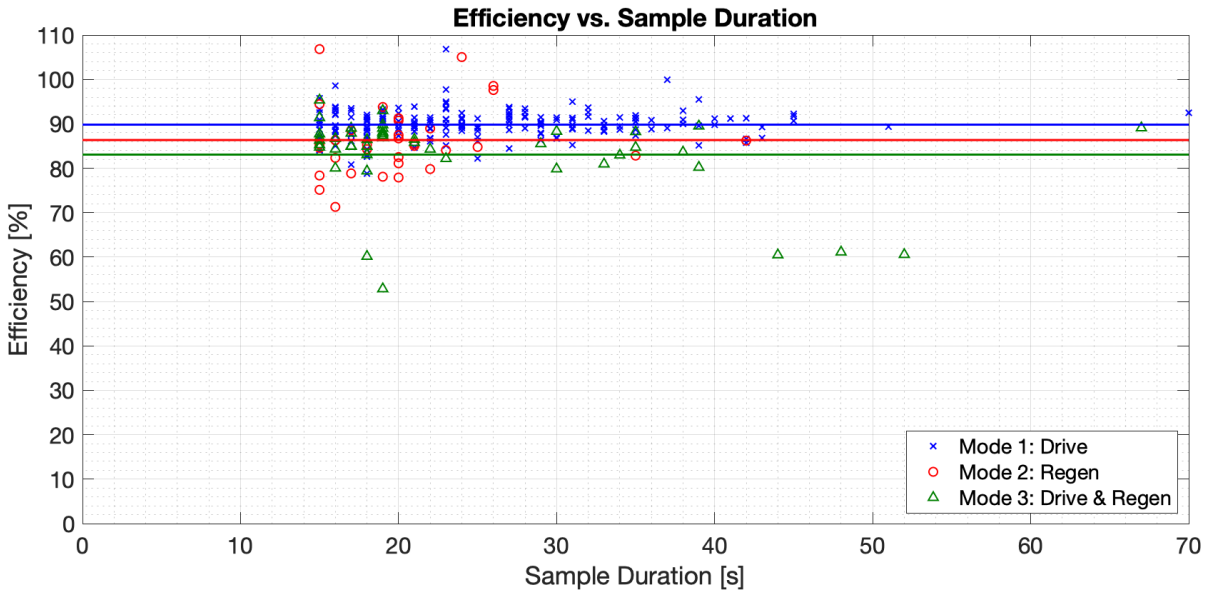

Figure 2.26. Power electronics efficiency versus sample duration Lexington 15 October test

The Lexington route generated outlying efficiency values both below 70% and near or above 100%, and these are clearly not physically accurate. However, closer inspection of the power data for these outlying points reveals that they are characterized by (1) sudden changes in power, (2) low overall energy transfer, or (3) alignment delays between power input and power output. In all three of these scenarios, over a short sample duration, the energy change in the capacitor is significant relative to the total energy transfer, resulting in inaccurate efficiency results. The Lexington test route is generally a more aggressive test environment than the Indianapolis route, causing more sudden changes in power through the power electronics because of grade changes. As a result, all of the Lexington test runs

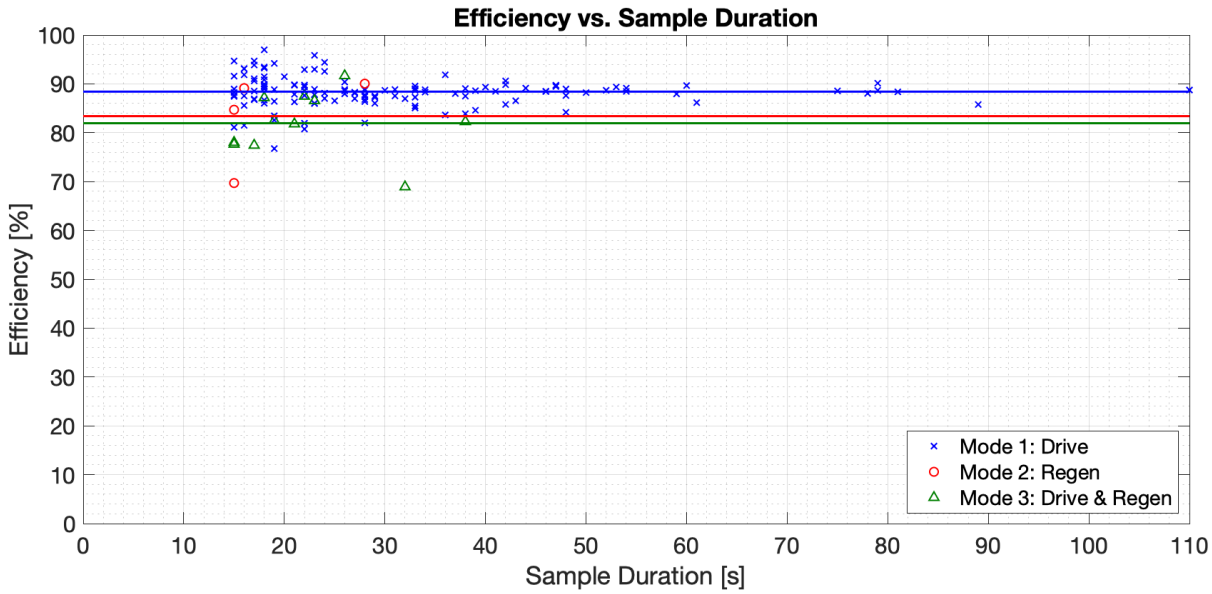

Figure 2.27. Power electronics efficiency versus sample duration Indianapolis 9 January test

exhibit more outlying efficiency values than the Indianapolis test runs. However for almost all test runs, the efficiency values calculated using sample durations greater than 30 - 40 seconds converged to reasonable averages.

2.4.3 Efficiency Results

Despite the outlying efficiencies that sometimes result from samples of less than 30 seconds, the average of all measured efficiency points is reasonable for nine of the runs from which data were gathered. In the remaining runs, time stamps in the battery data logs were recorded incorrectly, as noted in Section 2.2. Because this analysis relies upon the accurate matching of the motor, generator, and battery data streams in the time domain, these problematic data sets are not considered for the power electronics efficiency analysis.

For each of the nine usable data sets, efficiency is calculated for every data segment lasting longer than 15 seconds in one mode (these points are plotted for two runs in Figures 2.26 and 2.27). These efficiencies are then averaged for each mode, giving an average efficiency in each mode for all nine test runs. These average efficiencies are summarized in Table 2.2. All calculated efficiency averages are greater than 80%, which is the expected range. Power

Table 2.2. Power electronics efficiency results

	Mode 1 (Drive)	**Mode 2 (Regen)**	**Mode 3 (Drive + Charge)**
High	91.8%	90.1%	89.5%
Mean	89.5%	86.1%	85.1%
Low	87.8%	82.8%	81.8%

Mode 1, when the battery and generator are sending drive power to the motor, is the most efficient and the most reliable efficiency calculation, as the truck spends most of its total time in this mode, and the sample durations in this mode tend to be longer than for the other two modes. The overall efficiency difference between the three power modes is only a few percentage points, indicating that the power electronics handle power flow in any direction relatively efficiently. Boxplots for the set of average efficiencies in each mode are shown in Figure 2.28, where the red line is the median average efficiency, the blue box contains the middle half of the average efficiency values, and the upper and lower lines indicate the maximum and minimum average efficiency points. This corroborates the result from Table 2.2, showing that power Mode 1 is more efficient than the other two power modes.

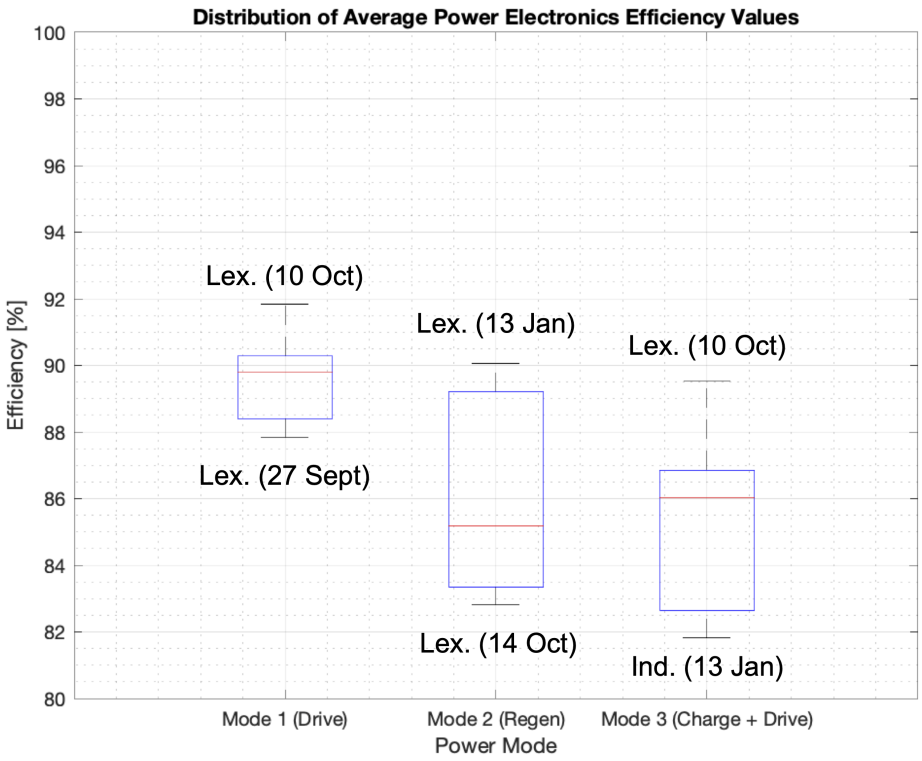

Figure 2.28. Boxplot of average power electronics efficiencies

2.5 Summary of Other Efficiency Results

The modeling and analysis conducted to identify the hybrid drivetrain's mechanisms for efficiency gains and potential for improvement was conducted in cooperation with Shubham Agnihotri, so this work is ommitted, but the results are summarized here briefly.

Two metrics are used to evaluate the test data and meet these objectives: the ratio of motor regeneration energy during testing to regeneration energy theoretically available due to grade and acceleration profile ($E_{\text{regen,test}}/E_{\text{regen,available}}$) and the ratio of regeneration energy to total required drive energy ($E_{\text{regen}}/E_{\text{drive}}$). Both metrics are obtained using test data and a physical vehicle model which represents the forces on the truck due to drag, rolling resistance, road grade, and acceleration profile.

2.5.1 Regeneration Energy Capture Percentage

The ratio $E_{\text{regen,test}}/E_{\text{regen,available}}$ represents the fraction of total available regenerative braking energy the truck is able to capture, and these results are summarized in Figure 2.29. The results indicate that the truck captures approximately 70% of the available energy on tests 18 and 21, but these tests occurred during high winds and low temperatures respectively. High winds increase the relative wind speed of the vehicle, increasing aerodynamic drag, as well as rolling resistance if there is a cross wind component, and low temperatures increase air density and rolling resistance. However, none of these factors was recorded during testing or included in the vehicle model, so the actual regeneration energy available is likely substantially less than the model indicates.

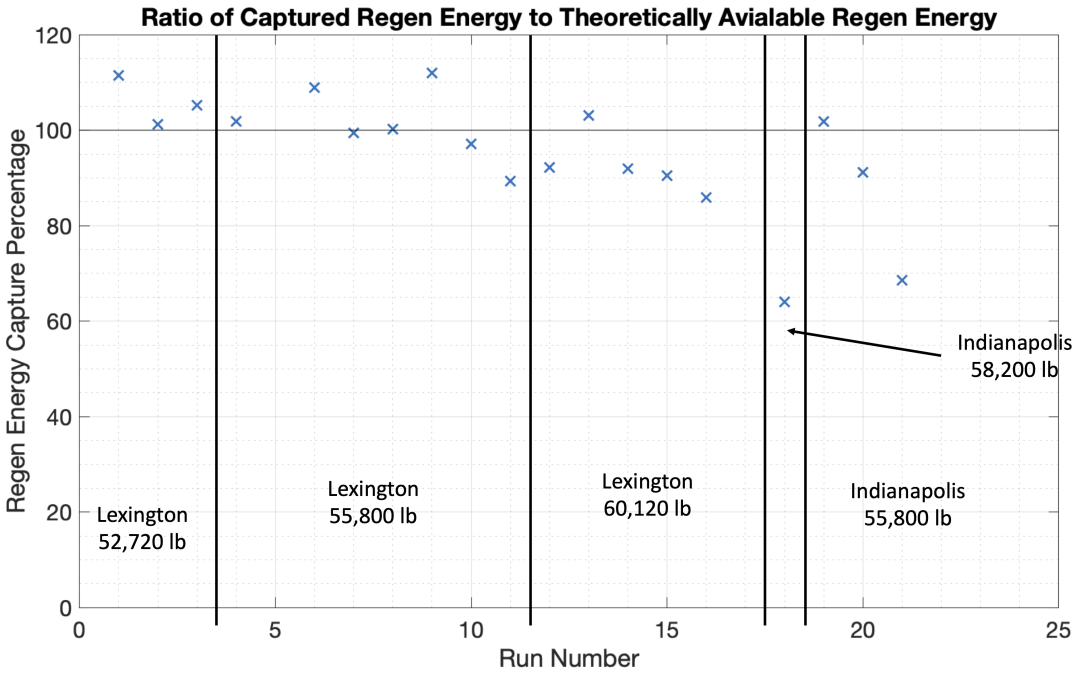

Figure 2.29. Measured motor regeneration energy as fraction of calculated available energy

More notably however, the data indicate that the truck captures more regeneration energy than was actually available for almost half of the test runs, but this discrepancy is due to using fixed values drag and rolling resistance coefficients, C_d and μ. While these coefficients were determined experimentally, they vary with tire temperature, road conditions, and relative

wind direction, so the values obtained in testing can only accurately be applied to test runs under the same conditions. Additionally, no tests were performed with the truck traveling fast enough to obtain a reliable estimate of its drag coefficient, so while the even distribution around 100% indicates that the truck can capture close to 100% of the available regeneration energy, no run-specific conclusions can be drawn.

2.5.2 Ratio of Regeneration Energy Capture to Drive Energy Output

The ratio $E_{\text{regen}}/E_{\text{drive}}$ represents the fraction of total drive energy that regenerative braking provides, which is calculated according to 2.17, where each energy term is obtained from the vehicle model using drive cycle data from testing.

$$\frac{E_{\text{regen}}}{E_{\text{drive}}} = \frac{E_{\text{decel}} + E_{\text{grade,down}}}{E_{\text{accel}} + E_{\text{grade,up}} + E_{\text{rr}} + E_{\text{aero}}} \tag{2.17}$$

These results are summarized in Figure 2.30 for test runs with usable data. Three energy ratio results are plotted for each test run based on: (1) the experimental truck (calculated from motor data), (2) the experimental truck (calculated from its theoretical power requirement), and (3) a reference 2018 Peterbilt 579 truck (calculated from its theoretical power requirement). The theoretical power requirements are calculated using the C_d and μ values shown in Table 2.3. The analytical results for the experimental truck match the experimental results fairly well despite some uncertainty around the experimentally determined C_d and μ coefficients, so it is reasonable to extrapolate the energy ratio calculation to different rolling resistance and drag coefficients.

Table 2.3. Drag and rolling resistance coefficients

Parameter	Test Truck	New Low Mileage Truck
C_d	0.68	0.58
μ	0.007	0.005

In these results, the Lexington profile yields almost double the ratio of regeneration to drive energy compared to the Indianapolis route, which is expected based on the higher battery energy transfer (Section 2.3.4) and rolling hills on the Lexington cycle. This affirms

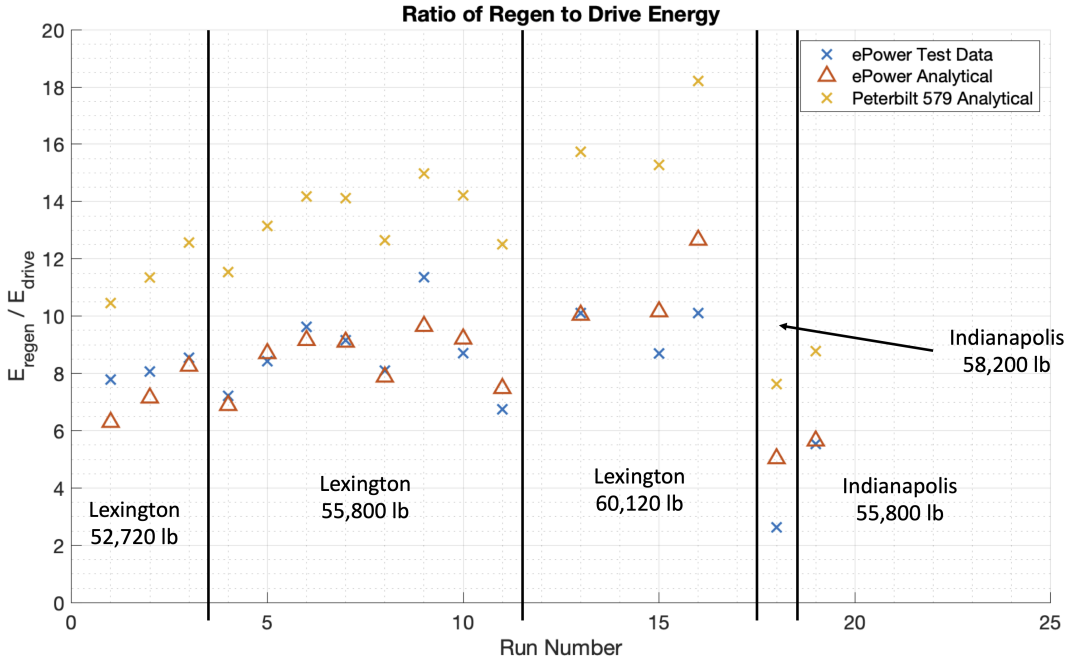

Figure 2.30. Energy ratio results summary

that the drivetrain's opportunity to capture and reuse regenerative braking energy depends heavily a drive cycle's grade profile.

Additionally, decreasing the truck's aerodynamic and rolling drag can potentially improve this energy recapture ratio. All vehicles benefit from drag reduction, because it reduces the propulsive power requirement, but it also increases excess kinetic energy which is typically dissipated through brakes or engine braking. In contrast, the hybrid drivetrain benefits from both the reduction in propulsive energy required to move the vehicle and the additional kinetic energy available, since it can recapture braking energy. If the experimental drivetrain is installed in the comparison Peterbilt 579 truck and trailer, the aerodynamic improvements and reduced rolling resistance due to lower wear could increase the energy capture ratio to 8% - 18% depending on the route.

Finally, the recapture energy ratio increases slightly with mass. Although variation among test runs obscures this trend, the results in Figure 2.30 suggest this relationship, and Equation 2.17 affirms it. Because every term in Equation 2.17 depends on mass except aerodynamic drag, which only occurs in the denominator, the percent increase of regenera-

tion energy is slightly greater than the percent increase of drive energy, yielding a slightly better regeneration energy ratio. Nonetheless, the series hybrid system would benefit most significantly from drag and rolling resistance reductions.

2.6 Future Work

The data from the testbed series hybrid truck shows effective mechanisms for efficiency gains over a standard drivetrain on highway routes, in particular those with mildly hilly terrain. However, three components of the powertrain that were not studied would benefit from further analysis. First, no analysis was conducted on the battery, because its wear and associated efficiency loss was known, and the startup plans to replace it anyway. Nonetheless, a drive profile simulation to evaluate round-trip efficiency of the battery would inform the choice of battery size and chemistry in future powertrain iterations. Battery round-trip efficiency–the ratio of total charge energy to total discharge energy over a drive cycle with the battery starting and ending at the same state of charge–would reveal how much of the captured regeneration energy actually comes back to the motor and how much is lost in the battery as heat.

Second, no analysis was conducted on the engine, because minimal engine data was available. However, a comparison of the brake specific fuel consumption (BSFC) of the test vehicle's engine and a larger, variable speed, standard drivetrain engine would reveal whether running the smaller engine at a constant speed but variable load provides any efficiency gains.

Finally, the architecture of the supervisory control system was not available, so no analysis was conducted on how electrical power is managed. The supervisory control system in a series hybrid drivetrain commands power flows among the generator, battery, and traction motor, and adjustments to this control architecture can yield significant gains in powertrain efficiency and performance. Intuitive rule-based strategies for supervisory control, such as those presented in [24] and [25], provide good energy management performance and are easily tunable, but optimal control methods such as those presented in [26] and [27] provide better overall efficiency by continuously adjusting power flows within the drivetrain to minimize a defined cost function. Additionally, "look ahead" based on prior knowledge of the vehicle's

route can further reduce fuel consumption and engine emissions, as shown in [28]. Even a few seconds foreknowledge of a power demands, both at the supervisory and engine control level can yield significant improvements in efficiency and overall performance.

For this experimental system specifically, a review of the existing control architecture would be useful, particularly with respect to the engine and battery power use. In all vehicle testing, the load placed on the engine varied from zero to the engine's maximum load, so the engine likely spent significant time operating far from its minimum BSFC range. If the supervisory controller could reduce the fluctuation of the power draw from the generator by depending more heavily on the battery, the engine could be operated closer to its minimum BSFC speed and torque range for more of the drive cycle, further improving fuel efficiency, although the round trip efficiency of the battery would become more significant in this case. A new battery optimized to withstand the heavy transient power requirements of hilly highway driving would also enable additional controller optimization in future efforts.

3. CONTROL ORIENTED NONLINEAR STATE SPACE MODEL OF DIESEL ENGINE WITH ELECTRIFIED AIR HANDLING

3.1 Engine Architecture

The experimental engine discussed here and in Chapter 4 is a 4.5-liter, 4 cylinder, diesel engine with a single turbocharger and wastegate, a high pressure exhaust gas recirculation (EGR) loop, and an exhaust throttle. An electrically driven supercharger (eBooster) and bypass valve after the turbocharger compression stage boost transient torque response, allowing the engine to replace the existing 6.8-liter engine in John Deere's 644K hybrid electric wheel loader. This engine architecture is represented in Figure 3.1 along with the the locations of states used in modeling and actuators available for control.

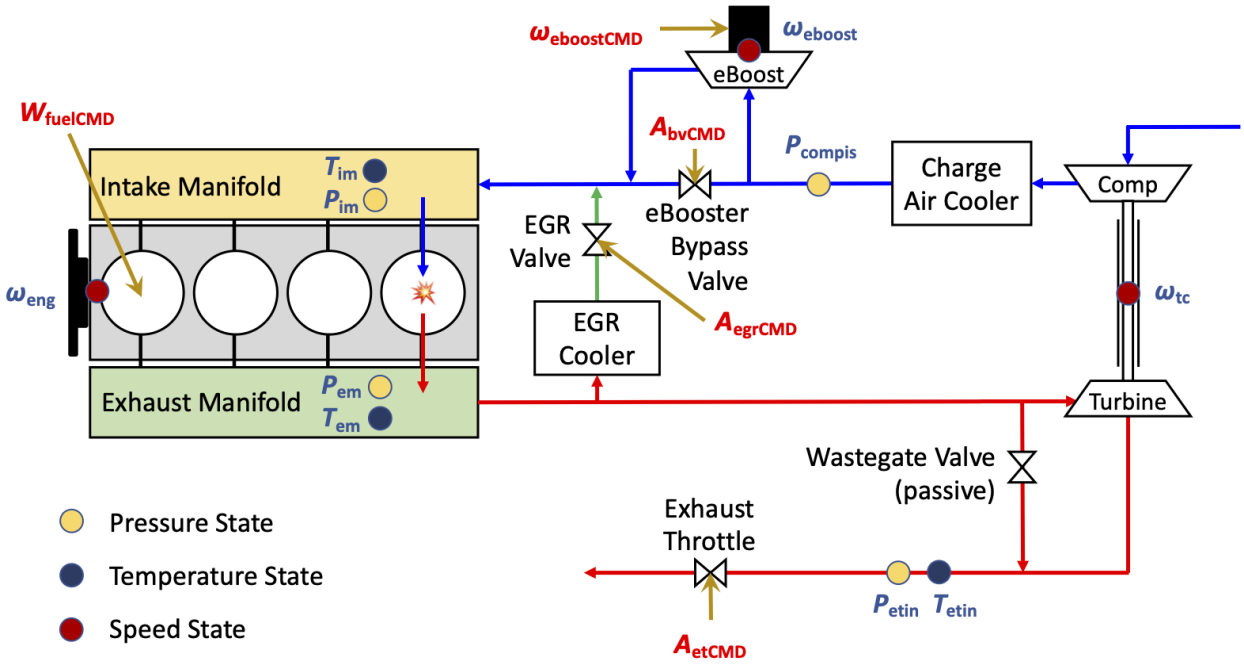

Figure 3.1. Engine air handling system diagram

3.2 Nonlinear State Space Model

The mean value model developed for this architecture is a nonlinear state space model of the form described in Equation 3.1,

$$\dot{x} = f(x, u, u_{\mathrm{d}}) \tag{3.1a}$$

$$y = g(x, u) \tag{3.1b}$$

where x is the vector of states, u is the set of controllable inputs, u_{d} is the set of disturbance inputs, and y is the vector of state outputs. This state space model is used to simulate engine operation as shown in Figure 3.2.

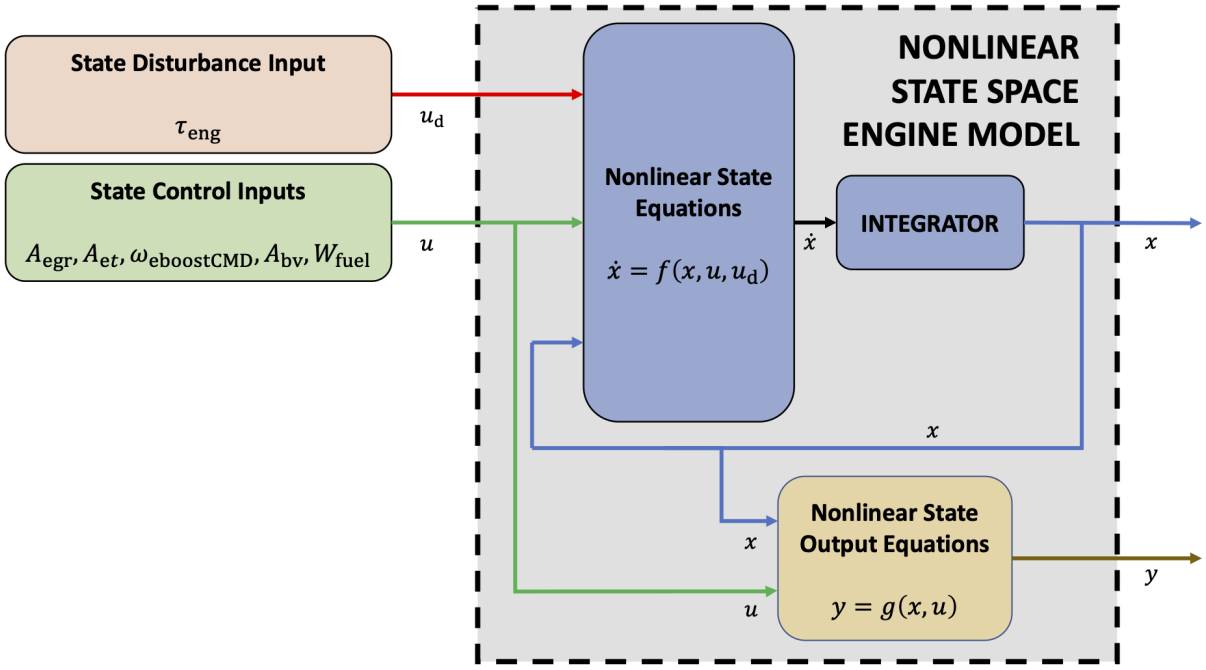

Figure 3.2. Nonlinear state space model simulation framework

Ten first order, nonlinear differential equations (Equations 3.2a - 3.2j) for the states described in Table 3.1 are marked by circles and blue text in Figure 3.1. The model's four pressure states (Equations 3.2a - 3.2d) and three temperature states (Equations 3.2e - 3.2g) are obtained from first law thermodynamic analysis of the various manifold volumes. Of

Table 3.1. Nonlinear mean value model states

State	Variable	Description	Units
x_1	P_{compis}	Compressor interstage pressure	Pa
x_2	P_{im}	Intake manifold pressure	Pa
x_3	P_{em}	Exhaust manifold pressure	Pa
x_4	P_{etin}	Exhaust throttle inlet pressure	Pa
x_5	T_{im}	Intake manifold temperature	K
x_6	T_{em}	Exhaust manifold temperature	K
x_7	T_{etin}	Exhaust throttle inlet temperature	K
x_8	ω_{tc}	Turbocharger shaft speed	rad/s
x_9	ω_{eboost}	eBooster shaft speed	rad/s
x_{10}	ω_{eng}	Engine shaft speed	rad/s

the three rotation speed states (Equations 3.2h - 3.2j), the turbocharger and engine speeds are derived from a torque balance about their respective shafts, but the eBooster speed is modeled as a first order response to its commanded speed. The eBooster has its own internal controller which tracks a shaft speed command by controlling motor power, and this

first order linear model represents the eBooster's response to its controller reasonably well, eliminating the need for a state derived from a shaft torque balance.

$$\dot{x}_1 = \dot{P}_{\text{compis}} = \frac{\gamma_{\text{amb}} R}{V_{\text{compis}}}[W_{\text{comp}} T_{\text{cac}} - W_{\text{eboost}} T_{\text{cac}} - W_{\text{bv}} T_{\text{cac}}] \tag{3.2a}$$

$$\dot{x}_2 = \dot{P}_{\text{im}} = \frac{\gamma_{\text{im}} R}{V_{\text{im}}}[W_{\text{egr}} T_{\text{egr}} + W_{\text{eboost}} T_{\text{eboost,out}} + W_{\text{bv}} T_{\text{cac}} - W_{\text{cyl}} T_{\text{im}}] \tag{3.2b}$$

$$\dot{x}_3 = \dot{P}_{\text{em}} = \frac{\gamma_{\text{ex}} R}{V_{\text{em}}}[W_{\text{cylout}} T_{\text{cylout}} - (W_{\text{turb}} + W_{\text{wg}} + W_{\text{egr}}) T_{\text{em}}] \tag{3.2c}$$

$$\dot{x}_4 = \dot{P}_{\text{etin}} = \frac{\gamma_{\text{ex}} R}{V_{\text{etin}}}[W_{\text{wg}} T_{\text{em}} + W_{\text{turb}} T_{\text{turb,out}} - W_{\text{et}} T_{\text{etin}}] \tag{3.2d}$$

$$\begin{aligned}\dot{x}_5 = \dot{T}_{\text{im}} = \frac{R T_{\text{im}}}{P_{\text{im}} V_{\text{im}}}[&W_{\text{egr}}(\gamma_{\text{ex}} T_{\text{egr}} - T_{\text{im}}) + W_{\text{eboost}}(\gamma_{\text{amb}} T_{\text{eboost,out}} - T_{\text{im}}) + \\ &W_{\text{bv}}(\gamma_{\text{amb}} T_{\text{cac}} - T_{\text{im}}) - W_{\text{cyl}}(\gamma_{\text{im}} T_{\text{im}} - T_{\text{im}})]\end{aligned} \tag{3.2e}$$

$$\begin{aligned}\dot{x}_6 = \dot{T}_{\text{em}} = \frac{R T_{\text{em}}}{P_{\text{em}} V_{\text{em}}}[&W_{\text{cylout}}(\gamma_{\text{ex}} T_{\text{cylout}} - T_{\text{em}}) - \\ &(W_{\text{turb}} + W_{\text{wg}} + W_{\text{egr}})(\gamma_{\text{ex}} T_{\text{em}} - T_{\text{em}})]\end{aligned} \tag{3.2f}$$

$$\begin{aligned}\dot{x}_7 = \dot{T}_{\text{etin}} = \frac{R T_{\text{etin}}}{P_{\text{etin}} V_{\text{etin}}}[&W_{\text{wg}}(\gamma_{\text{ex}} T_{\text{em}} - T_{\text{etin}}) + W_{\text{turb}}(\gamma_{\text{ex}} T_{\text{turb,out}} - T_{\text{etin}}) - \\ &W_{\text{et}}(\gamma_{\text{ex}} T_{\text{etin}} - T_{\text{etin}})]\end{aligned} \tag{3.2g}$$

$$\dot{x}_8 = \dot{\omega}_{\text{tc}} = \frac{Z_{\text{turb}} - Z_{\text{comp}} - Z_{\text{loss}}}{I_{\text{tc}} \omega_{\text{tc}}} \tag{3.2h}$$

$$\dot{x}_9 = \dot{\omega}_{\text{eboost}} = (\omega_{\text{eboostCMD}} - \omega_{\text{eboost}}) \mathcal{T}_{eboost} \tag{3.2i}$$

$$\dot{x}_{10} = \dot{\omega}_{\text{eng}} = \frac{C_{\text{trq}} P_{\text{im}} - \tau_{\text{eng}}}{I_{\text{eng}}} \tag{3.2j}$$

Five actuators are available for control on the engine, and they effect the nonlinear model either directly through the state equations or through the submodels presented in section 3.3. These actuators are shown in Figure 3.1 as red text and are summarized in Table 3.2.

Table 3.2. Engine actuators

Input	Variable	Description	Units
u_1	A_{egr}	Effective EGR valve area	m^2
u_2	A_{et}	Effective exhaust throttle area	m^2
u_3	$\omega_{\text{eboostCMD}}$	eBooster shaft speed command	rad/s
u_4	A_{bv}	Effective bypass valve area	m^2
u_5	W_{fuel}	Fueling rate	kg/s
u_d	τ_{eng}	External load torque (disturbance)	Nm

Three state outputs are specified in Equations 3.3a - 3.3c and summarized in Table 3.3. The in-cylinder EGR fraction and air fuel ratio are technically dynamic states that do not respond immediately to changes in the flow rates from which they are calculated, but the manifold volumes are small enough in this engine that these parameters respond almost immediately to changes in flow rate. As a result, they are modeled as ratios of internal parameters, rather than dynamic states.

$$y_1 = F_{\text{egr}} = \frac{W_{\text{comp}}}{W_{\text{egr}}} \tag{3.3a}$$

$$y_2 = \text{AFR} = \frac{W_{\text{cyl}} - W_{\text{egr}}}{W_{\text{fuel}}} \tag{3.3b}$$

$$y_3 = \omega_{\text{eng}} = x_{10} \tag{3.3c}$$

Table 3.3. State outputs

Output	Variable	Description	Units
y_1	F_{egr}	Intake manifold EGR fration	-
y_2	AFR	Air-Fuel Ratio	-
y_3	ω_{eng}	Engine shaft speed	rad/s

The letters and subscripts used in Equations 3.2 and 3.3 are defined in Tables 3.4 and 3.5 respectively, and all terms used in the state equations are defined in Section 3.3. Additionally this nonlinear model is tuned to match a GT-Power engine model taken as a truth reference,

and validation results for the nonlinear model are presented in Chapter 4 along with results from two linearized models.

Table 3.4. Letter assignments

Letter	**Meaning**	**Units**
γ	Specific heat ratio	-
C_{trq}	Engine torque coefficient	-
I	Inertia	kg·m^2
P	Pressure	Pa
R	Mass-specific gas constant	J/kg·K
$\mathcal{T}_{\text{eboost}}$	Time constant	s
τ_{eng}	Torque	Nm
T	Temperature	K
V	Volume	m^3
ω	Shaft speed	rad/s
W	Flow rate	kg/s
Z	Power	W

Table 3.5. Subscript definitions

Subscript	Description
amb	Ambient
cac	Charge air cooler
compis	Compressor interstage
im	Intake manifold
em	Exhaust manifold
egr	Exhaust gas recirculation
etin	Exhaust throttle inlet
tc	Turbocharger
comp	Compressor
turb	Turbine
loss	Shaft losses
wg	Wastegate
eboost	eBooster
bv	Bypass valve
eng	Engine
ex	Exhaust

3.3 Submodels Used in Nonlinear State Space Model

Several submodels are used to calculate parameters in the the engine model state equations. These submodels are developed from [18], [29], [30] and implemented as standalone MATLAB functions, which the MATLAB and Simulink based engine model calls, facilitating a modular overall model structure. Additionally, every parameter from Equations 3.2 and 3.3 is listed in Table 3.6 with a brief description, its type, and the section describing its submodel if applicable.

Table 3.6. Terms used in state equations

Parameter	Description	Type	Value
W_{comp}	Turbocharger compressor flow	submodel	Section 3.3.2
W_{eboost}	eBooster compressor flow	submodel	Section 3.3.1
W_{bv}	eBooster bypass valve flow	submodel	Section 3.3.8
W_{cyl}	Total flow into all cylinders	submodel	Section 3.3.9
W_{cylout}	Total flow out of all cylinders	simple sum	$W_{\text{cyl}} + W_{\text{fuel}}$
W_{egr}	EGR flow	submodel	Section 3.3.8
W_{turb}	Turbocharger turbine flow	submodel	Section 3.3.4
W_{wg}	Turbocharger wastegate flow	submodel	Section 3.3.8
W_{et}	Exhaust throttle flow	submodel	Section 3.3.8
Z_{comp}	Turbocharger compressor power	submodel	Section 3.3.3
Z_{turb}	Turbocharger turbine power	submodel	Section 3.3.5
Z_{loss}	Frictional windage loss	submodel	Section 3.3.6
P_{compis}	Compressor interstage pressure	state	
P_{im}	Intake manifold pressure	state	
P_{em}	Exhaust manifold pressure	state	
P_{etin}	Exhaust throttle inlet pressure	state	
T_{cac}	CAC outlet temperature	constant	307 K
$T_{\text{eboost,out}}$	eBooster outlet temperature	submodel	Section 3.3.11
T_{egr}	EGR cooler outlet temperature	constant	350 K
T_{im}	Intake manifold temperature	state	
T_{cylout}	Cylinder outlet temperature	submodel	Section 3.3.10
T_{em}	Exhaust manifold temperature	state	
$T_{\text{turb,out}}$	Turbine outlet temperature	simple equality	T_{em}
T_{etin}	Exhaust throttle inlet temperature	state	
C_{trq}	Engine torque coefficient	submodel	Section 3.3.12
τ_{eng}	External load torque	disturb. input	
V	Volumes	constant	
γ	Specific heat ratios	constant	
R	Gas constant	constant	287 J/kg·K
I	Inertias	constant	
ω_{tc}	Turbocharger speed	state	
ω_{eboost}	eBooster speed	state	
$\omega_{\text{eboostCMD}}$	eBooster speed command	input	
$\mathcal{T}_{\text{eboost}}$	eBooster time constant	constant	0.1 s

3.3.1 eBooster Compressor Flow

The engine uses a high pressure eBooster compressor and a low pressure turbocharger compressor (Figure 3.1) to boost intake manifold pressure, and the flow through these compression stages is used to calculate turbocharger power and state derivatives. The eBooster compressor flow is modeled according to the map reduction approach presented in [30], where the two-dimensional compressor map is nondimensionalized to allow a one-dimensional polynomail fit to describe the map. With this approach, flow is calculated as follows:

$$W_{\text{eboost}} = \left[\frac{\pi}{4}\rho_{\text{in}}d^2\left(\frac{1}{\gamma R T_{\text{in}}}\right)^{\frac{\gamma-1}{2\gamma}}\left(\frac{\pi}{60}d\omega\right)^{\frac{2\gamma-1}{\gamma}}\right]\left(a_3X^3+a_2X^2+a_1X+a_0\right) \tag{3.4a}$$

$$X = \frac{c_p T_{\text{in}}\left(PR^{\frac{\gamma-1}{\gamma}}-1\right)}{\frac{1}{2}\left(\frac{\pi}{60}d\omega\right)^2} \tag{3.4b}$$

$$PR = \frac{P_{\text{out}}}{P_{\text{in}}} \tag{3.4c}$$

All parameters in Equations 3.4 are listed in Table 3.7, and the values used for the regression fit constants, a_1, a_2, a_3, and a_4 are shown in Table 3.8.

Table 3.7. Parameters in eBooster compressor flow model

Parameter	Description	Value	Units
ρ_{in}	Inlet density	$P_{\text{in}}/(RT_{\text{in}})$	kg/m^3
d	Compressor blade tip diameter	0.065	m
γ	Specific heat ratio	1.4	-
R	Gas constant	287	J/kg·K
T_{in}	Inlet temperature	state	K
ω	eBooster haft speed	state	rad/s
c_{p}	Specific heat (constant pressure)	1003	J/kg·K
P_{out}	Outlet pressure = P_{im}	state	Pa
P_{in}	Inlet pressure = P_{compis}	state	Pa

The map fit using this modeling approach is shown in Figure 3.3 on top of the original manufacturer provided map data. The eBooster generally operates in the low pressure ratio

Table 3.8. Regression fit coefficients in eBooster compressor flow model

Coefficient	Value
a_3	0
a_2	-0.0542
a_1	-0.0159
a_0	0.2165

range for each shaft speed, so the map is tuned to fit well in this region. Although the fit is poor in the low flow rate area of the map when the compressor is near surge, the eBooster does not reach this area during normal operation.

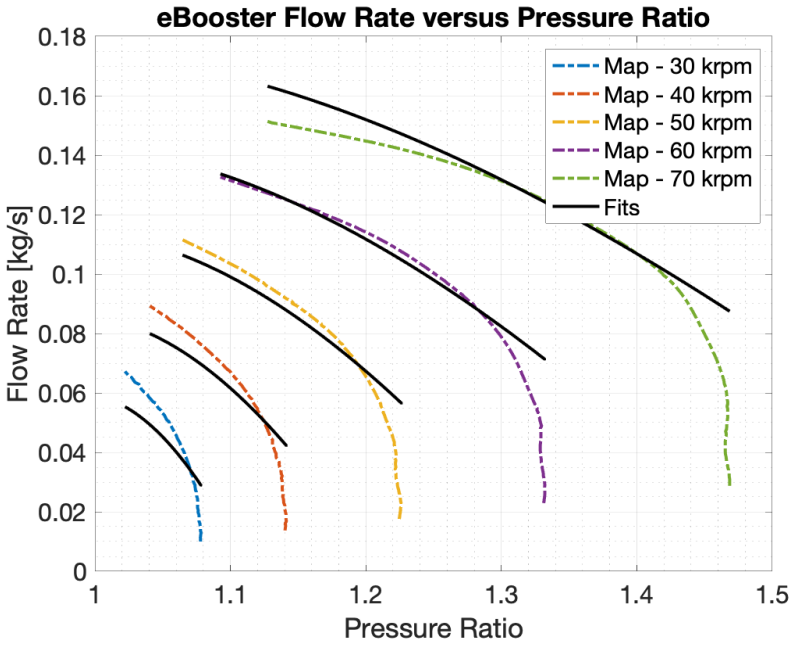

Figure 3.3. eBooster compressor map

3.3.2 Turbocharger Compressor Flow

The method for compressor modeling presented in Section 3.3.1 does not represent the turbocharger compressor map with enough accuracy, because the nondimensionalization approach used in [30] does not collapse the map in such a way that a single variable polynomial could adequately describe in. Instead the following regression surface fit represents the map

much better using a two dimensional polynomail that is third order in pressure ratio and second order in compressor speed,

$$W_{\text{comp}} = a_{00} + a_{01}PR + a_{02}PR^2 + a_{03}PR^3 + a_{10}\omega + a_{11}PR\omega + a_{12}PR^2\omega + a_{20}\omega^2 + a_{21}PR\omega^2 \tag{3.5a}$$

$$PR = \frac{P_{\text{out}}}{P_{\text{in}}} \tag{3.5b}$$

where inlet pressure to the compressor, P_{in}, is the constant ambient pressure, the outlet pressure, P_{out}, is the interstage pressure state, P_{compis}, and the shaft speed, ω, is the turbocharger shaft speed. The values of the regression fit coefficients are shown in Table 3.9, and the resulting fit for the turbocharger compressor map using this modeling approach is shown in Figure 3.4 on top of the original manufacturer provided map data.

Table 3.9. Regression fit coefficients in turbocharger compressor flow model

Coefficient	**Value**
a_{00}	0.0777
a_{01}	0.4443
a_{02}	-0.5199
a_{03}	-0.0415
a_{10}	-0.6307 $\times 10^{-5}$
a_{11}	0.5159 $\times 10^{-5}$
a_{12}	0.4549 $\times 10^{-5}$
a_{20}	0.4431 $\times 10^{-10}$
a_{21}	0.5946 $\times 10^{-10}$

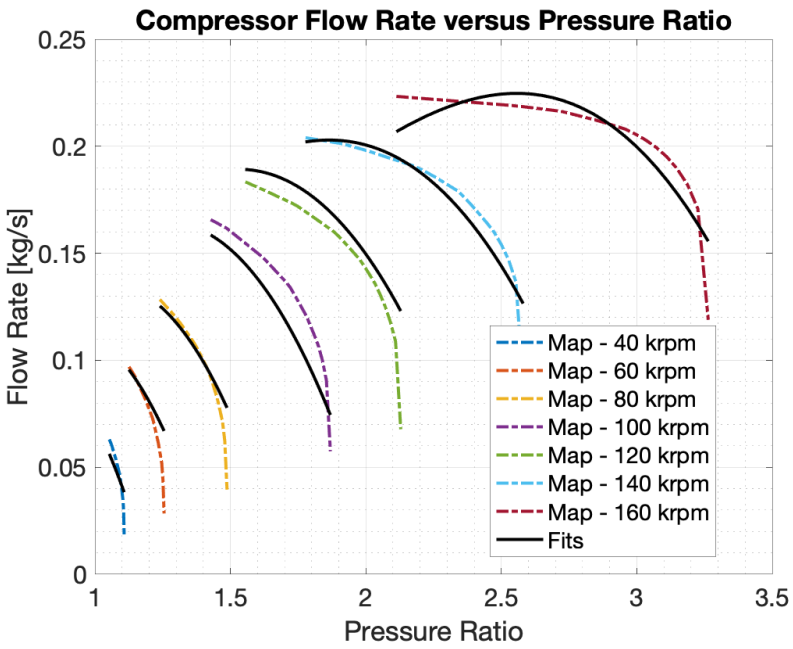

Figure 3.4. Turbocharger compressor map

3.3.3 Turbocharger Compressor Power

The compressor's power consumption is obtained from a thermodynamic energy balance and is calculated according to Equation 3.6:

$$Z_{\text{comp}} = \frac{W_{\text{comp}} c_{\text{p}} T_{\text{in}}}{\eta_{\text{comp}}} \left[PR^{\frac{\gamma-1}{\gamma}} - 1 \right] \tag{3.6a}$$

$$PR = \frac{P_{\text{out}}}{P_{\text{in}}} \tag{3.6b}$$

The compressor efficiency, η is assumed to be constant, because it is consistent within 5% for the relevant operating range of the engine. The assumed value for efficiency and all parameters in Equation1 3.6a and 3.6a are listed in Table 3.10.

Table 3.10. Parameters in turbocharger compressor power model

Parameter	Description	Value	Units
W_{comp}	Compressor flow rate	Section 3.3.2	kg/s
c_{p}	Specific heat (constant pressure)	1003	J/kg·K
T_{in}	Inlet temperature = T_{amb}	300	K
η_{comp}	Compressor efficiency	0.69	-
γ	Specific heat ratio	1.4	-
P_{out}	Outlet pressure = P_{compis}	state	Pa
P_{in}	Inlet pressure = P_{amb}	98,735	Pa

3.3.4 Turbine Flow

The turbine is also modeled using a surface fit with a two dimensional polynomial that is third order in pressure ratio and first order in reduced turbine speed. The polynomial relates reduced turbine flow to pressure ratio and reduced turbine speed, then actual turbine flow rate is obtained from this reduced flow rate and the turbine inlet pressure and temperature:

$$W_{\text{turb}} = W_{\text{turb,red}} \frac{P_{\text{in}}}{1000\sqrt{T_{\text{in}}}} \tag{3.7a}$$

$$W_{\text{turb,red}} = a_{00} + a_{01}PR + a_{02}PR^2 + a_{03}PR^3 + a_{10}N_{\text{red}} + a_{11}N_{\text{red}}PR + a_{12}N_{\text{red}}PR^2 \tag{3.7b}$$

$$PR = \frac{P_{\text{in}}}{P_{\text{out}}} \tag{3.7c}$$

$$N_{\text{red}} = \frac{\omega}{\sqrt{T_{\text{in}}}} \tag{3.7d}$$

All parameters in Equations 3.7 are listed in Table 3.11, and the values of the regression fit coefficients are shown in Table 3.12. The resulting fit is shown in Figure 3.5 on top of the original manufacturer provided map data.

Table 3.11. Parameters in turbine flow model

Parameter	Description	Value	Units
$W_{\text{turb,red}}$	Reduced turbine flow rate	Equation 3.7b	kg/s·$\sqrt{\text{K}}$/kPa
N_{red}	Reduced turbine speed	Equation 3.7d	rpm/$\sqrt{\text{K}}$
T_{in}	Inlet temperature = T_{em}	state	K
ω	Turbocharger shaft speed	state	rad/s
P_{in}	Inlet pressure = P_{em}	state	Pa
P_{out}	Outlet pressure = P_{etin}	state	Pa

Table 3.12. Regression fit coefficients in turbocharger turbine flow model

Coefficient	Value
a_{00}	-0.0222
a_{01}	0.0394
a_{02}	-0.0136
a_{03}	0.1497 $\times 10^{-2}$
a_{10}	-0.1481 $\times 10^{-5}$
a_{11}	0.8447 $\times 10^{-6}$
a_{12}	-0.1289 $\times 10^{-6}$

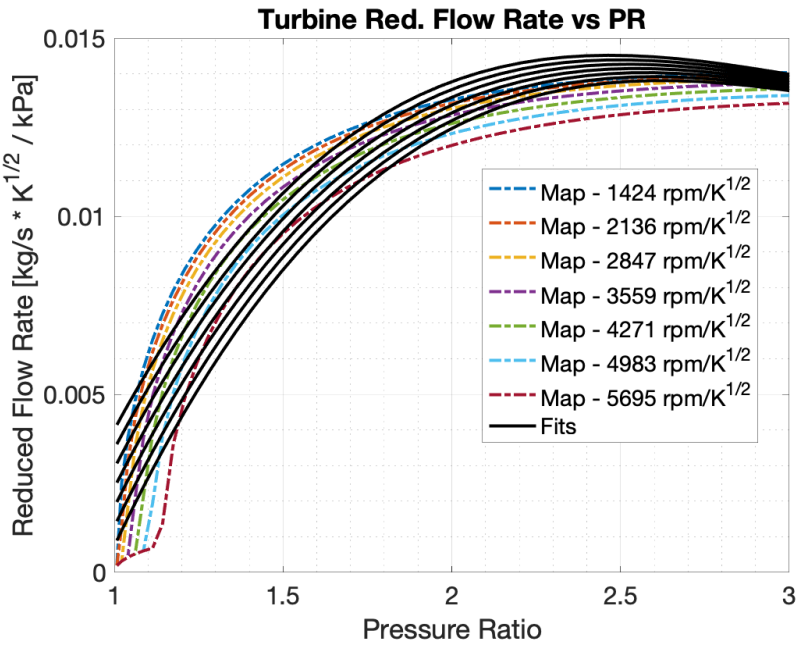

Figure 3.5. Turbocharger turbine map

3.3.5 Turbine Power

The turbine's power consumption is obtained from a thermodynamic energy balance and is calculated according to Equation 3.8:

$$Z_{\text{turb}} = W_{\text{turb}} c_{\text{p}} T_{\text{in}} \eta_{\text{comp}} \left[1 - \frac{P_{\text{out}}}{P_{\text{in}}}\right]^{\frac{\gamma-1}{\gamma}} \tag{3.8}$$

Like the compressor efficiency, the turbine efficiency, η is assumed to be constant, because it is consistent within 5% for the relevant operating range of the engine. The assumed values for efficiency and all other parameters in Equation 3.8 are listed in Table 3.13.

Table 3.13. Parameters in turbocharger turbine power model

Parameter	Description	Value	Units
W_{turb}	Turbine flow rate	Section 3.3.4	kg/s
c_{p}	Specific heat (constant pressure)	1107	J/kg·K
T_{in}	Inlet temperature = T_{em}	state	K
η_{turb}	Turbine efficiency	0.63	-
γ	Specific heat ratio	1.35	-
P_{out}	Outlet pressure = P_{etin}	state	Pa
P_{in}	Inlet pressure = P_{em}	state	Pa

3.3.6 Turbocharger Windage Loss

The turbocharger windage loss due to friction is modeled as a reduction in power that is a function of turbocharger shaft speed, ω according to the following equation:

$$Z_{\text{loss}} = a_3\omega^3 + a_2\omega^2 + a_1\omega + a_0 \tag{3.9}$$

Data from the GT-Power reference engine model is used to obtain the regression coefficients shown in Table 3.14, and the resulting fit is shown in Figure 3.6.

Table 3.14. Regression fit coefficients in turbocharger windage loss model

Coefficient	Value
a_0	-0.0222
a_1	0.0394
a_2	-0.0136
a_3	0.1497×10^{-2}

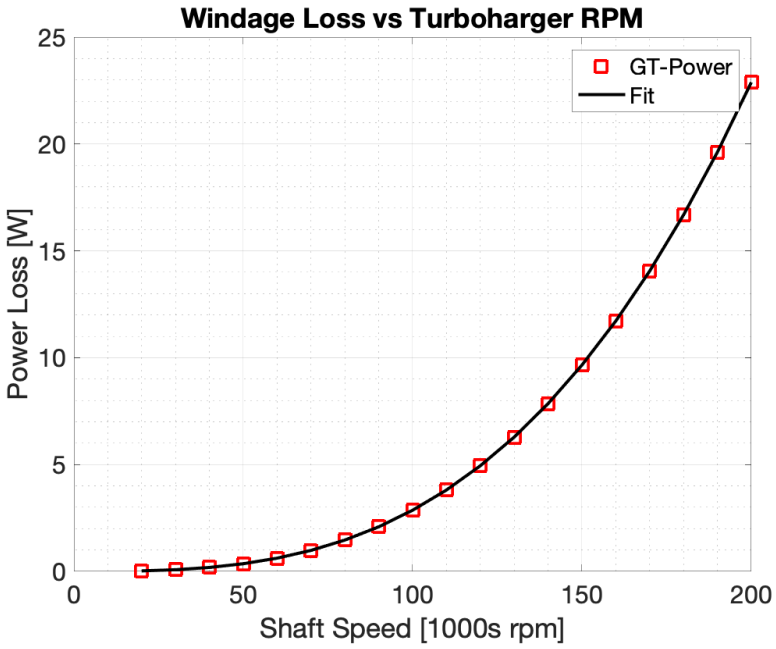

Figure 3.6. Turbocharger windage loss

3.3.7 Turbine Wastegate

The turbocharger wastegate is mechanically connected with a spring to the turbocharger compressor outlet, so the wastegate valve position is a function of the compressor outlet pressure state, P_{compis}. The flow through the wastegate is calculated using the valve submodel in Section 3.3.8, but the effective valve area, A, is obtained from an emperical relation between P_{compis} and the wastegate forward discharge coefficient, C_{d}. However, the emperical

relation is only valid for P_{compis} values between 245 kPa and 270 kPa; below 245 kPa, the wastegate is completely shut, and above 270 kPa the wastegate is fully open.

$$A = C_{\text{d}}\pi\left(\frac{d_{\text{wg}}}{2}\right)^2 \tag{3.10a}$$

$$C_{\text{d}} = a_5 P_{\text{compis}}^5 + a_4 P_{\text{compis}}^4 + a_3 P_{\text{compis}}^3 + a_2 P_{\text{compis}}^2 + a_1 P_{\text{compis}} + a_0 \tag{3.10b}$$

C_{d} is wastegate discharge coefficient, d_{wg} is the wastegate orifice diameter, and P_{compis} is the compressor interstage pressure state in kPa. The values used for the regression coefficients are listed in Table 3.15, and the resulting fit is shown in Figure 3.7.

Table 3.15. Regression fit coefficients in wastegate effective valve area model

Coefficient	**Value**
a_0	-4.148 $\times 10^{5}$
a_1	8.008
a_2	-0.6184 $\times 10^{-4}$
a_3	0.2387 $\times 10^{-9}$
a_4	-0.4607 $\times 10^{-15}$
a_5	0.3556 $\times 10^{-21}$

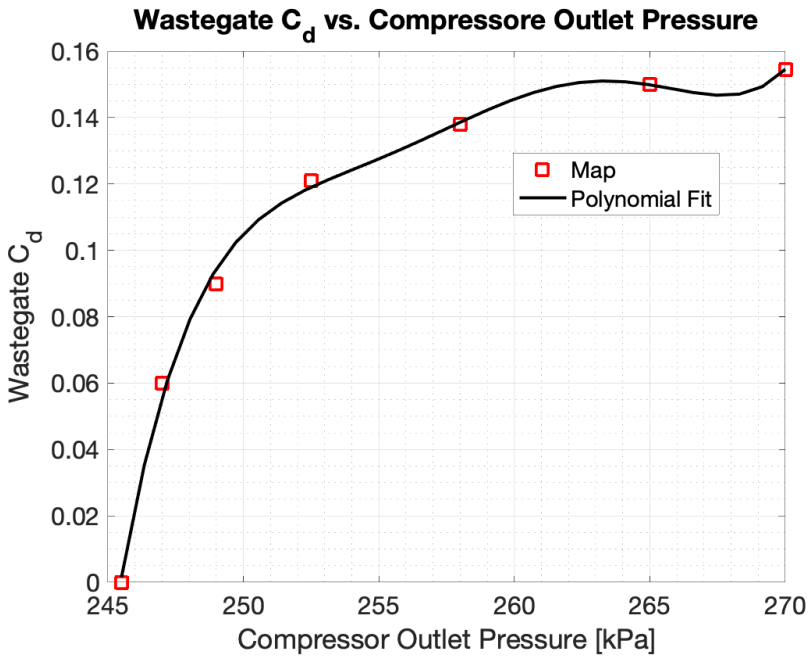

Figure 3.7. Wastegate forward discharge coefficient regression fit

3.3.8 Valve Flow

The mass flow rates through the eBooster bypass valve, EGR valve, wastegate, and exhaust throttle are all modeled by the standard orifice equation and a linearization of the orifice equation for pressure ratios near 1 [18].

$$W_{\text{valve}} = A\frac{P_{\text{in}}}{\sqrt{RT_{\text{in}}}}\Psi \tag{3.11a}$$

$$\Psi = \begin{cases} \Psi_0 & PR < \Pi_{\text{linear}} \\ \frac{1-\Pi}{1-\Pi_{\text{linear}}}\Psi_0 & PR_{\text{linear}} < PR \end{cases} \tag{3.11b}$$

$$\Psi_0 = \sqrt{\frac{2\gamma}{\gamma-1}\left(\Pi^{\frac{2}{\gamma}} - \Pi^{\frac{\gamma+1}{\gamma}}\right)} \tag{3.11c}$$

$$\Pi = \begin{cases} PR_{\text{crit}} & PR < PR_{\text{crit}} \\ PR & PR_{\text{crit}} < PR < PR_{\text{linear}} \\ PR_{\text{linear}} & PR_{\text{linear}} < PR \end{cases} \tag{3.11d}$$

$$PR = \frac{P_{\text{out}}}{P_{\text{in}}} \tag{3.11e}$$

$$PR_{\text{crit}} = \left(\frac{2}{\gamma + 1}\right)^{\frac{\gamma}{\gamma - 1}} \tag{3.11f}$$

Here the critical pressure ratio, PR_{crit} is the pressure ratio below which flow through the orifice is choked, and PR_{linear} is the pressure ratio (less than 1) above which the linear Taylor expansion approximation to the orifice equation is applied. All parameters used in the valve model are listed in Table 3.16.

Table 3.16. Parameters in valve model

Parameter	**Description**	**Value (eBooster Bypass Valve)**	**Value (EGR Valve)**	**Value (Waste-gate)**	**Value (Exhaust Throttle)**	**Units**
A	Effective valve area	cmd	cmd	Section 3.3.7	cmd	m^2
R	Gas constant	287	287	287	287	J/kg·K
T_{in}	Inlet temperature	300	350	T_{em} (state)	T_{etin} (state)	K
γ	Specific heat ratio	1.4	1.35	1.35	1.35	-
P_{out}	Outlet pressure	P_{im} (state)	P_{im} (state)	P_{etin} (state)	104,000	Pa
P_{in}	Inlet pressure	P_{compis} (state)	P_{em} (state)	P_{em} (state)	P_{etin} (state)	Pa

3.3.9 Cylinder Charge Flow

In the actual engine, charge gases enter a cylinder only when its intake valves are open, and this timing is different for each cylinder due to cycle offsets among the cylinders. However, for the purposes of the mean value model, the charge flow is averaged to provide a mean total charge flow rate through all four cylinders using the speed density equation for a single, four cycle cylinder , then multiplying this flow rate by the number of cylinders in the engine.

$$W_{\text{cyl}} = N_{\text{cyl}}\eta_{\text{vol}}\frac{P_{\text{im}}V_{\text{disp}}}{RT_{\text{im}}}\frac{\omega_{\text{eng}}}{120} \tag{3.12}$$

The volumetric efficiency, η_{vol}, of each cylinder is consistent within 2% throughout the engine's operating range of interest, so a constant value is assumed. This value is listed along with all other charge flow model parameters in Table 3.17.

Table 3.17. Parameters in charge flow model

Parameter	Description	Value	Units
N_{cyl}	Number of cylinders	4	-
η_{vol}	Volumetric efficiency	0.91	-
V_{disp}	Displacement of single cylinder	1.131×10^{-3}	m^3
R	Gas constant	287	J/kg·K
P_{im}	Intake manifold pressure	state	Pa
T_{im}	Intake manifold temperature	state	K
ω_{eng}	Engine speed	state	rpm

3.3.10 Exhaust Gas Temperature

The exhaust temperature model is used to determine the temperature of the combustion gases exiting each cylinder and entering the intake manifold, T_{cylout}. This model is developed originally in [29] and consists of two parts. In the first part, shown in Equations 3.13, temperature and pressure of the combustion products when the exhaust valves open is calculated based on a constant pressure combustion process:

$$X_{\text{eff}} = a_{00} + a_{01}\omega_{\text{eng}} + a_{02}\omega_{\text{eng}}^2 + a_{10}m_{\text{fuel}} + a_{11}m_{\text{fuel}}\omega_{\text{eng}} \tag{3.13a}$$

$$P_{\text{tdc}} = P_{\text{im}}\text{ECR}^{\gamma_{\text{im}}} \tag{3.13b}$$

$$T_{\text{tdc}} = \frac{P_{\text{im}}V_{\text{tdc}}}{m_{\text{charge}}R}\text{ECR}^{\gamma_{\text{im}}} \tag{3.13c}$$

$$V_{\text{eoc}} = \frac{\gamma_{\text{im}} - 1}{\gamma_{\text{im}}}\frac{X_{\text{eff}}m_{\text{fuel}}\text{LHV}_{\text{fuel}}}{P_{\text{tdc}}} + V_{\text{tdc}} \tag{3.13d}$$

$$T_{\text{eoc}} = T_{\text{tdc}}\frac{V_{\text{eoc}}}{V_{\text{tdc}}} \tag{3.13e}$$

$$P_{\text{evo}} = P_{\text{tdc}}\left(\frac{V_{\text{eoc}}}{V_{\text{evo}}}\right)^{\gamma_{\text{ex}}} \tag{3.13f}$$

$$T_{\text{evo}} = P_{\text{tdc}}\left(\frac{V_{\text{eoc}}}{V_{\text{evo}}}\right)^{\gamma_{\text{ex}}-1} \tag{3.13g}$$

In the second part of the model, shown in Equations 3.14, the actual temperature of the gases entering the exhaust manifold is calculated by accounting for heat transfer to the engine block:

$$T_{\text{bd}} = T_{\text{evo}}\left(\frac{P_{\text{em}}}{P_{\text{evo}}}\right)^{1-\frac{1}{\gamma_{\text{ex}}}} \tag{3.14a}$$

$$\begin{aligned} A_1 &= \boldsymbol{\pi}B \cdot S \\ A_2 &= \boldsymbol{\pi}\left(\frac{B}{2}\right)^2 \\ A_3 &= \boldsymbol{\pi}B^2S \end{aligned} \tag{3.14b}$$

$$S_{\text{p}} = 2\frac{\omega_{\text{eng}}}{60} \tag{3.14c}$$

$$w = 6.18 S_{\mathrm{p}} \tag{3.14d}$$

$$h = 3.26 B^{m-1} \left(\frac{P_{\mathrm{em}}}{1000} \right)^{m} T_{\mathrm{bd}}^{0.75-1.62m} w^{m} \tag{3.14e}$$

$$q = h(A_1 + A_2 + A_3)(T_{\mathrm{bd}} - T_{\mathrm{wall}}) \tag{3.14f}$$

$$m_{\mathrm{cylout}} = m_{\mathrm{fuel}} + m_{\mathrm{charge}} \tag{3.14g}$$

$$T_{\mathrm{cylout}} = T_{\mathrm{bd}} - \frac{30q}{\omega_{\mathrm{eng}} c_{\mathrm{p,ex}} m_{\mathrm{cylout}}} \tag{3.14h}$$

The general process efficiency, X_{eff} is calculated as a function of engine speed and fuel mass, and the regression fit constants are listed in Table 3.18. All other parameters used in Equations 3.13 and 3.14 are listed in Table 3.19.

Table 3.18. Regression fit coefficients exhaust gas temperature model

Coefficient	**Value**
a_{00}	0.2415
a_{01}	3.2895×10^{-4}
a_{02}	-7.1204×10^{-8}
a_{10}	2975
a_{11}	-0.8331×10^{-15}

Table 3.19. Parameters in charge flow model

Parameter	Description	Value	Units
P_{im}	Intake manifold pressure	state	Pa
P_{tdc}	Pressure at TDC	Equation 3.13b	Pa
P_{evo}	Pressure at EVO	Equation 3.13f	Pa
P_{em}	Exhaust Manifold Pressure	state	Pa
T_{tdc}	Temperature at TDC	Equation 3.13c	K
T_{eoc}	Temperature at EOC	Equation 3.13e	K
T_{evo}	Temperature at EVO	Equation 3.13g	K
T_{wall}	Cylinder wall temperature	550	K
T_{bd}	Blowdown temperature	Equation 3.14a	K
V_{tdc}	Volume of 1 cylinder at TDC	7.5423×10^{-5}	m^3
V_{eoc}	Volume of 1 cylinder at EOC	Equation 3.13d	m^3
V_{evo}	Volume of 1 cylinder at EVO	6.4107×10^{-4}	m^3
ECR	Effective compression ratio	16	-
m_{charge}	Mass of gas in 1 cylinder	$f(W_{\text{cyl}}, \omega_{\text{eng}})$	kg
m_{fuel}	Fuel mass injected into 1 cylinder in 1 cycle	command	kg
m_{cylout}	Total mass exiting 1 cylinder	Equation 3.14g	kg
R	Gas constant	287	J/kg·K
γ_{im}	Intake manifold specific heat ratio	1.4	-
γ_{ex}	Exhaust manifold specific heat ratio	1.35	-
X_{eff}	Efficiency	Equation 3.13a	-
LHV_{fuel}	Lower heating value of diesel	42.8×10^{6}	J/kg
A_1, A_2, A_3	Sidewall, cylinder head, & piston head area	Equation 3.14b	m^2
B	Cylinder bore diameter	0.1065	m
S	Cylinder stroke length	0.127	m
S_{p}	Mean piston speed	Equation 3.14c	m/s
ω_{eng}	Engine speed	state	rpm
w	Average cylinder gas velocity	Equation 3.14d	m/s
m	Convective heat transfer parameter	0.8	-
h	Convective heat transfer coefficient	Equation 3.14e	$\text{W/m}^2\text{·K}$
q	Mass specific heat transfer	Equation 3.14f	W/kg
$c_{\text{p,ex}}$	Constant pressure specific heat	1107	J/kg·K

3.3.11 eBooster Outlet Temperature

The eBooster compression stage is assumed to be an isentropic process, so the isentropic temperature relation is used to calculate its outlet temperature:

$$T_{\text{eboost,out}} = T_{\text{cac}} \left(\frac{P_{\text{im}}}{P_{\text{compis}}} \right)^{\frac{\gamma_{\text{amb}}-1}{\gamma_{\text{amb}}}} \tag{3.15}$$

T_{cac} is the CAC outlet temperature, which is approximately constant at 307 K, P_{im} is the intake manifold pressure state, P_{compis} is the compressor interstage pressure state, and γ_{amb} is the ratio of specific heats for air, which is 1.4.

3.3.12 Engine Torque Coefficient

A torque balance about the engine crankshaft between load torque and torque applied by combustion models the engine's crank speed in Equation 3.2j. The combustion torque itself is modeled as the product of intake manifold pressure, P_{im}, and the torque coefficient in Equations 3.16:

$$C_{\text{trq}} = \frac{\eta_{\text{vol}} \eta_{\text{therm}} \text{LHV}_{\text{fuel}} V_{\text{disp}} N_{\text{cyl}}}{4\pi R T_{\text{im}} \text{AFR}} \tag{3.16a}$$

$$\begin{aligned} \eta_{\text{therm}} = a_{00} + a_{01}\omega_{\text{eng}} + a_{02}\omega_{\text{eng}}^2 + a_{03}\omega_{\text{eng}}^3 + a_{10}\tau_{\text{eng}} + a_{11}\tau_{\text{eng}}\omega_{\text{eng}} + \\ a_{12}\tau_{\text{eng}}\omega_{\text{eng}}^2 + a_{20}\tau_{\text{eng}}^2 + a_{21}\tau_{\text{eng}}^2\omega_{\text{eng}} + a_{30}\tau_{\text{eng}}^3 \end{aligned} \tag{3.16b}$$

The AFR in this case is the ratio of total charge flow, including EGR gases, to fuel, and the thermal efficiency, η_{therm} of the engine is modeled as a polynomial fit to engine speed, ω_{eng}, and external load torque, τ_{eng}. All parameters in Equation 3.16 are listed in Table 3.20, and the coefficients used in the regression fit are listed in Table 3.21.

Table 3.20. Parameters engine torque coefficient model

Parameter	Description	Value	Units
N_{cyl}	Number of cylinders	4	-
η_{vol}	Volumetric efficiency	0.91	-
η_{therm}	Engine thermal efficiency	Equation 3.16b	-
V_{disp}	Displacement of single cylinder	1.131×10^{-3}	m^3
R	Gas constant	287	J/kg·K
LHV_{fuel}	Lower heating value of diesel	42.8×10^{6}	J/kg
T_{im}	Intake manifold temperature	state	K
AFR	Air-fuel ratio	$W_{\text{cyl}}/W_{\text{fuel}}$	-
ω_{eng}	Engine speed	state	rpm
τ_{eng}	External load torque	disturb. input	Nm

Table 3.21. Regression fit coefficients for thermal efficiency

Coefficient	Value
a_{00}	0.7587
a_{01}	-7.687×10^{-4}
a_{02}	3.825×10^{-7}
a_{03}	-7.500×10^{-11}
a_{10}	4.355×10^{-4}
a_{11}	9.083×10^{-7}
a_{12}	-1.000×10^{-10}
a_{20}	-3.039×10^{-6}
a_{21}	7.571×10^{-10}
a_{30}	3.688×10^{-9}

4. STATE SPACE MODEL LINEARIZATION, VALIDATION, AND ANALYSIS

4.1 Nonlinear Model Linearization

To develop the set of linear $\mathcal{H}_\infty$ controllers discussed in Section 1.3.4, linear engine models are required, which can be obtained by linearizing the nonlinear state space model presented in Chapter 3. Each resulting linear model can be represented as:

$$\dot{x} = \delta\dot{x} = A\delta x + B\delta u + F\delta u_\mathrm{d} \tag{4.1a}$$

$$\delta y = C\delta x + D\delta u \tag{4.1b}$$

$$\delta x = x - x_\mathrm{e} \qquad \delta y = y - y_\mathrm{e} \qquad \delta u = u - u_\mathrm{e} \qquad \delta u_\mathrm{d} = u_\mathrm{d} - u_\mathrm{d,e} \tag{4.1c}$$

where x, y, u, and u_d are the nonlinear model states, outputs, and inputs, δx, δy, δu, and δu_d are their linear correlaries, and x_e, y_e, u_e, and $u_\mathrm{d,e}$ are the equilibrium values around which the nonlinear model is linearized. The state matrices, A, B, F, C, and D are calculated from the set of nonlinear differential equations,

$$\dot{x} = f(x, u, u_\mathrm{d}) \tag{3.1a}$$

$$y = g(x, u) \tag{3.1b}$$

as the following Jacobian matrices, where each partial derivative is calculated as a function of x_{e}, u_{e}, and $u_{\mathrm{d,e}}$:

$$A = A^{10\times10}(x_{\mathrm{e}}, u_{\mathrm{e}}, u_{\mathrm{d,e}}) = \begin{bmatrix} \frac{\partial f_1}{\partial x_1} & \cdots & \frac{\partial f_1}{\partial x_{10}} \\ \vdots & \ddots & \vdots \\ \frac{\partial f_{10}}{\partial x_1} & \cdots & \frac{\partial f_{10}}{\partial x_{10}} \end{bmatrix} \tag{4.3a}$$

$$B = B^{10\times5}(x_{\mathrm{e}}, u_{\mathrm{e}}, u_{\mathrm{d,e}}) = \begin{bmatrix} \frac{\partial f_1}{\partial u_1} & \cdots & \frac{\partial f_1}{\partial u_5} \\ \vdots & \ddots & \vdots \\ \frac{\partial f_{10}}{\partial u_1} & \cdots & \frac{\partial f_{10}}{\partial u_5} \end{bmatrix} \tag{4.3b}$$

$$F = F^{10\times1}(x_{\mathrm{e}}, u_{\mathrm{e}}, u_{\mathrm{d,e}}) = \begin{bmatrix} \frac{\partial f_1}{\partial u_{\mathrm{d}}} \\ \vdots \\ \frac{\partial f_{10}}{\partial u_{\mathrm{d}}} \end{bmatrix} \tag{4.3c}$$

$$C = C^{3\times10}(x_{\mathrm{e}}, u_{\mathrm{e}}, u_{\mathrm{d,e}}) = \begin{bmatrix} \frac{\partial g_1}{\partial x_1} & \cdots & \frac{\partial g_1}{\partial x_{10}} \\ \vdots & \ddots & \vdots \\ \frac{\partial g_3}{\partial x_1} & \cdots & \frac{\partial g_3}{\partial x_{10}} \end{bmatrix} \tag{4.3d}$$

$$D = D^{3\times5}(x_{\mathrm{e}}, u_{\mathrm{e}}, u_{\mathrm{d,e}}) = \begin{bmatrix} \frac{\partial g_1}{\partial u_1} & \cdots & \frac{\partial g_1}{\partial u_5} \\ \vdots & \ddots & \vdots \\ \frac{\partial g_3}{\partial u_1} & \cdots & \frac{\partial g_3}{\partial u_5} \end{bmatrix} \tag{4.3e}$$

In practice, the nonlinear state equations are linearized using MATLAB's symbolic toolbox, then each linear model is generated by passing the equilibrium states and inputs as arguments for the symbolic linear matrices.

4.2 Linear Models Selected

The engine operating space of interest for control ranges from 1200 rpm to 2000 rpm, and no single linear model accurately represents the engine dynamics across this entire speed range. Instead, two linear models are used which each cover a 400 rpm range around their respective equilibria, thus covering the complete operating range of interest. The equilibrium states and input conditions for these linear models are listed in Table 4.1.

Table 4.1. Equilibrium states and inputs for linear models

State / Input	Parameter	Linear Model 1 Equilibrium Value (1200 - 1600 rpm)	Linear Model 2 Equilibrium Value (1600 - 2000 rpm)	Units
x_1	P_{compis}	163.96	174.97	kPa
x_2	P_{im}	191.13	202.04	kPa
x_3	P_{em}	200.28	219.84	kPa
x_4	P_{etin}	109.29	111.10	kPa
x_5	T_{im}	323	326	K
x_6	T_{em}	629	636	K
x_7	T_{etin}	629	636	K
x_8	ω_{tc}	93	102	krpm
x_9	ω_{eboost}	45	45	krpm
x_{10}	ω_{eng}	1400	1800	rpm
u_1	A_{egr}	2.26 (50% of max)	2.26 (50% of max)	cm^2
u_2	A_{et}	12.53 (50% of max)	12.53 (50% of max)	cm^2
u_3	$\omega_{\text{eboostCMD}}$	45 (64% of max)	45 (64% of max)	krpm
u_4	A_{bv}	0 (0% of max)	0 (0% of max)	cm^2
u_5	W_{fuel}	2.52	3.29	g/s
u_{d}	τ_{eng}	300	300	Nm

4.3 Model Validation

The linearized engine models are validated against a high fidelity truth reference GT Power engine model to ensure that they accurately represent the physical engine's gas exchange dynamics, and to obtain the uncertainty bounds used in $\mathcal{H}_\infty$ controller design. This GT Power engine model from John Deere simulates crank angle resolved combustion dynamics and one dimensional flow, so for model validation, it is a reasonable proxy for the real engine.

An open loop validation approach, shown in 4.1, is used for validation of both the nonlinear and linear models, wherein an existing set of controllers passes inputs to both GT Power and the state space models. For this validation, a target engine speed and disturbance load torque profile is simulated in GT Power, using its internal controllers to determine the input signals to the five actuators, then the same load torque profile is then simulated with the linear and nonlinear models using the actuator signals generated in GT-Power. Finally, the

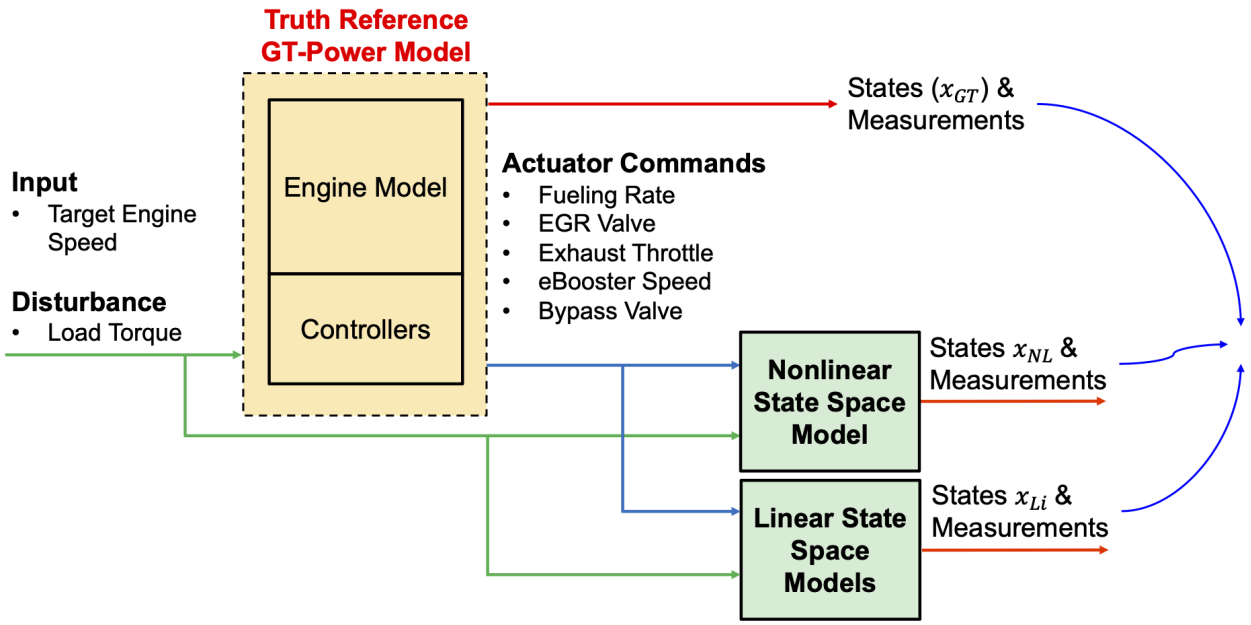

Figure 4.1. Nonlinear and linear model validation method

vectors of states, x, and state outputs, y, for the linear and nonlinear models are compared to the equivalent GT Power parameters for accuracy. The speed-torque profiles used for validation are constant speed torque steps from 100 Nm to 500 Nm in 100 Nm increments. This set of torque steps is conducted at 1200 rpm, 1400 rpm, 1800 rpm, 1800 rpm, and 2000rpm, covering the entire engine speed range of interest.

The manufacturer eBooster map does not contain data for low eBooster speeds or pressure ratios near 1, and as a result, the nonlinear model does not capture the gas exchange dynamics at these low eBooster speeds and pressure ratios. Consequently, for this validation, the eBooster is maintained at a 30,000 rpm idle speed, because this is the minimum speed for which the nonlinear model is tuned and comparison is reasonable.

Additionally, the exhaust throttle and bypass valve areas do not change in these validation results. On the actual engine, the exhaust throttle is set at a fixed position and not controlled, and the bypass valve is dependent on eBooster speed and remains shut above 30,000 rpm, so the same conditions are represented here.

4.3.1 Validation Results from Linear Model 1

The first linear model is linearized about an engine speed of 1400 rpm, and validation results are shown at 1200 rpm, 1400 rpm, and 1600 rpm.

Torque Steps at 1200 rpm

At the 1200 rpm operating point, the existing GT Power controllers command the EGR valve to remain mostly shut at low torque, then open slightly more with each increase in torque until the valve is completely open at high torque. The eBooster remains at 30,000 rpm until torque reaches 400 Nm, when speed is increased slightly to around 35,000 rpm.

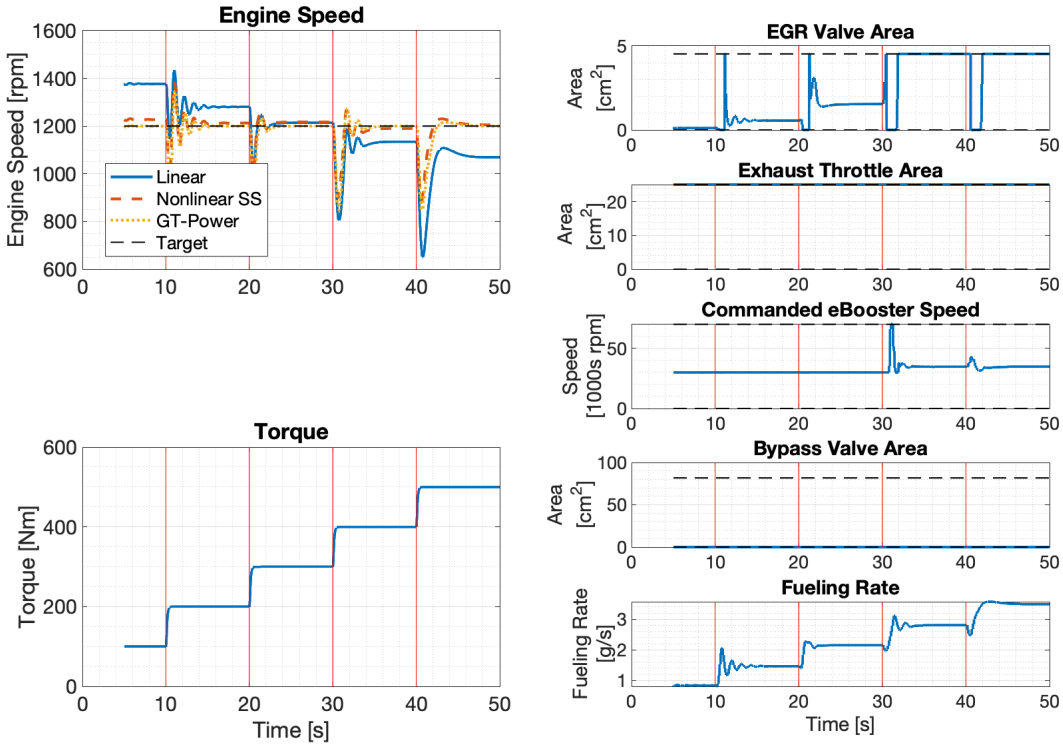

Figure 4.2. Linear model 1 speed and torque profile and actuator responses for torque steps at 1200 rpm

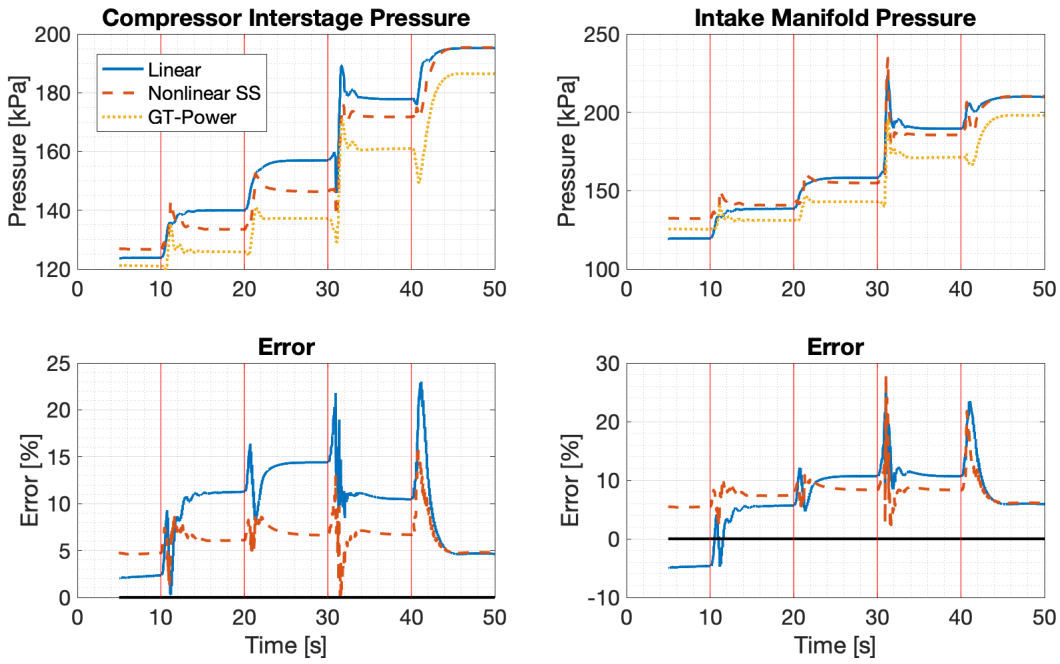

(a) Compressor interstage pressure and intake manifold pressure

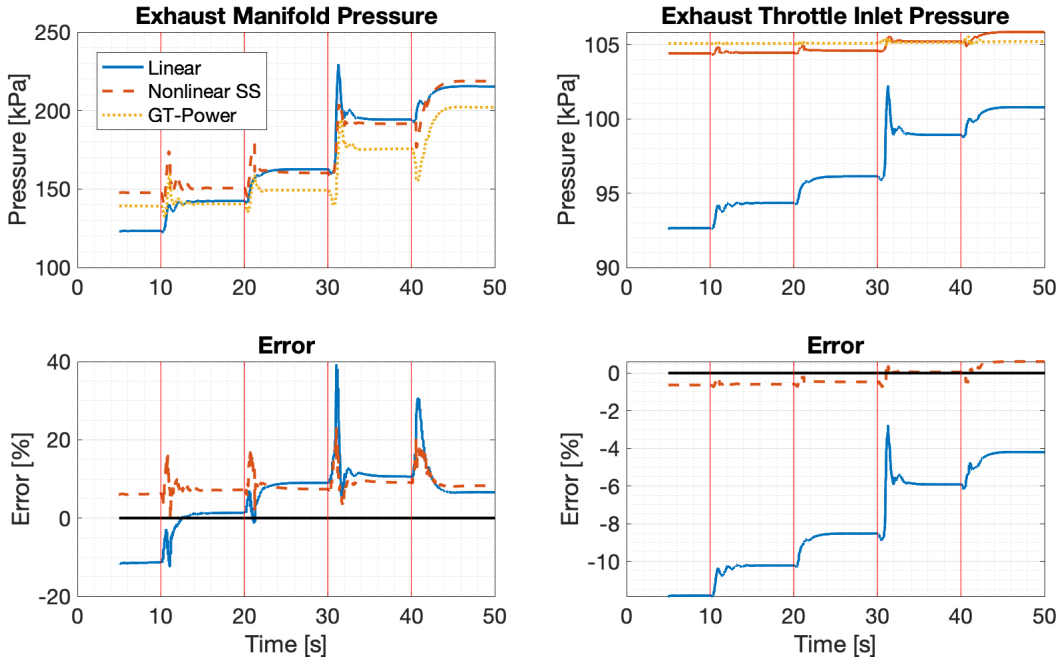

(b) Exhaust manifold and exhaust throttle inlet pressure

Figure 4.3. Linear model 1 pressure states for torque steps at 1200 rpm

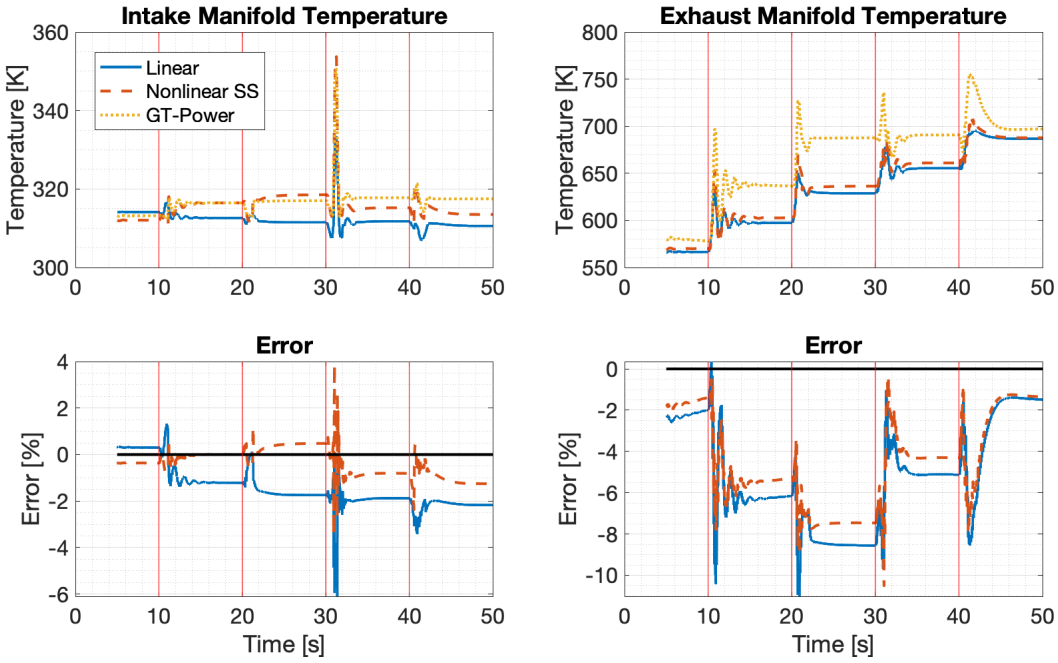

(a) Intake and exhaust manifold

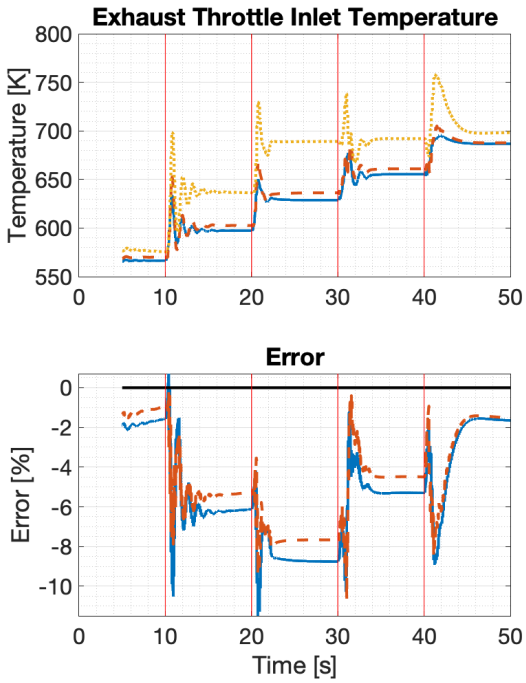

(b) Exhaust throttle inlet

Figure 4.4. Linear model 1 temperature states for torque steps at 1200 rpm

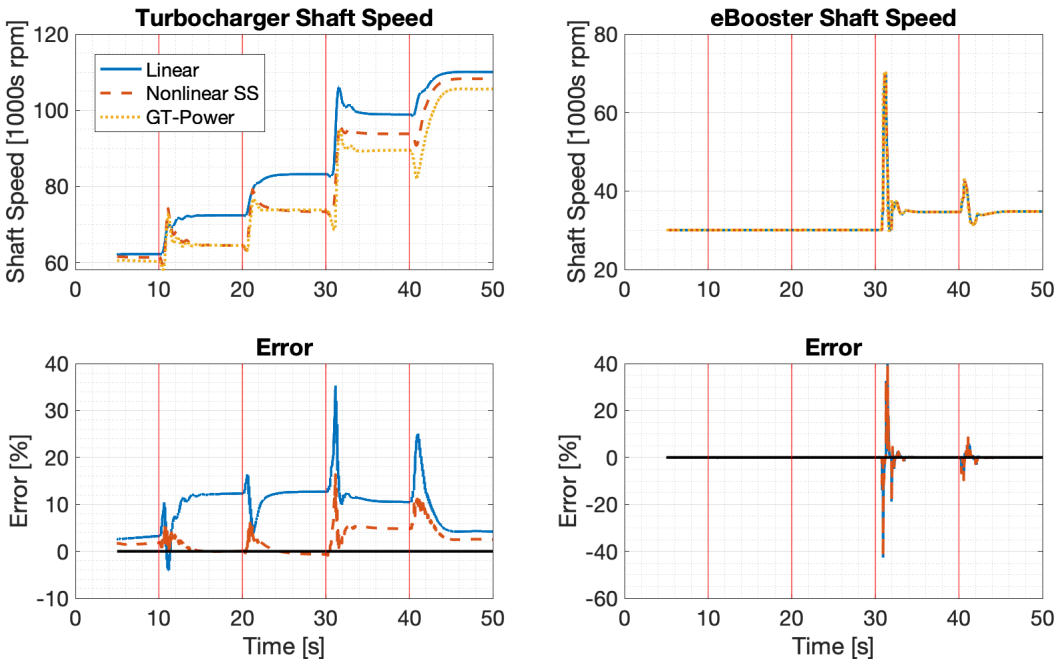

Figure 4.5. Linear model 1 turbomachinery speed states for torque steps at 1200 rpm

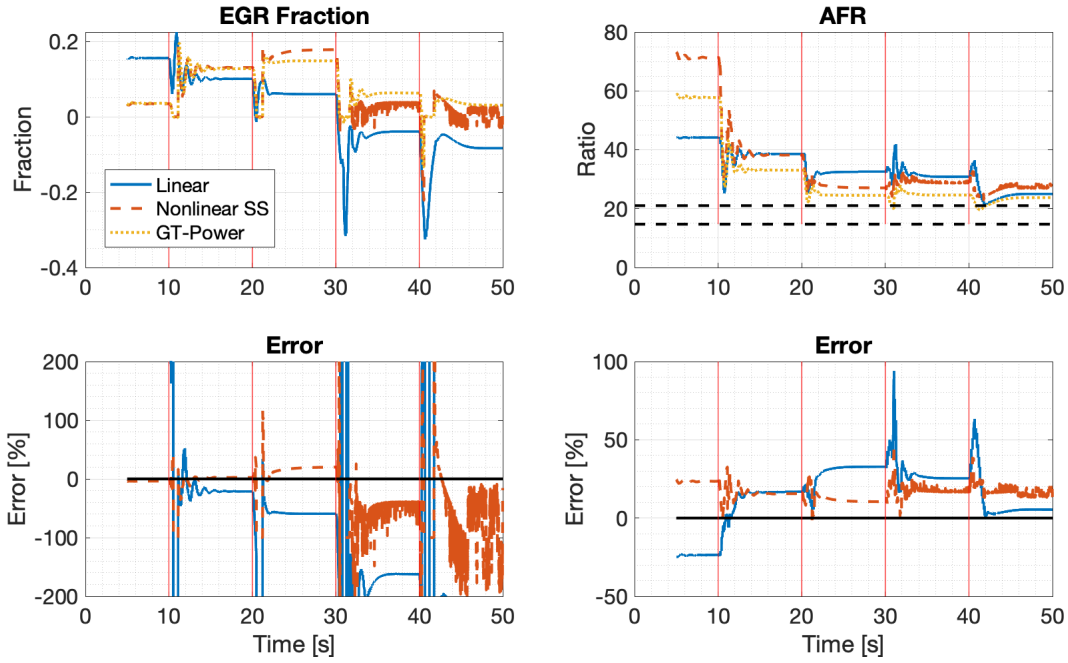

(a) EGR fraction and AFR

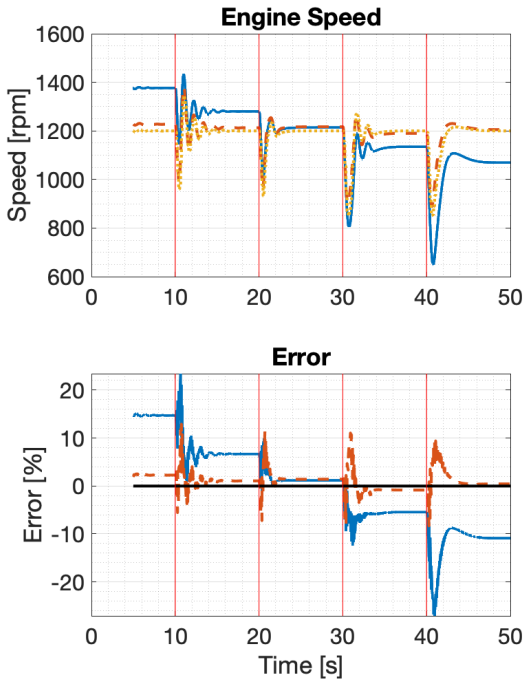

(b) Engine speed

Figure 4.6. Linear model 1 state outputs for torque steps at 1200 rpm

Under steady state conditions, all linear model states remain within 15% of the GT Power truth reference, and all nonlinear model states remain within 10%. However, brief transient errors as high as 40% and 30% are observed for the linear and nonlinear models respectively, which result primarily from sudden changes in eBooster operation. The eBooster can accelerate from its 2000 rpm idle speed to its 70,000 rpm maximum speed within 0.3 seconds, but the eBooster outlet pressure (intake manifold pressure) in the GT Power model does not increase as quickly in response to this sudden speed increase as the nonlinear and linear models predict. This is likely because the GT Power model uses a detailed, proprietary black box eBooster model, whereas the map data available for the state space model does not include the high speed, low pressure ratio operating area for the eBooster. As a result, the eBooster model derived from the available map data likely overestimates air flow in this regime. Additionally, in the reference engine model, transient pressure spikes are smaller and much less abrupt, indicating that gas flows in the state space models respond much faster that they do in the reference model.

State output responses at this low engine speed also show significant error. Engine speed tracking is good–within 2% and 10% for the nonlinear model under steady state and transience and within 15% and 25% for the linear model under steady state and transience. However the linear model's EGR fraction error appears to be large, especially at low torque condition of the first few seconds, simply because EGR fraction close to zero. In this region, the pressure difference across the EGR valve is small–on the order of 20 kPa–so the EGR flow is sensitive to small errors in intake and exhaust manifold pressure, leading to larger errors overall. AFR is represented reasonably well, although significant transient errors are observed, again due to the discrepencies in eBooster flow already noted.

Finally, the linear model predicts significantly lower exhaust throttle inlet pressures than the nonlinear model suggests. This is because the valve flow model variation with pressure ratio is highly nonlinear at low pressure ratios like those observed across the exhaust throttle. Consequently, any given linear model is only accurate for a narrow range of pressure ratios and exhaust throttle effective areas near the linearization condition, leading to large errors when conditions are far from the equilibrium used for linearization.

Torque Steps at 1400 rpm

At the 1400 rpm operating point, the existing GT Power controllers again command the EGR valve to remain mostly shut at low torque, then open slightly more with each increase in torque until the valve is completely open at high torque. The eBooster also remains at 30,000 rpm until torque reaches 400 Nm, when speed is increased slightly to around 35,000 rpm.

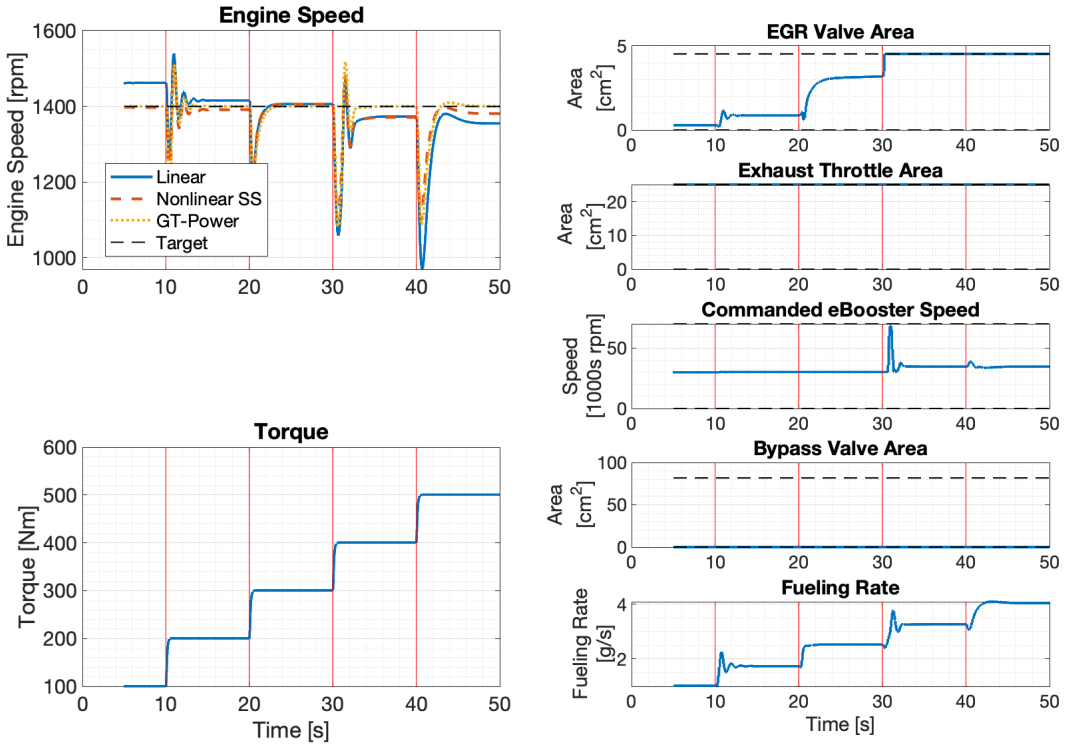

Figure 4.7. Linear model 1 speed and torque profile and actuator responses for torque steps at 1400 rpm

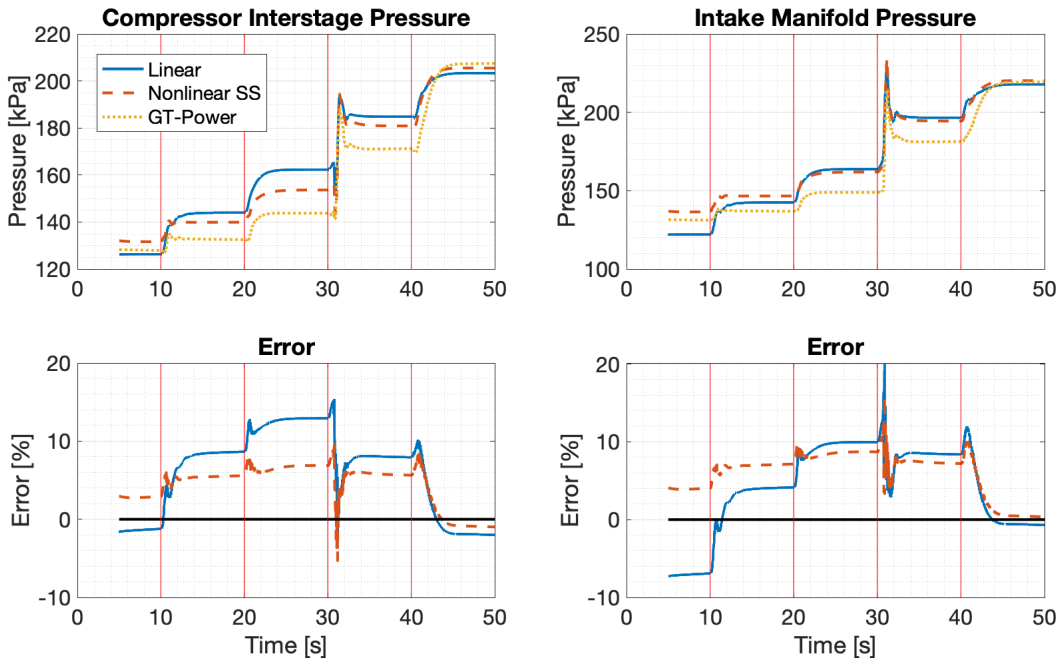

(a) Compressor interstage pressure and intake manifold pressure

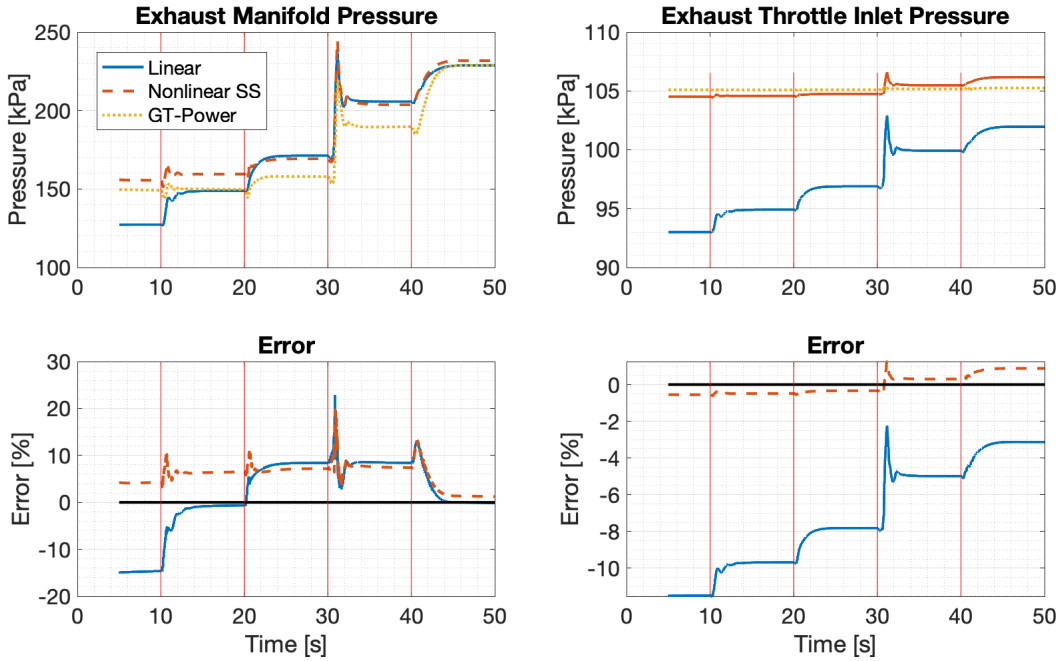

(b) Exhaust manifold and exhaust throttle inlet pressure

Figure 4.8. Linear model 1 pressure states for torque steps at 1400 rpm

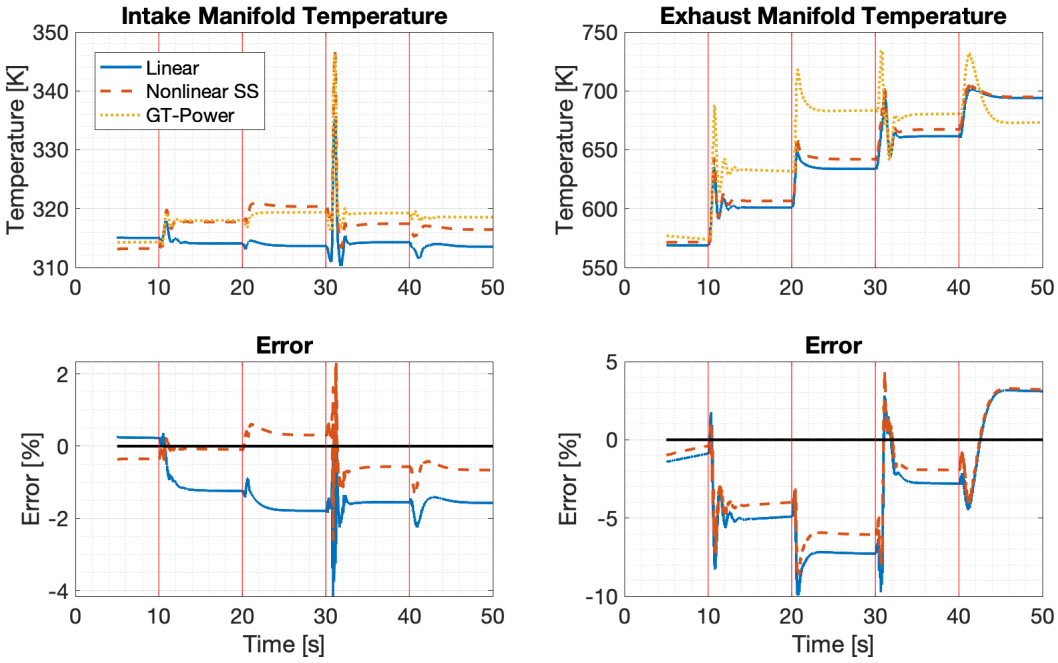

(a) Intake and exhaust manifold

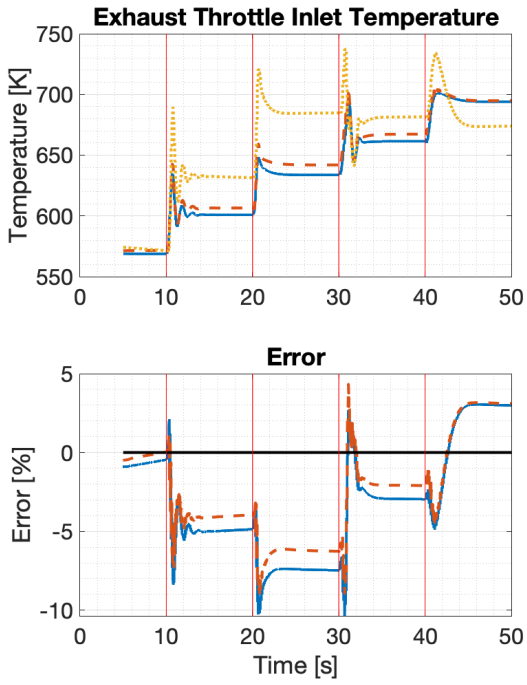

(b) Exhaust throttle inlet

Figure 4.9. Linear model 1 temperature states for torque steps at 1400 rpm

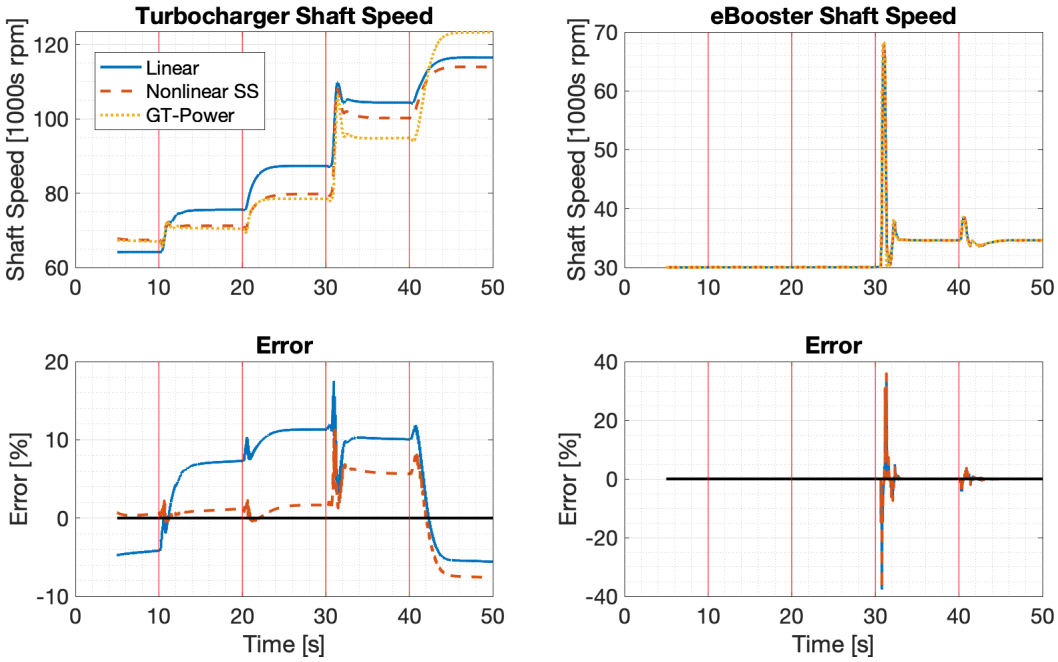

Figure 4.10. Linear model 1 turbomachinery speed states for torque steps at 1400 rpm

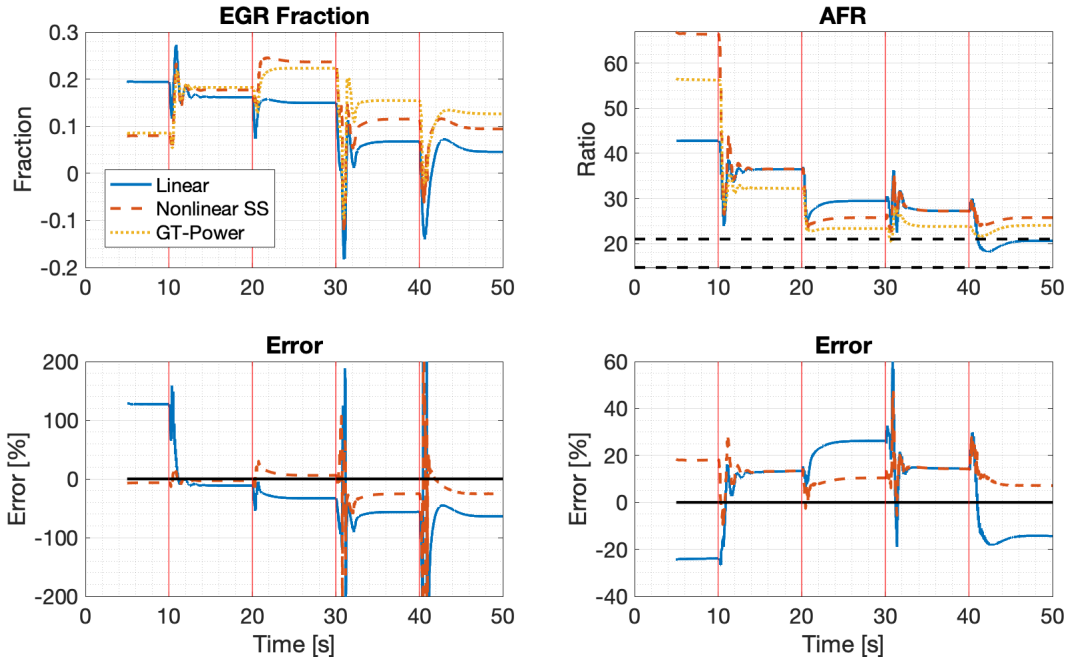

(a) EGR fraction and AFR

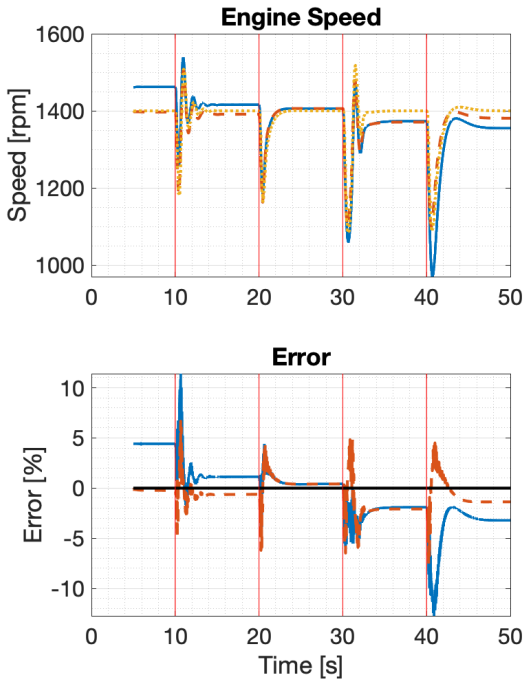

(b) Engine speed

Figure 4.11. Linear model 1 state outputs for torque steps at 1400 rpm

Model results at 1400 rpm are somewhat better overall than the 1200 rpm case, because the engine is operating closer to the equilibrium states used for linearization. Additionally, EGR fraction and AFR tracking are better because the EGR fraction is not as close to 0 overall. However, the linear model still shows significant error at 100Nm in both EGR fraction and AFR, indicating that the linear model does not accurately represent fresh air and EGR flow rates at low torque. Additionally, the linear model still significantly underestimates exhaust throttle inlet pressure.

Torque Steps at 1600 rpm

At the 1600 rpm operating point, the existing GT Power controllers command roughly the same EGR valve and eBooster speeds as the 1200 rpm and 1600 rpm operating points, although fueling rate is slightly greater because of the higher engine speed.

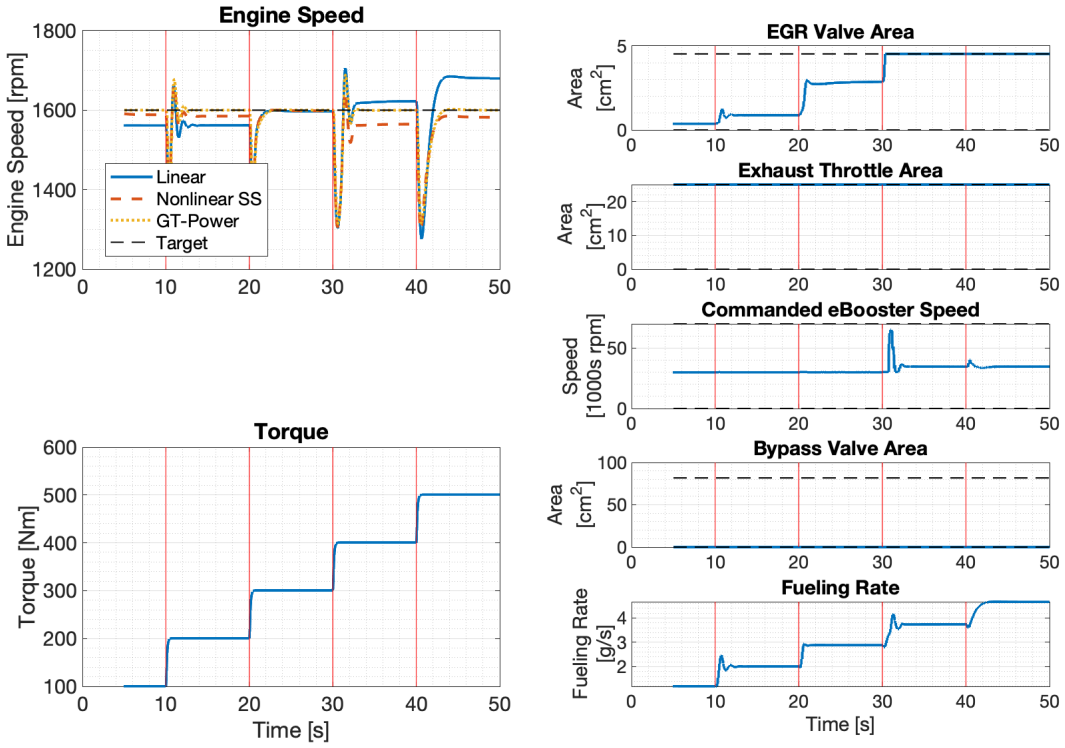

Figure 4.12. Linear model 1 speed and torque profile and actuator responses for torque steps at 1600 rpm

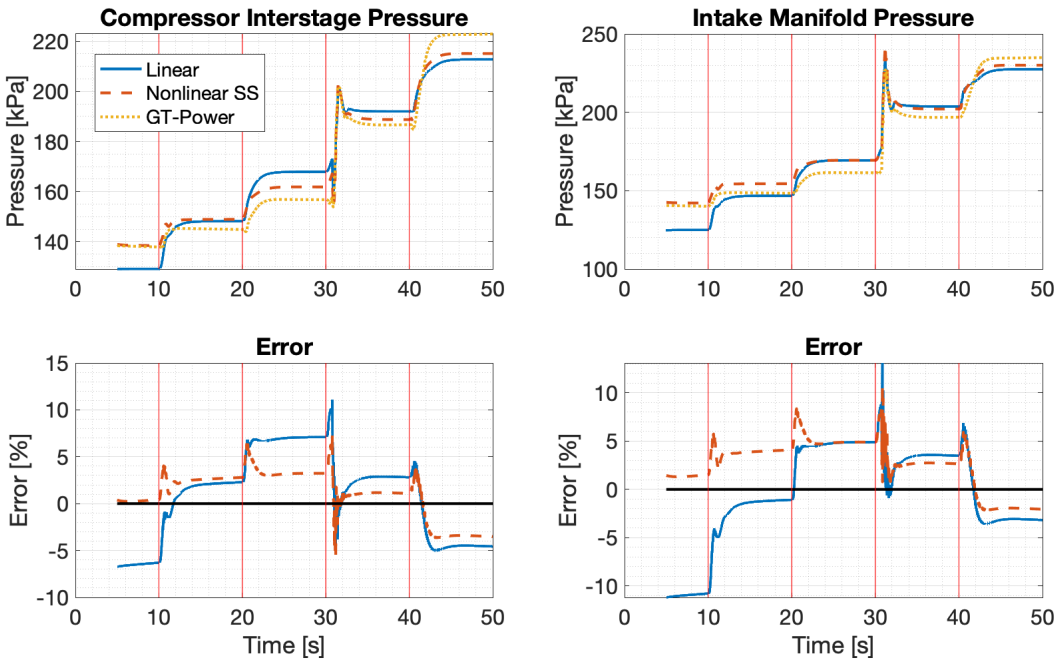

(a) Compressor interstage pressure and intake manifold pressure

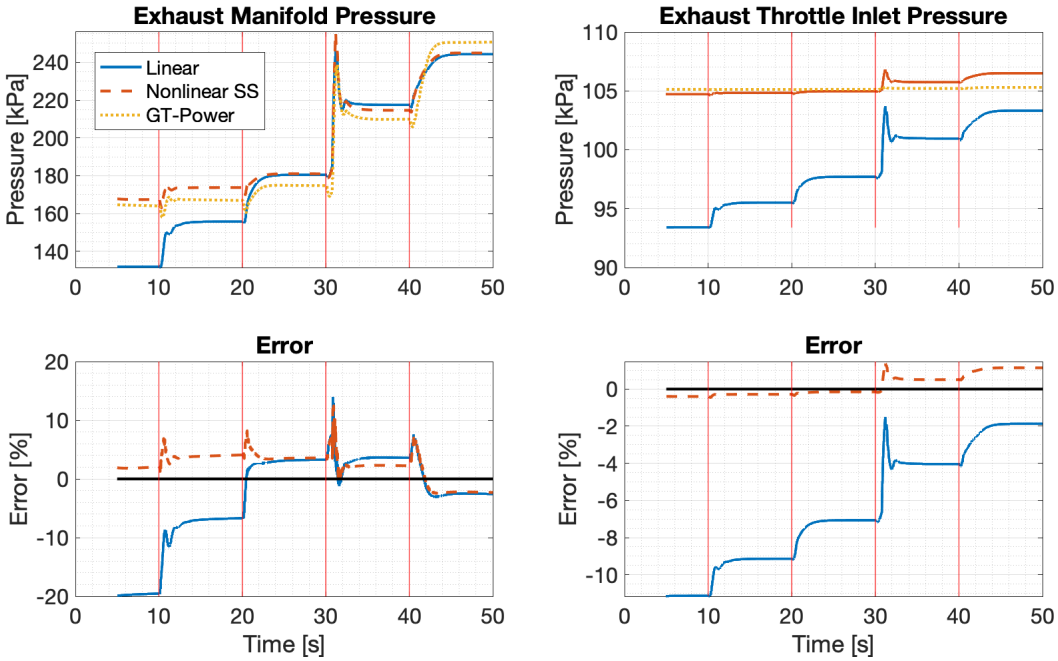

(b) Exhaust manifold and exhaust throttle inlet pressure

Figure 4.13. Linear model 1 pressure states for torque steps at 1600 rpm

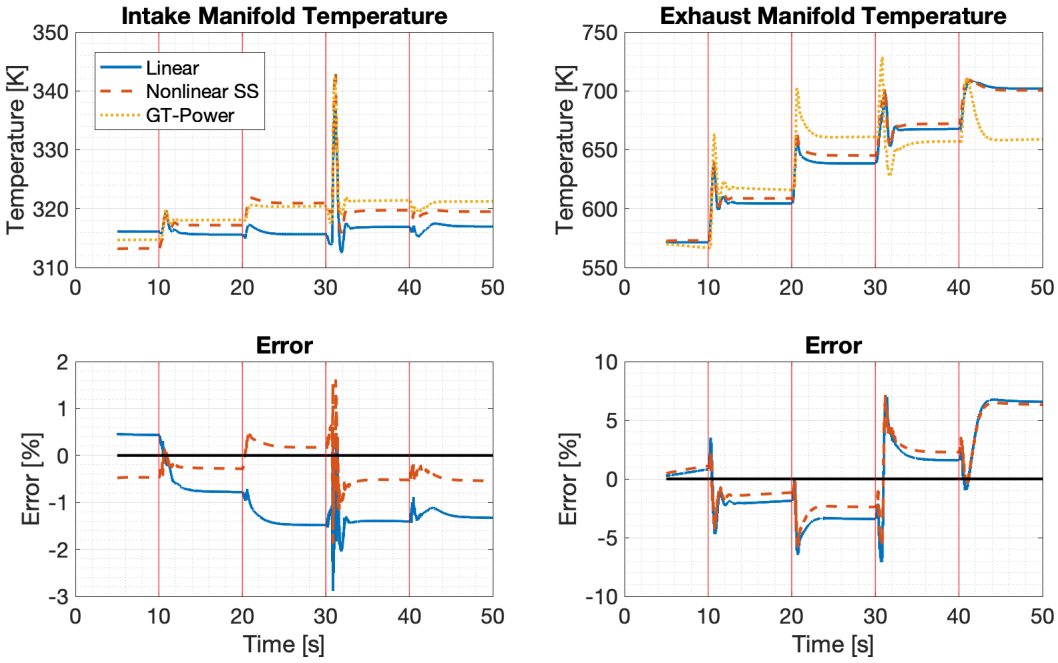

(a) Intake and exhaust manifold

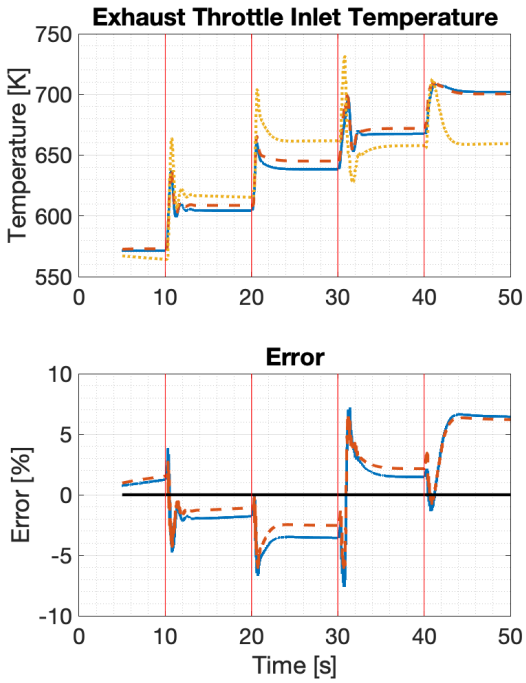

(b) Exhaust throttle inlet

Figure 4.14. Linear model 1 temperature states for torque steps at 1600 rpm

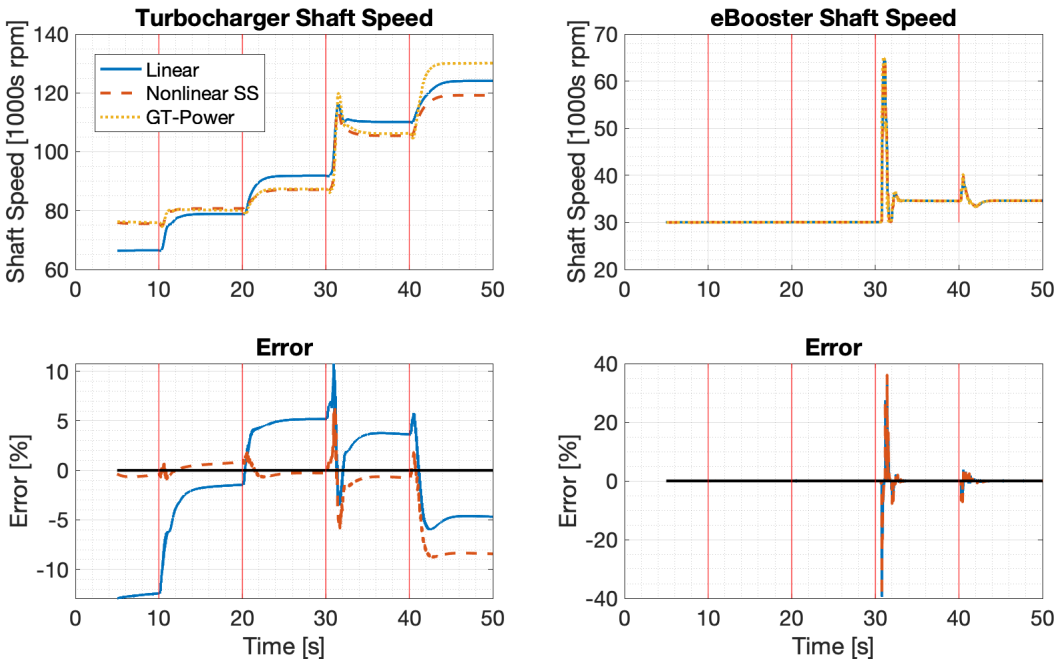

Figure 4.15. Linear model 1 turbomachinery speed states for torque steps at 1600 rpm

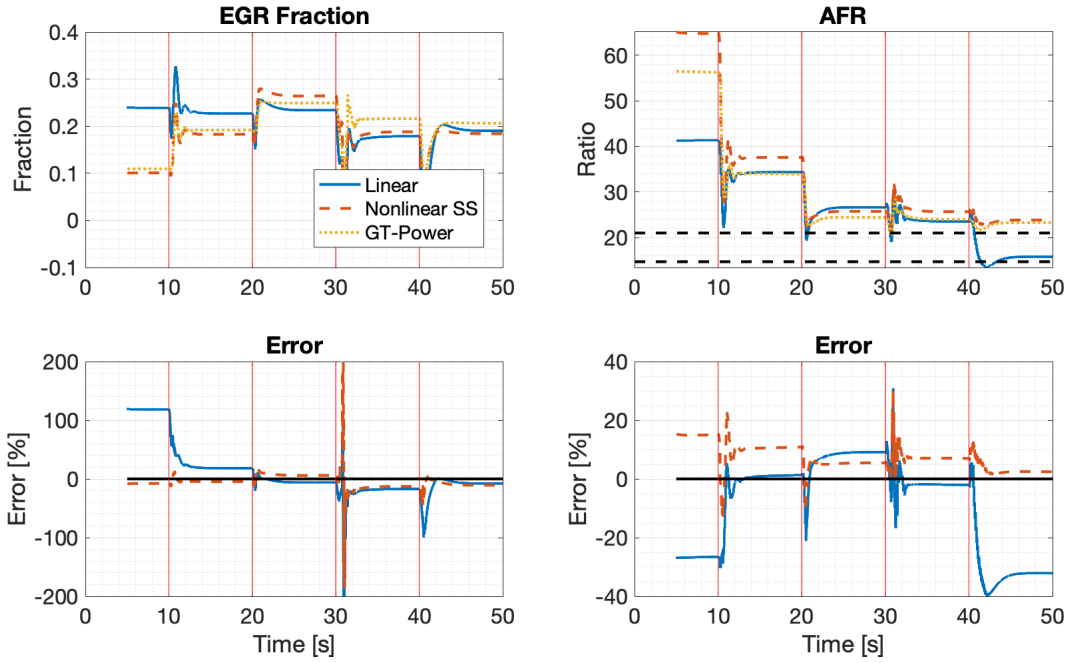

(a) EGR fraction and AFR

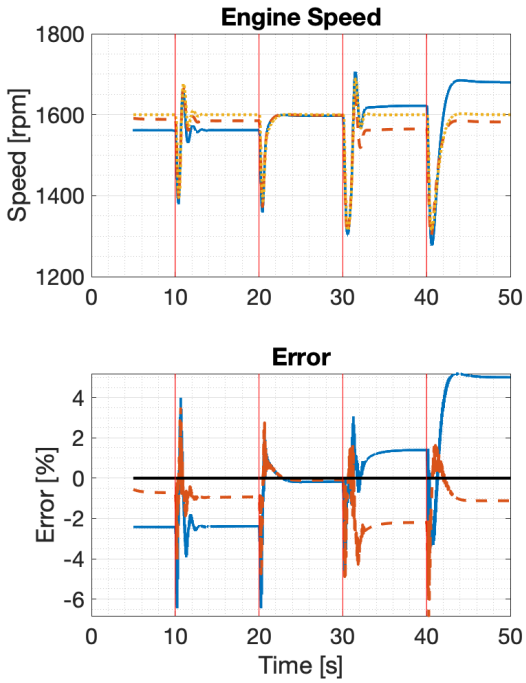

(b) Engine speed

Figure 4.16. Linear model 1 state outputs for torque steps at 1600 rpm

Improved responses across all states and state outputs are again observed, because the higher engine speed maintains flow rates that are consistantly in a range that the linear model can well represent. However, large errors in EGR fraction and AFR are still observed at low torque due to state conditions that are far away from the linearization equilibrium.

4.3.2 Validation Results from Linear Model 2

The second linear model is linearized about an engine speed of 1800 rpm, and validation results are shown at 1600 rpm, 1800 rpm, and 2000 rpm.

Torque Steps at 1600 rpm

The 1600 rpm speed-torque profile and actuator commands used to validate linear model 1 are used here to validate linear model 2 at 1600 rpm. This engine speed also represents the crossover point between the models. Below 1600 rpm, linear model 1 is used, and above 1600 rpm, linear model 2 is used.

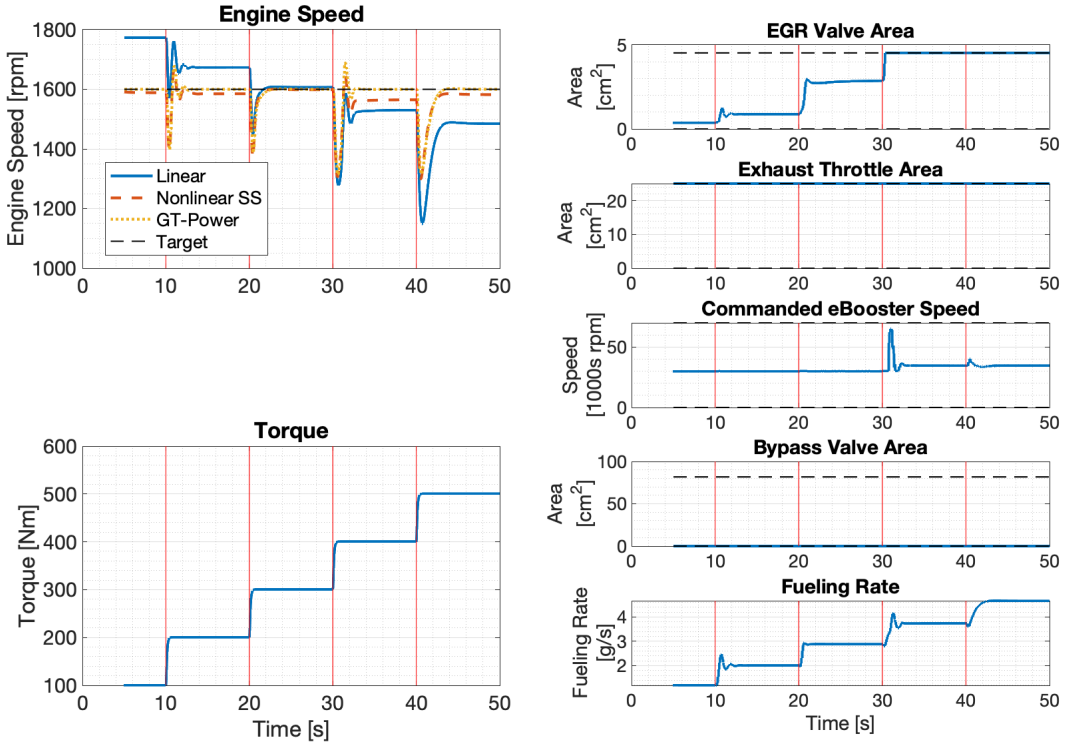

Figure 4.17. Linear model 2 speed and torque profile and actuator responses for torque steps at 1600 rpm

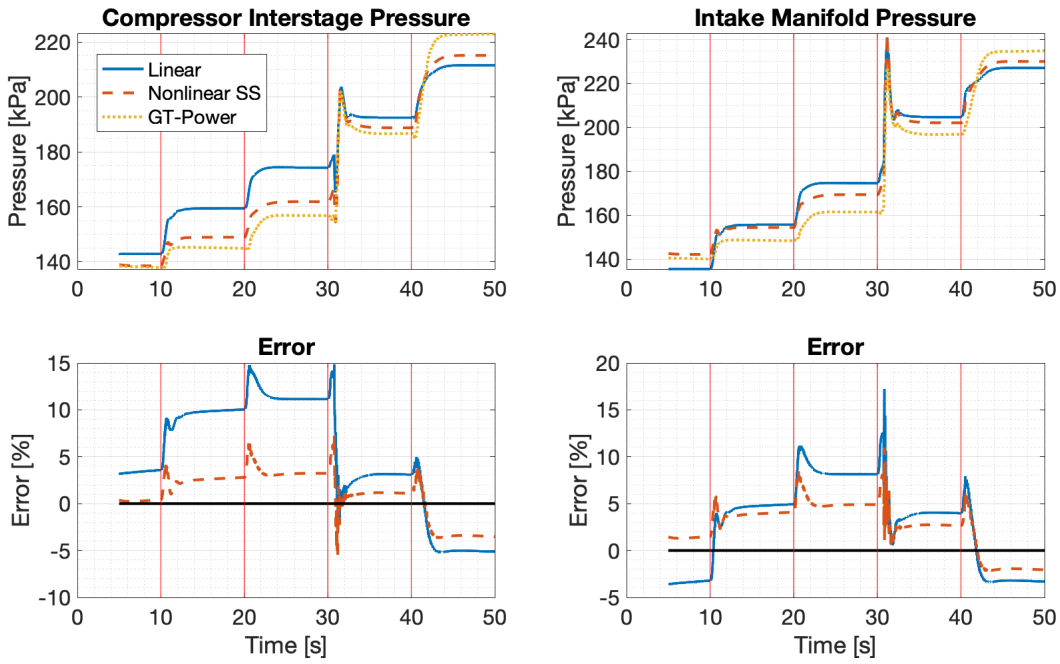

(a) Compressor interstage pressure and intake manifold pressure

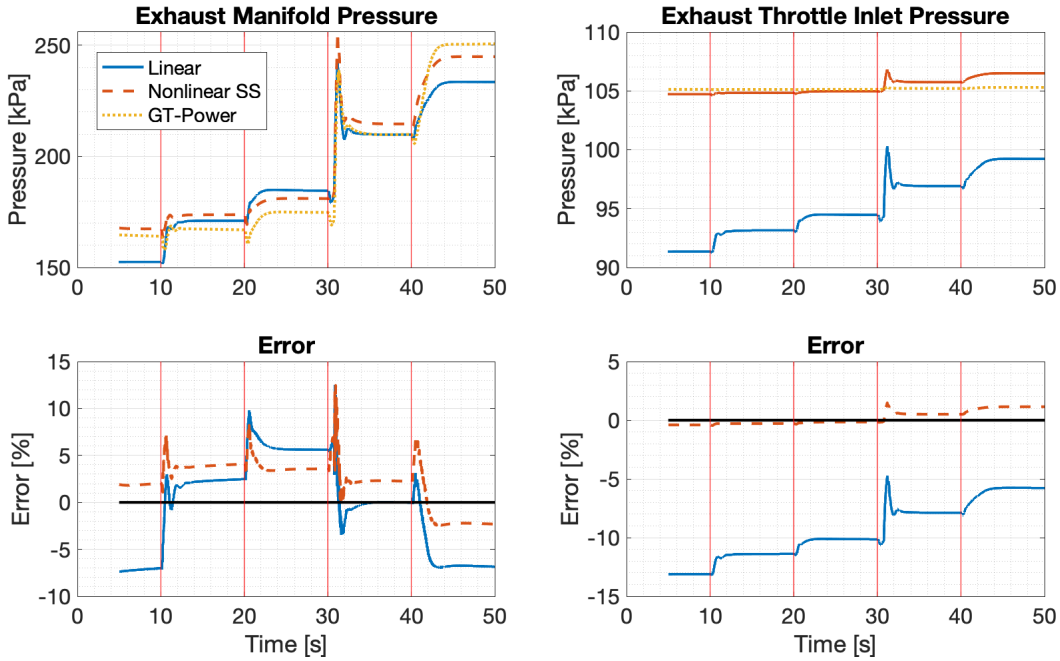

(b) Exhaust manifold and exhaust throttle inlet pressure

Figure 4.18. Linear model 2 pressure states for torque steps at 1600 rpm

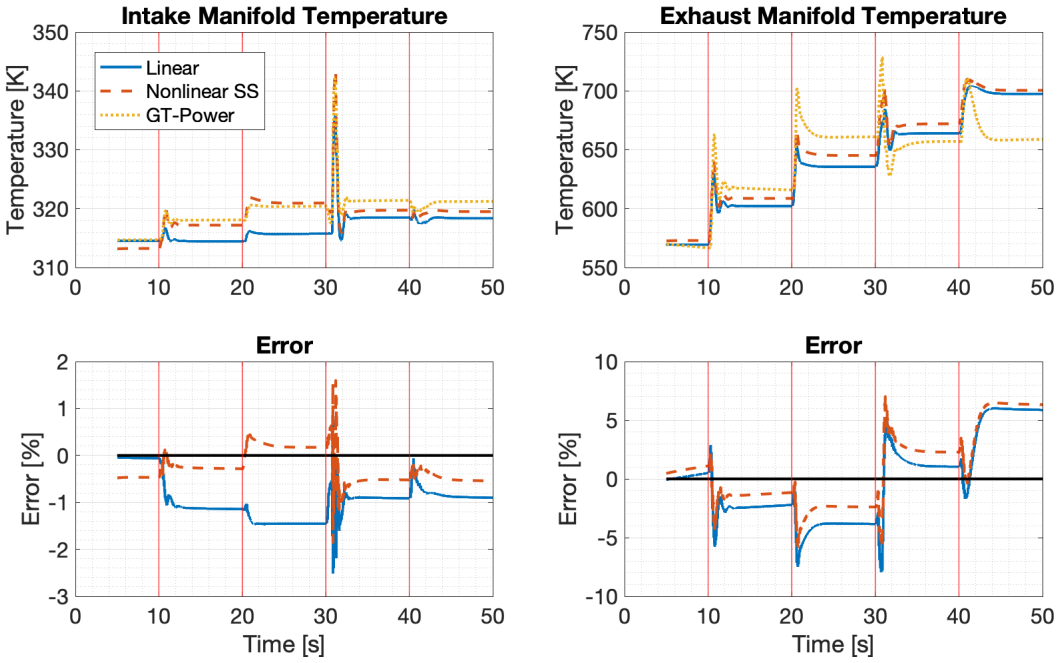

(a) Intake and exhaust manifold

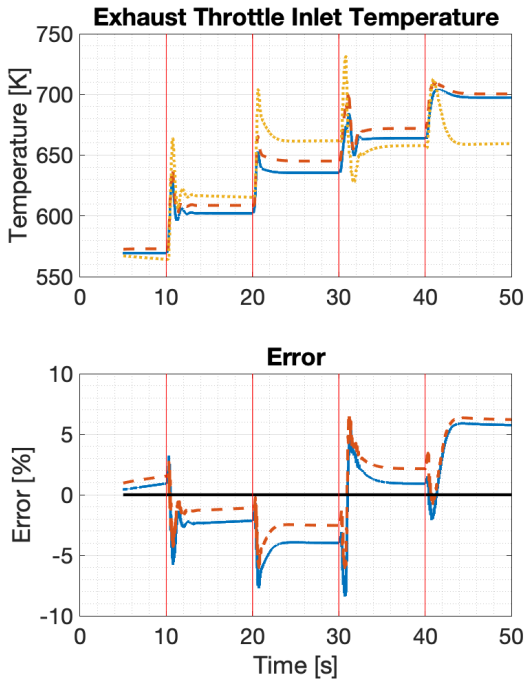

(b) Exhaust throttle inlet

Figure 4.19. Linear model 2 temperature states for torque steps at 1600 rpm

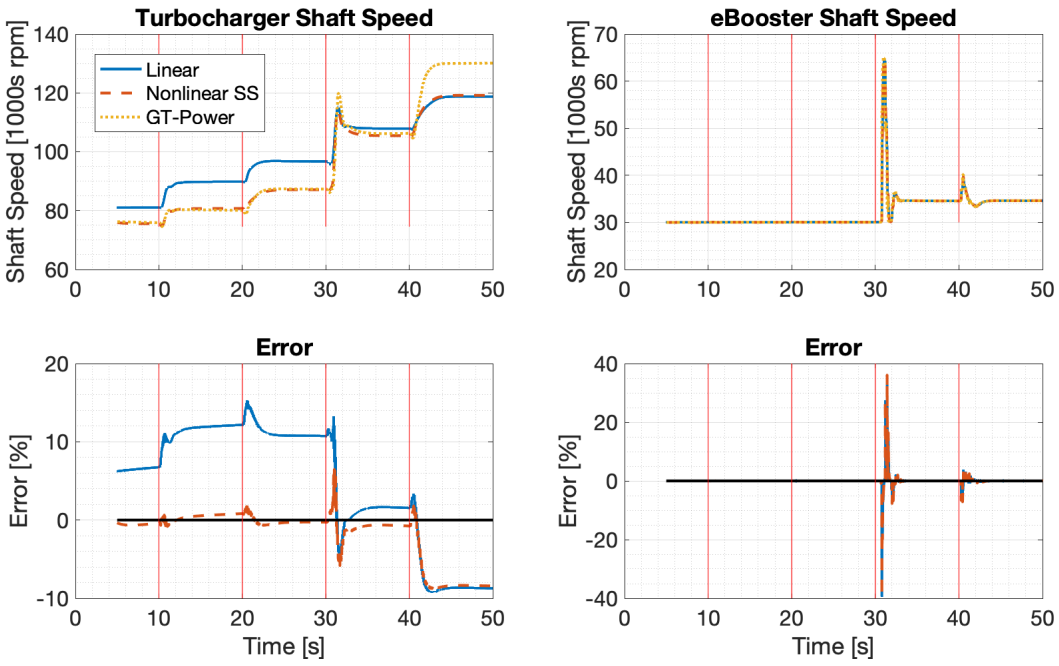

Figure 4.20. Linear model 2 turbomachinery speed states for torque steps at 1600 rpm

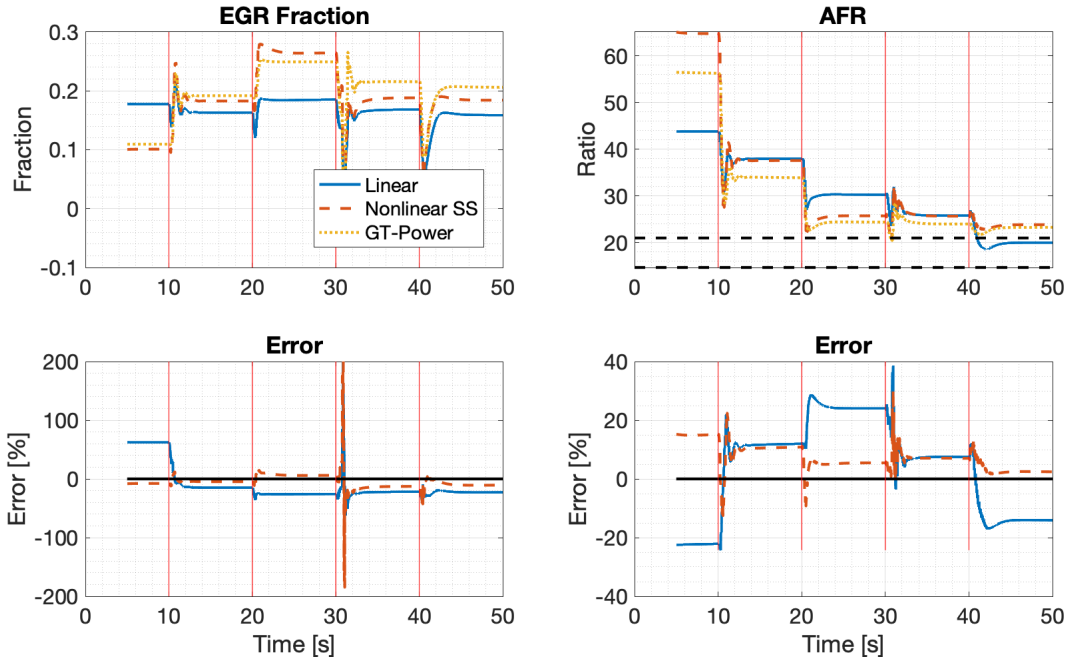

(a) EGR fraction and AFR

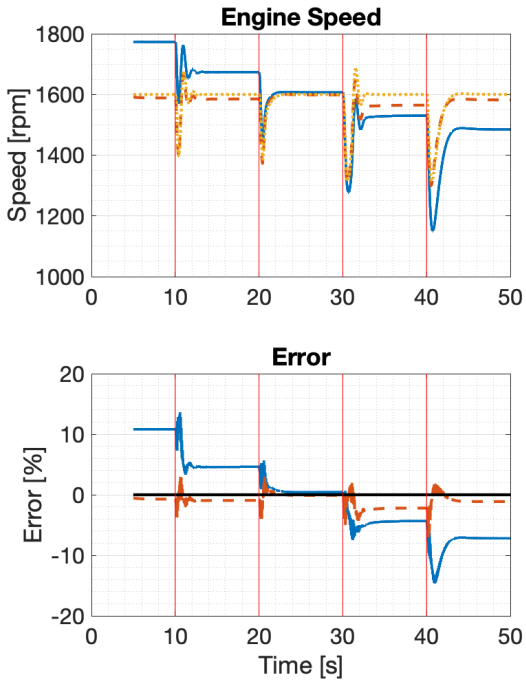

(b) Engine speed

Figure 4.21. Linear model 2 state outputs for torque steps at 1600 rpm

At 1600 rpm, linear model 1 actually performs slightly better than linear model 2. In particular, linear model 2 shows larger EGR fraction and AFR error, and linear model 2 shows significantly greater engine speed error. Also, the engine speed error trend is reversed, with linear model 1 underestimating engine speed at low torque and overestimating speed at high torque, while linear model 2 overestimates speed at low torque and underestimates speed at high torque.

Torque Steps at 1800 rpm

At 1800 rpm, the GT Power controllers command roughly the same eBooster speed and EGR valve response as in the 1600 rpm case, but the EGR valve area is no longer saturated at 500 Nm.

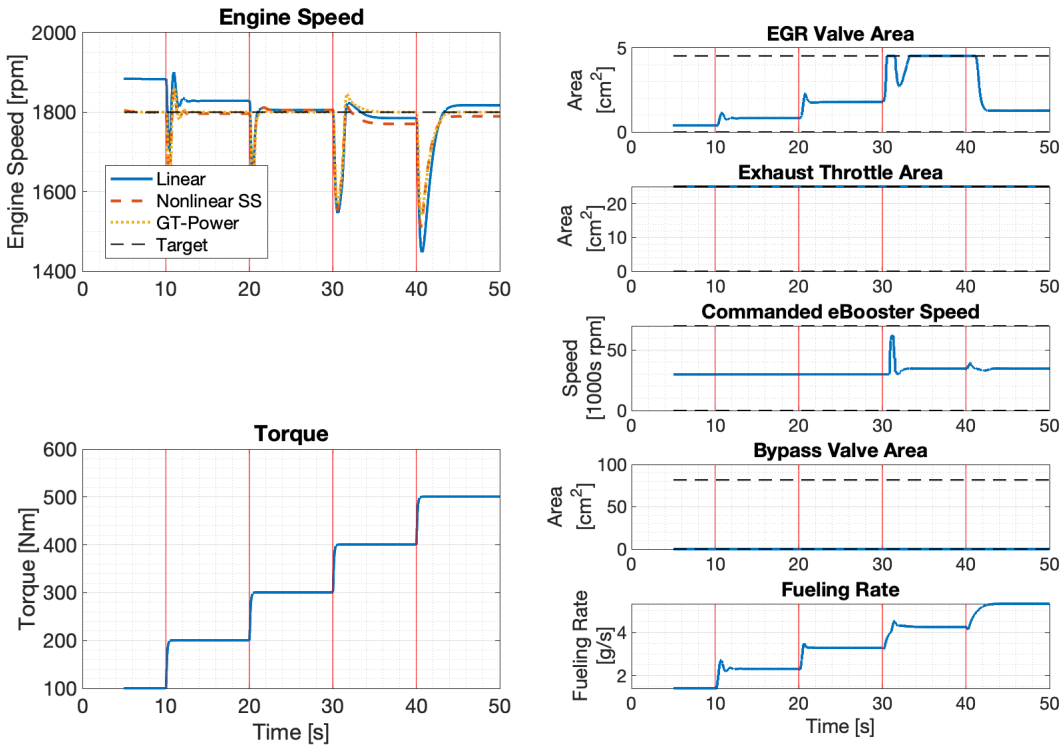

Figure 4.22. Linear model 2 speed and torque profile and actuator responses for torque steps at 1800 rpm

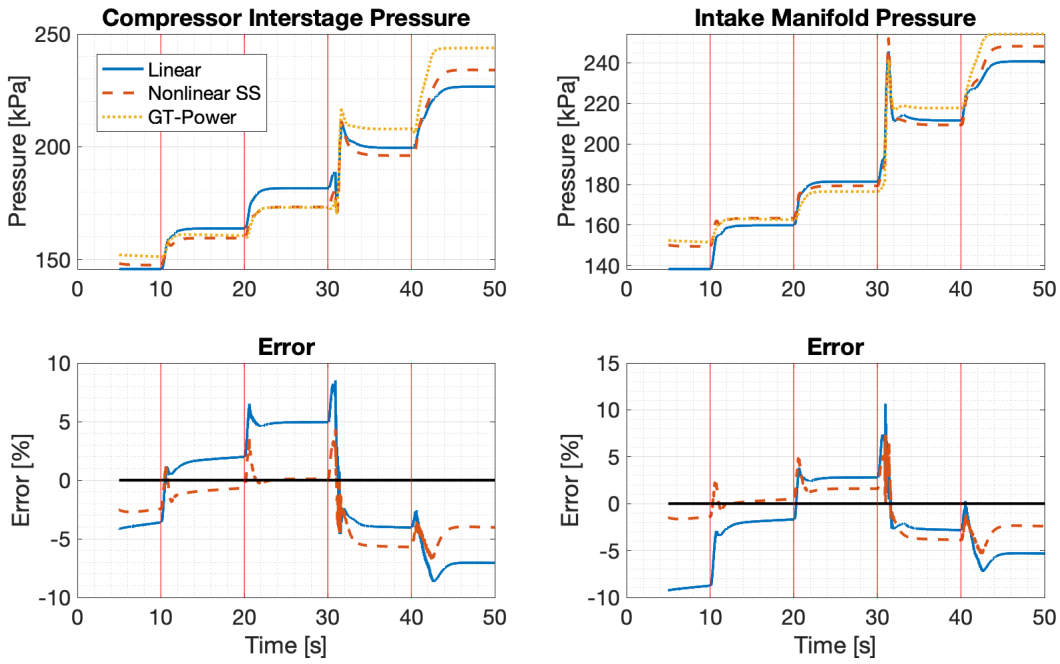

(a) Compressor interstage pressure and intake manifold pressure

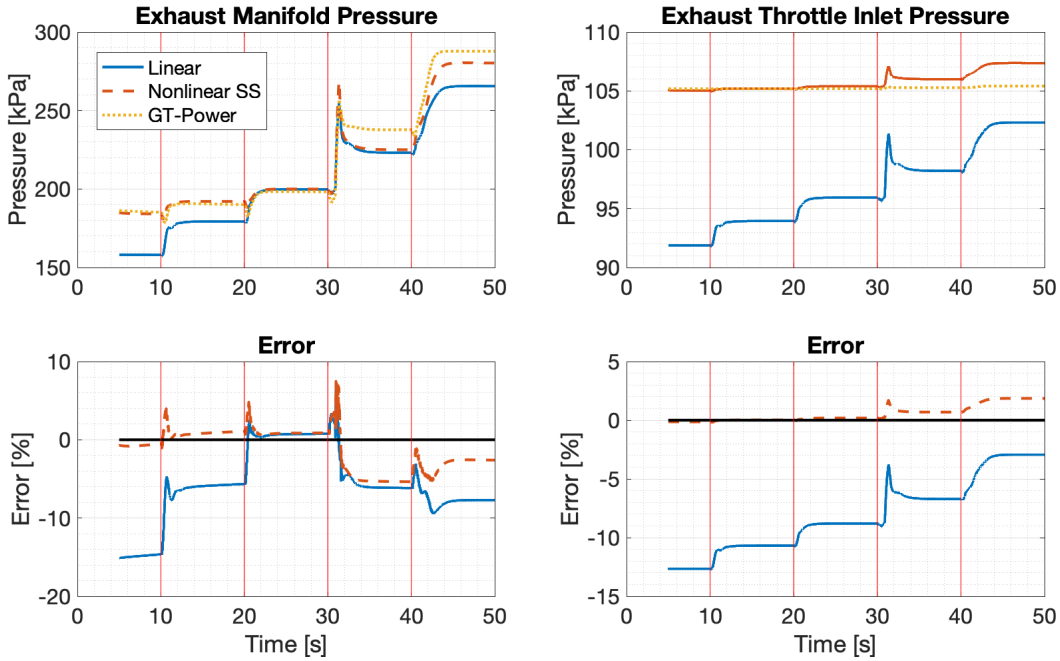

(b) Exhaust manifold and exhaust throttle inlet pressure

Figure 4.23. Linear model 2 pressure states for torque steps at 1800 rpm

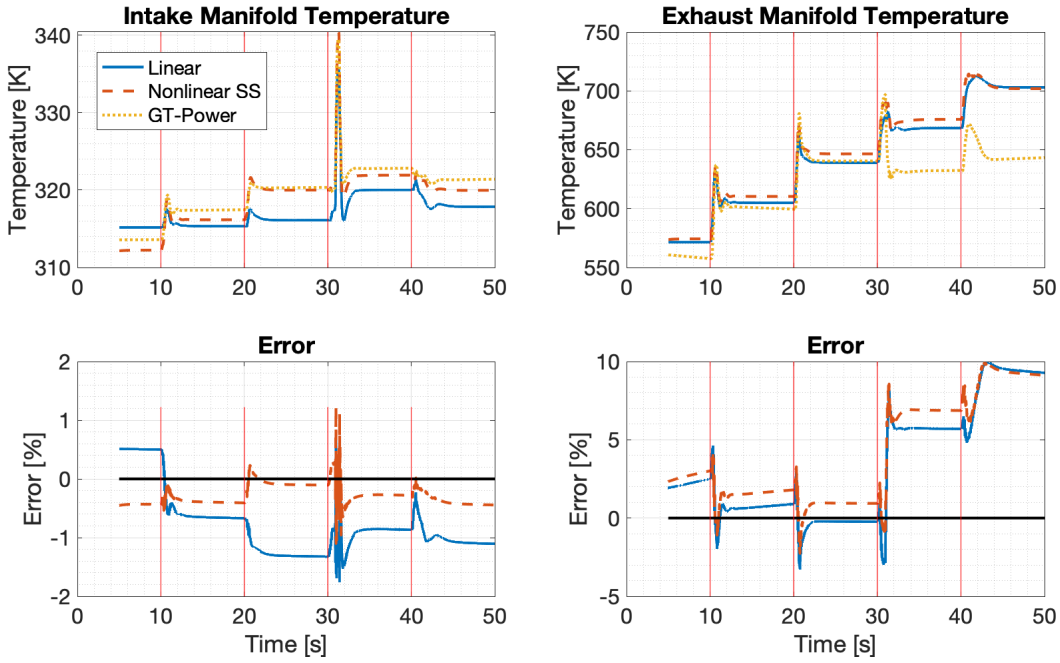

(a) Intake and exhaust manifold

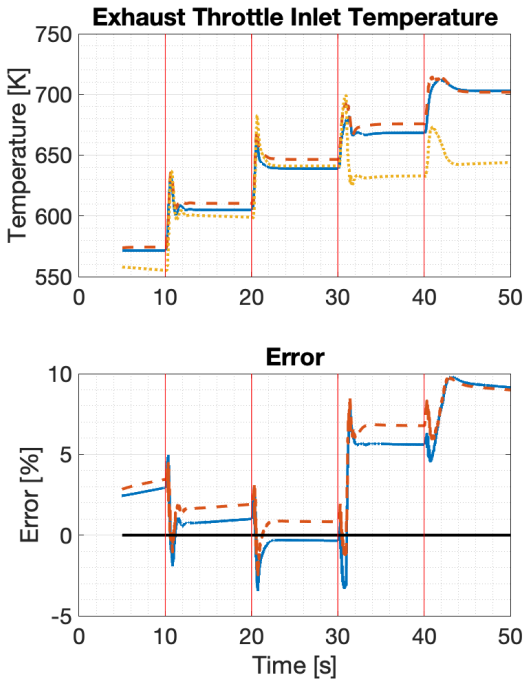

(b) Exhaust throttle inlet

Figure 4.24. Linear model 2 temperature states for torque steps at 1800 rpm

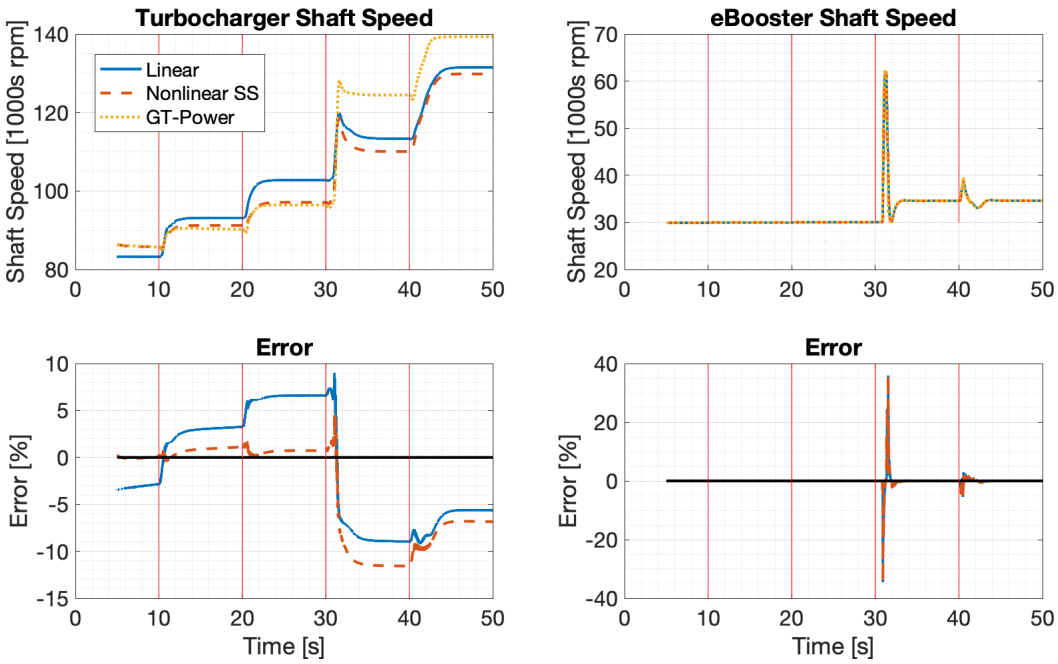

Figure 4.25. Linear model 2 turbomachinery speed states for torque steps at 1800 rpm

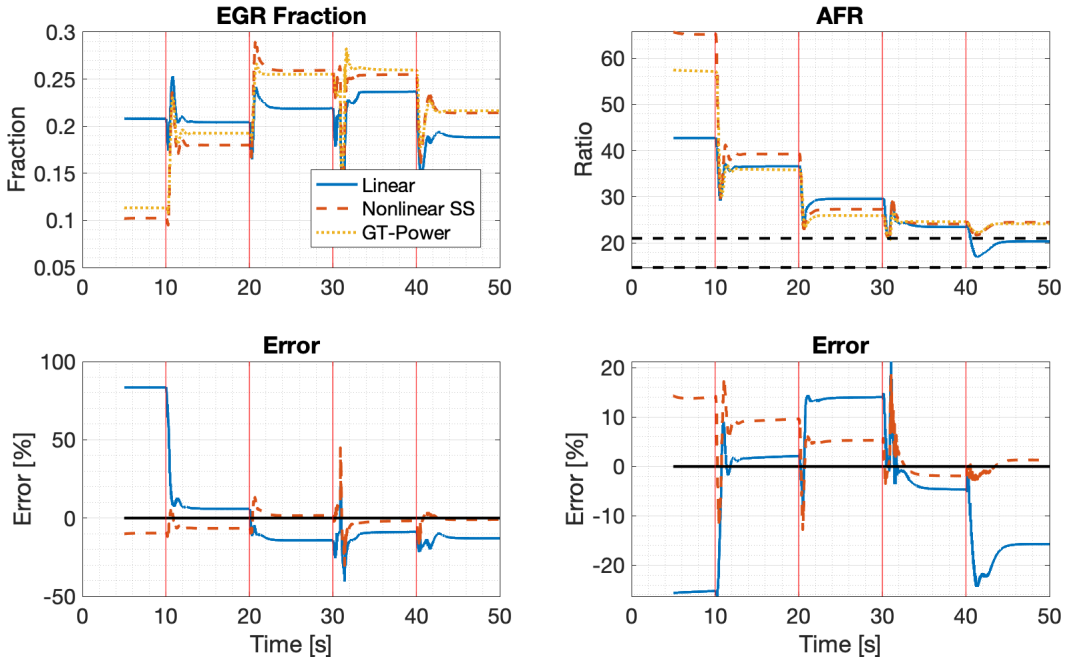

(a) EGR fraction and AFR

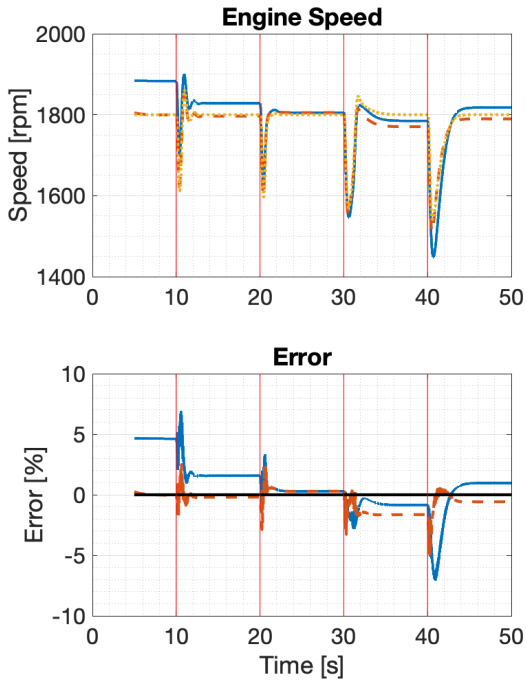

(b) Engine speed

Figure 4.26. Linear model 2 state outputs for torque steps at 1800 rpm

Improved responses are again observed as compared to the 1600 rpm case, because the engine is operating closer to the 1800 equilibrium states about which the nonlinear model is linearized. All three state outputs in particular match GT Power much more closely, but again, significant errors occur at the initial 100 Nm torque step.

Torque Steps at 2000 rpm

At 2000 rpm, the GT Power controllers no longer command any eBooster speed increase beyond 30,000 rpm, nor do they saturate the EGR valve.

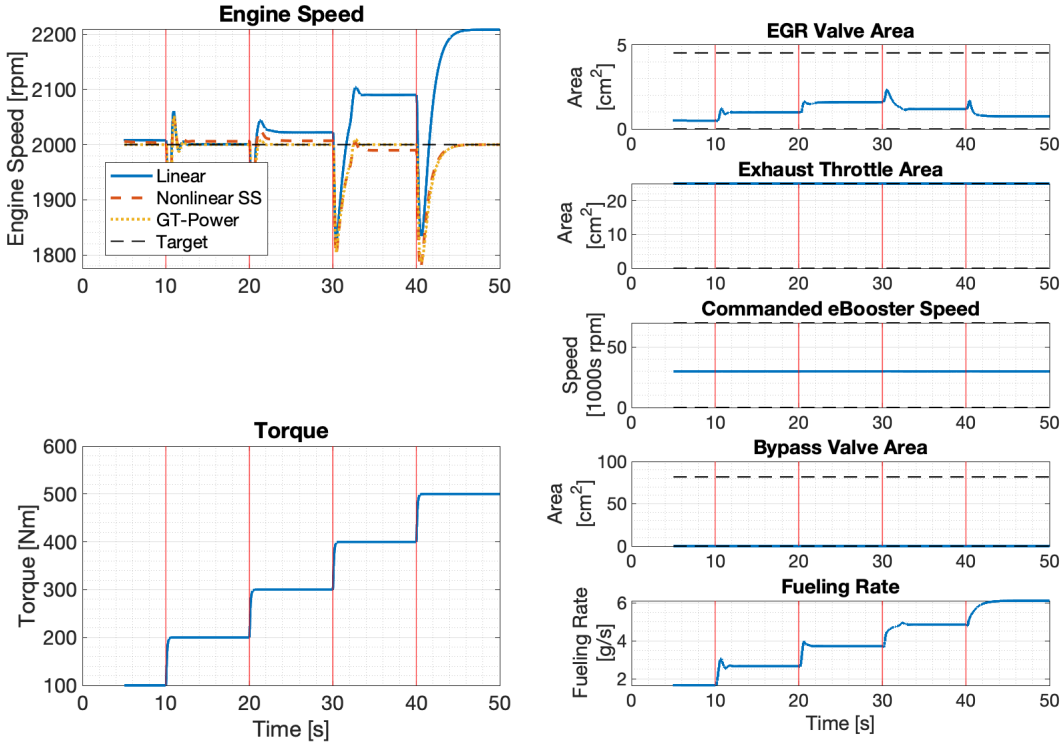

Figure 4.27. Linear model 2 speed and torque profile and actuator responses for torque steps at 2000 rpm

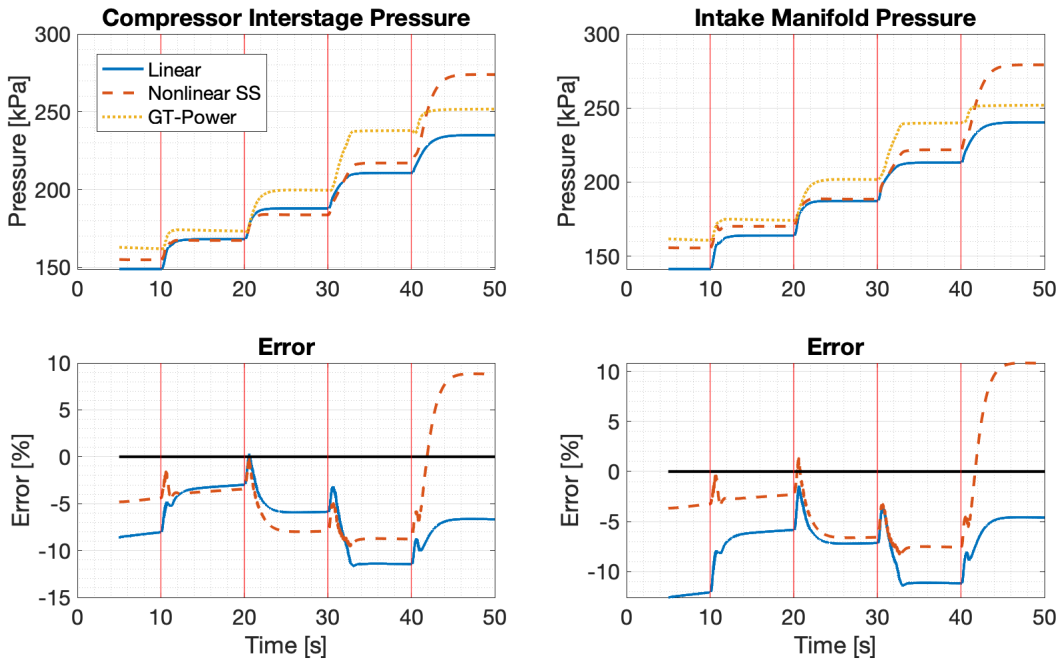

(a) Compressor interstage pressure and intake manifold pressure

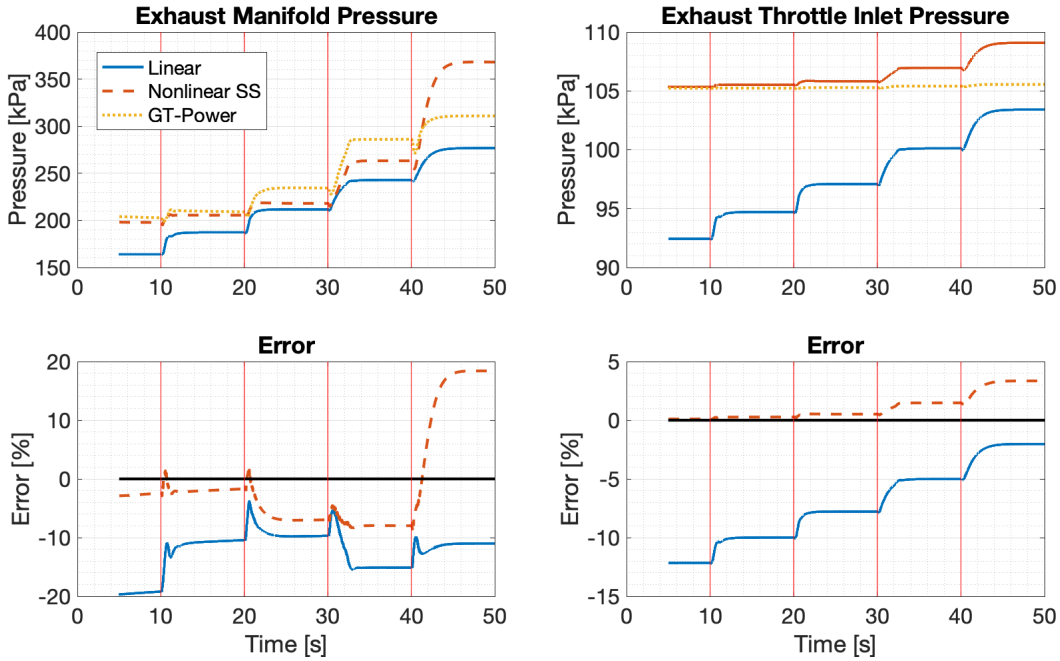

(b) Exhaust manifold and exhaust throttle inlet pressure

Figure 4.28. Linear model 2 pressure states for torque steps at 2000 rpm

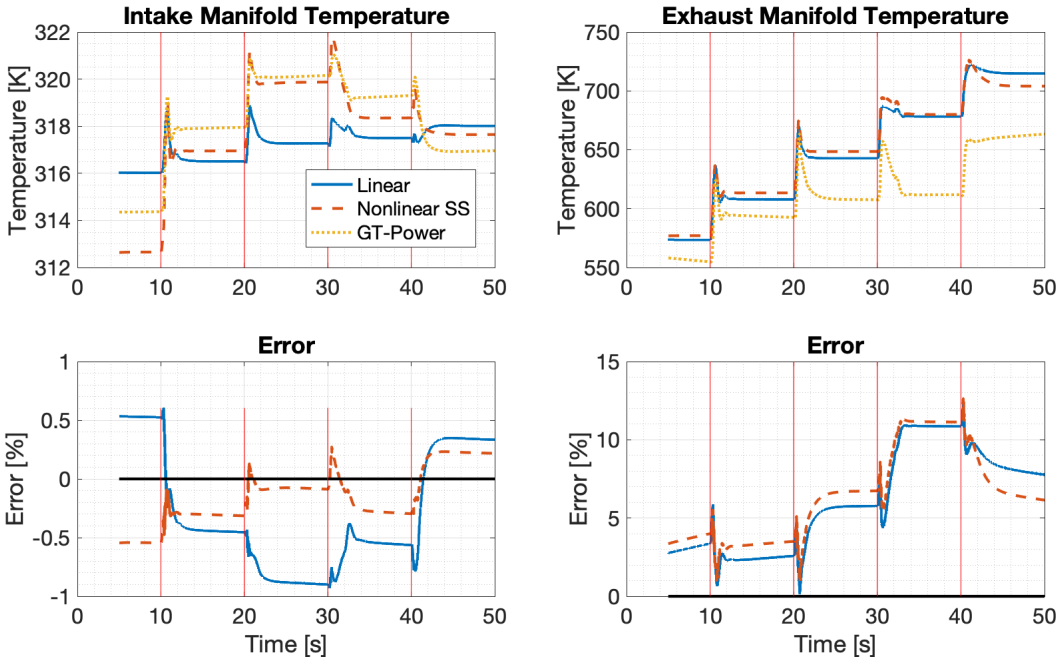

(a) Intake and exhaust manifold

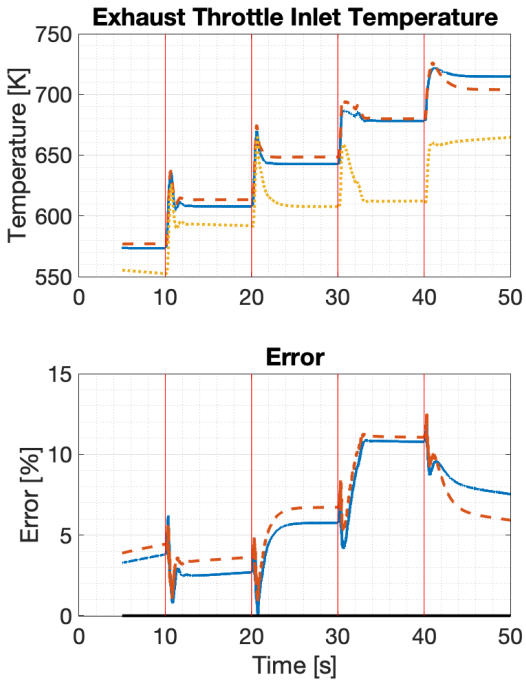

(b) Exhaust throttle inlet

Figure 4.29. Linear model 2 temperature states for torque steps at 2000 rpm

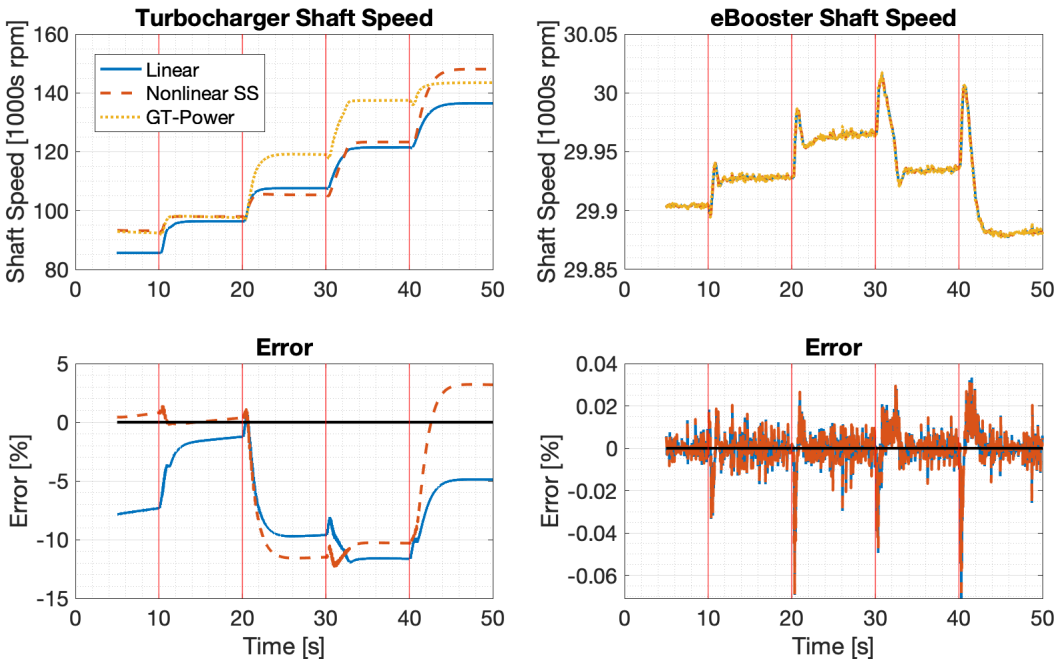

Figure 4.30. Linear model 2 turbomachinery speed states for torque steps at 2000 rpm

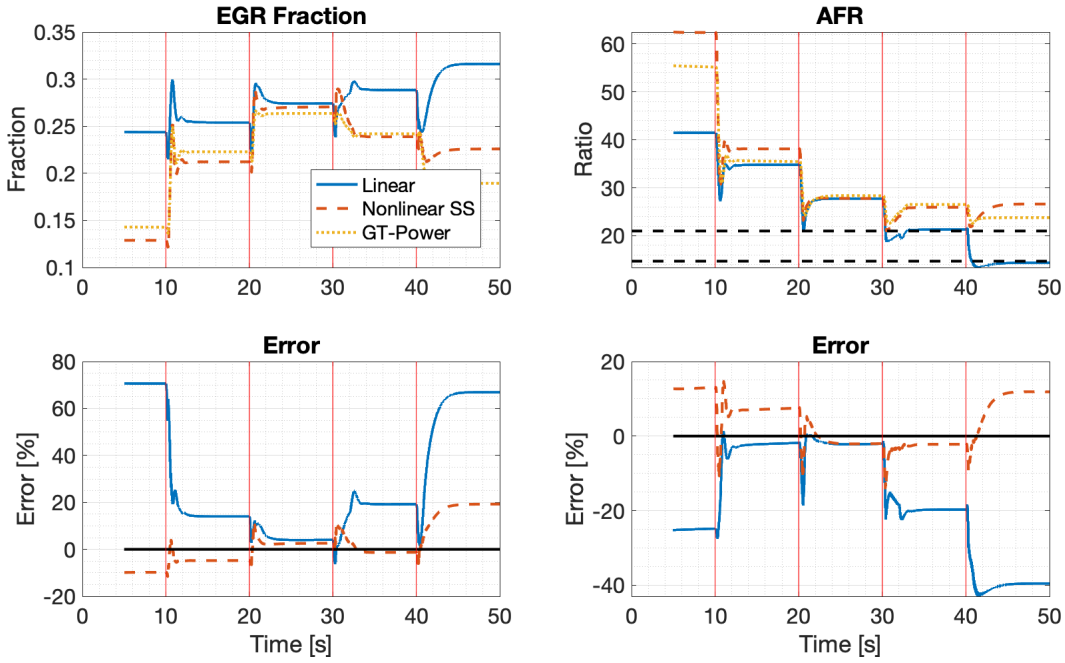

(a) EGR fraction and AFR

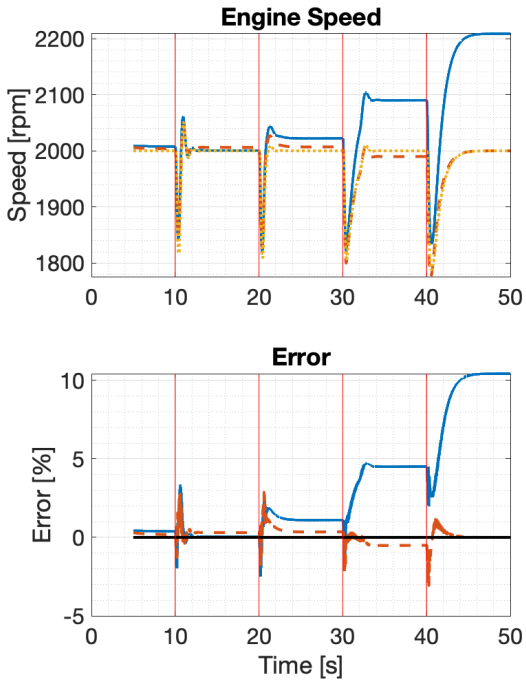

(b) Engine speed

Figure 4.31. Linear model 2 state outputs for torque steps at 2000 rpm

A notable increase in error is observed across all states and state outputs for the 2000 rpm test case. This is partly because the test case is relatively far away from the linearization equilibrium point, and partly because compressor interstage pressure is large enough to activate the wastegate. The wastegate remains shut for $P_{\text{compis}} < 245$ kPa, and the empirical relation for wastegate discharge coefficient is only valid between 245 kPa and 270 kPa, which is nonlinear saturation behaviour that cannot be captured in a linear model. As a result, significant differences in the gas exchange dynamics occur at the 500 Nm torque where the wastegate is opened. These dynamic differences explain why large steady state error is observed between 40 and 50 seconds in all state outputs for the linear model. Additionally, the same problem with large steady state error at low torque is also still observed.

4.3.3 Summary

In summary, the two linear models shown represent the engine's gas exchange dynamics reasonably well near the middle of its operating range: 1400 - 1800 rpm and 200 - 400 Nm. However outside this range, significant deviation from the GT Power truth reference response is observed because the flow rates through the engine are either higher or lower than those near the equilibria used for linearization. As a result, different linear dynamics represent the engine response in these regions.

In particular, the linear models consistently overestimate EGR fraction and underestimate AFR at low torque, indicating that in this region, the fresh air flow is consistently too low and the EGR flow is consistently too high. Consequently, when using these models for controller design, better robust performance is possible within the 1400 - 1800 rpm and 200 - 400 Nm speed and torque ranges than is possible outside them, and given the AFR and EGR fraction errors, robust performance in tracking these gas exchange parameters may not be possible for low torque conditions. However, engine speed response is reasonably good across the entire operating range, so a controller should be able to achieve robust engine speed performance across the entire operating envelope.

4.3.4 Improvements and Limitations

Two changes to the engine model may improve these EGR fraction and AFR errors. First, an eBooster map that includes data for the eBooster near and below a pressure ratio of 1 would allow better eBooster flow prediction under transient conditions. Second, using one linear model for the low torque region (100 Nm - 300 Nm) and a different linear model for the high torque region (300 Nm - 500 Nm) would allow linearization closer to the actual engine conditions present in these two regimes. However, this approach requires switching controllers based on both engine speed and load, increasing the complexity of controller and its tuning.

Significant errors were also observed from the valve flow submodel when pressure ratios were near 1, which is particularly relevant for this engine, since the bypass valve, EGR valve, and exhaust throttle all operate with small pressure differences across them. This is also why all of the validation results shown have the eBooster idling at 30,000 rpm with the bypass valve shut. The engine's gas exchange dynamics with the bypass valve open are completely different from its dynamics with the bypass valve shut, so although the nonlinear model somewhat captures this difference in dynamics, at least two different linear models are necessary to capture the region between a shut bypass valve and an open bypass valve. Furthermore, because the eBooster map does not include data for a pressure ratio near 1, which is enforced by the bypass valve when it is in any position other than fully shut, even the nonlinear model does not represent the engine's dynamics well when the bypass valve is open.

However, ultimately the bypass valve's primary purpose is to divert air around the eBooster, allowing it to idle when not needed. This behaviour can be achieved with an open loop controller that chooses the bypass valve position based on eBooster speed, so as long as the MIMO controller can effectively actuate eBooster speed to track EGR fraction and AFR, the bypass valve can be removed as an actuator from the MIMO controller. Consequently, the linear models used in control design do not need to capture the engine's response to the bypass valve.

4.4 Relative Gain Array Analysis

The relative gain array (RGA), Λ, of a linear plant model, G, is a useful tool for determining interactions between plant inputs, u, and plant outputs, y [19]. For a general linear system

$$\dot{x} = Ax + Bu + Fu_{\mathrm{d}} \tag{4.4a}$$

$$y = Cx + Du \tag{4.4b}$$

the matrix of closed loop transfer functions can be obtained from the state space realization using the complex parameter, s, as follows:

$$G(s) = C(sI - A)^{-1}B + D \tag{4.5}$$

The RGA matrix, Λ, is defined in terms of G as:

$$\Lambda(G) = G \times (G^{\dagger})^{T} \tag{4.6}$$

The pseudo inverse $G^{\dagger} = G^{H}(GG^{H})^{-1}$ is used because the linear system is non-square, with 5 inputs and 3 outputs. Here, G^{H} is the complex conjugate transpose, or Hermetian transpose of G, and "$\times$" indicates the Schur product

Each element, λ_{ij}, in Λ is a function of frequency, ω, and can be expressed as follows:

$$\lambda_{\mathrm{ij}}(\omega) = \frac{\left(\frac{y_{\mathrm{i}}}{u_{\mathrm{j}}}\right)_{u_{\mathrm{k}\neq\mathrm{j}}=0}}{\left(\frac{y_{\mathrm{i}}}{u_{\mathrm{j}}}\right)_{y_{\mathrm{k}\neq\mathrm{i}}=0}} \tag{4.7}$$

To provide an intuitive control explanation for the meaning of λ_{ij}, the numerator is the ratio of output i to input j, $y_{\mathrm{i}}/u_{\mathrm{j}}$, when all other *inputs*, $u_{\mathrm{k}\neq\mathrm{j}}$, are zero. The denominator is the ratio of output i to input j, $y_{\mathrm{i}}/u_{\mathrm{j}}$, when all other inputs, $u_{\mathrm{k}\neq\mathrm{j}}$ perfectly control the system to make all other *outputs*, y_{k}, zero. As a result, λ_{ij} is a measure of the closed loop gain from u_{j}

to y_i (input u_j's ability to effect output y_i) at two extremes: zero control effort from other actuators (numerator) and maximum influence from other actuators (denominator).

In general, λ_{ij} is a complex parameter that depends on frequency, so its magnitude and phase can be plotted as functions of frequency. The following conclusions can then be drawn about a u_j - y_i pairing at each frequency:

1. $|\lambda_{ij}| = 0$: Input u_j has no influence on output y_i.

2. $0 < |\lambda_{ij}| < 1$: The closed loop gain from input u_j to output y_i increases as other actuators are engaged to control other outputs. This can indicate that oscillations or even instability may occur.

3. $|\lambda_{ij}| = 1$: The closed loop gain from input u_j to output y_i is independent of the other actuators and outputs. This indicates that the response of y_i to u_j will not change as other actuators are engaged to control other outputs.

4. $|\lambda_{ij}| > 1$: The closed loop gain from input u_j to output y_i decreases as other actuators are engaged to control other outputs. This can indicate sluggish control response with this pairing, as well as sensitivity to model uncertainty.

5. $\angle\lambda_{ij} < -90°$ or $\angle\lambda_{ij} > 90°$: The closed loop gain from input u_j to output y_i switches sign when other actuators are engaged to control other outputs, causing system instability. This is equivalent to $\mathcal{R}\mathrm{e}(\lambda_{ij}) < 1$.

To summarize, λ_{ij} with magnitude close to 1 and phase close to 0° indicates a completely decoupled input-output pair amenable to independent SISO control loops.

As an analysis tool for linear systems used in $\mathcal{H}_\infty$ MIMO controller development however, the RGA can inform the designer of three aspects of a system's behaviour. First, as $|\lambda_{ij}|$ moves farther away from 1, system inputs and outputs become more coupled, and coordinated MIMO control becomes more important. Second, the outputs' responses to inputs can inform the tuning of weighting functions for actuator inputs and system outputs. Finally, the outputs' sensitivity to inputs provides a method of confirming that the linear model represents the plant's response to actuators as expected.

In the following sections, the RGA magnitude and phase are plotted for each pair of inputs and outputs as functions of frequency from 0 to 30 rad/s (approximately 5 Hz), where $\omega = 0$ represents system behaviour at steady state. This frequency range corresponds to the range where gas exchange control is most important and achievable. The fueling rate is omitted from the EGR fraction and AFR plots, because the magnitude and phase of its interaction with these outputs is zero in all cases.

4.4.1 RGA Analysis for Linear Model 1

The RGA plots that relate EGR fraction and AFR pairing with the four gas exchange actuators are shown in Figures 4.32 and 4.33, and several notable observations can be made. First, the EGR valve appears to have no influence on EGR fraction or AFR, which is potentially problematic for control. However, in simulations from both the nonlinear state space model and the GT Power model, at lower engine speeds such as the 1400 rpm point used to obtain this linearization, the engine struggles to drive sufficient EGR because of a very small pressure drop from the exhaust manifold to the intake manifold. This problem is exacerbated by the eBooster, which can cause cause reversed flow through the EGR valve for some conditions.

Second, each of the remaining three actuators shows similar magnitude with respect to EGR fraction and AFR, with the exhaust throttle closest to one for $\omega = 0$. This indicates that the exhaust throttle is the best pairing for both EGR fraction and AFR control at steady state, and that the eBooster and bypass valve can influence these parameters, but are slightly more sensitive to uncertainty. An intuitive understanding of the engine also corroborates the conclusion that at these low engine speeds, the exhaust throttle is an effective tool for driving EGR, because the exhaust throttle can increase the pressure drop across the EGR valve by increasing pressure in the exhaust manifold.

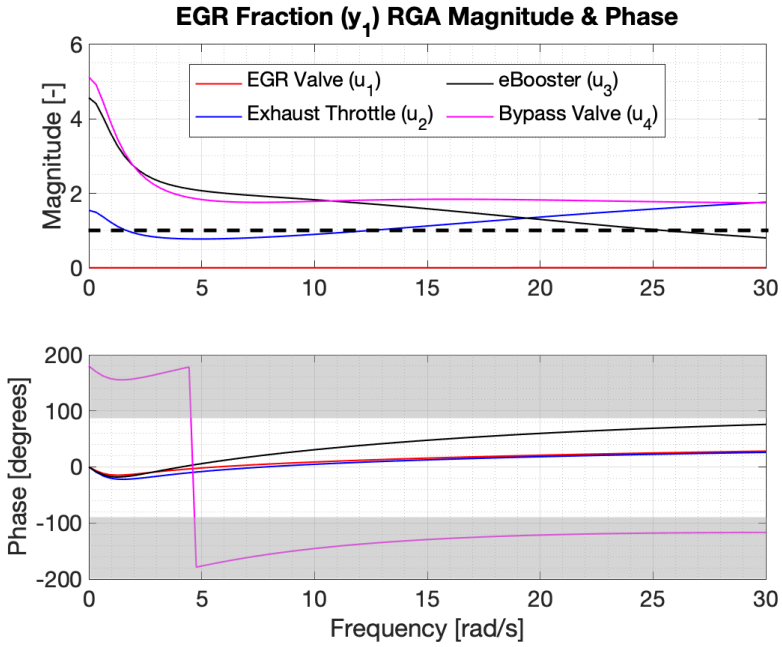

Figure 4.32. Linear model 1 RGA element analysis for EGR fraction output

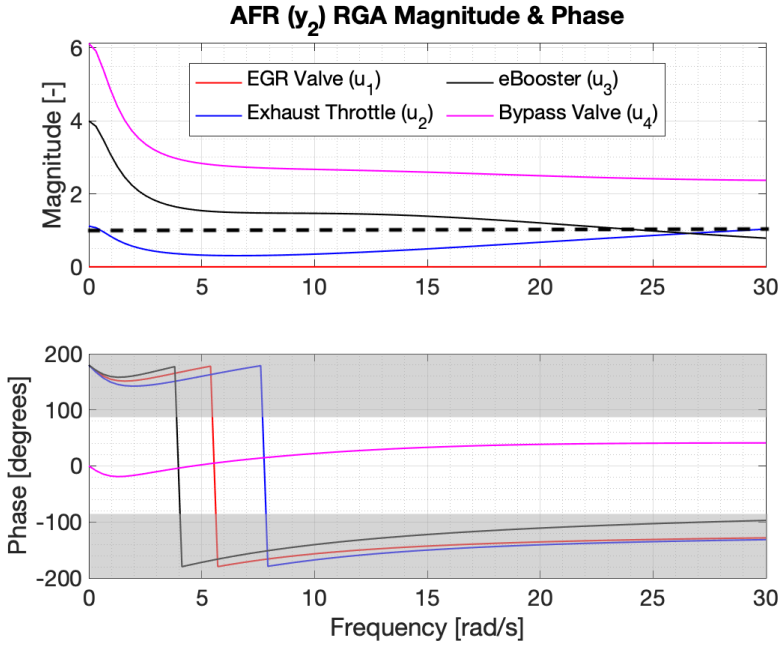

Figure 4.33. Linear model 1 RGA element analysis for AFR output

Third, the bypass valve has a phase near 180° when paired with EGR fraction, which indicates that its influence on EGR fraction can reverse depending on the operation of other actuators. This behaviour is expected, because the bypass valve's effect on fresh air flow rate is dependent entirely on the eBooster. If the eBooster is at idle, opening the bypass valve will increase fresh air flow, but if the eBooster is near its maximum speed, opening the bypass valve will allow fresh air to flow backwards through it, reducing the fresh air flow to the intake manifold and the eBooster's overall effectiveness.

Finally, the eBooster, EGR valve, and exhaust throttle all show phases near 180° when paired with AFR. This is expected for the eBooster and EGR valve, because their influence on fresh air flow into the engine changes depending on every other actuator. For the exhaust throttle however, this behavior is unexpected and may indicate a problem in the way the linear model responds to exhaust throttle actuation.

The RGA plot relating all actuators to engine speed is shown in Figure 4.34, and it is clear that fueling rate is the preferred actuator to command engine speed at all frequencies. This is expected, as the engine's speed is not dependent on air flow, as long as air flow is sufficient for combustion.

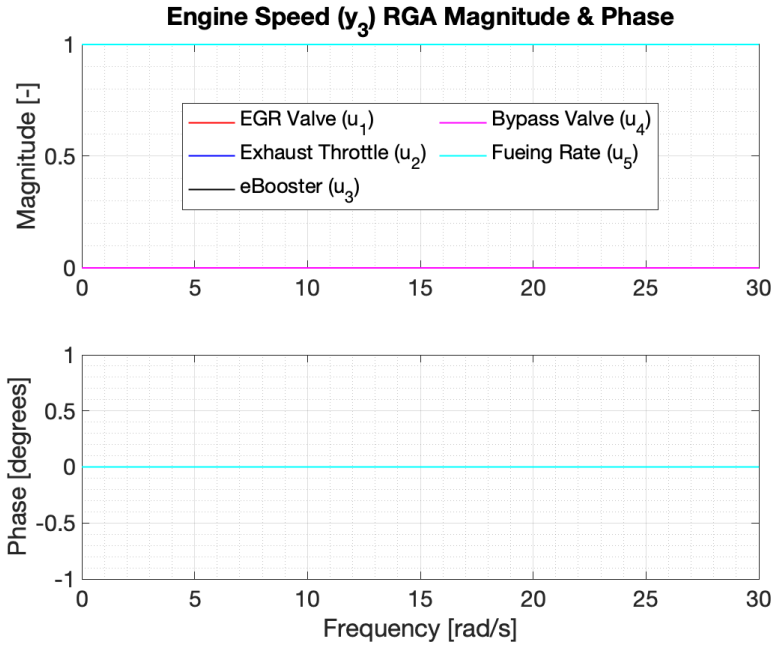

Figure 4.34. Linear model 1 RGA element analysis for engine speed output

4.4.2 RGA Analysis for Linear Model 2

Similar trends are noted in the RGA plots for the system linearized around an 1800 rpm equilibrium, but two minor differences are notable from the EGR fraction and AFR pairings shown in Figures 4.35 and 4.36. In both pairings, the EGR valve magnitude is larger than its magnitude for the first linear model, which is expected, because the engine is more capable of driving EGR at higher engine speeds.

Second, the eBooster and bypass valve show lower magnitudes, indicating that they are less sensitive to uncertainty overall. This is because the pressure drop across the EGR valve tends to be larger in general, so the EGR flow measurement is less sensitive to uncertainty in other areas of the system. Additionally, because the higher gas flow rate through the engine spins the turbocharger faster, the eBooster's overall influence on gas exchange dynamics is less pronounced than for the lower engine speed range represented in the first linear model.

The RGA plot relating all actuators to engine speed is shown in Figure 4.37, and fueling rate is again the obvious pairing to control the engine speed output.

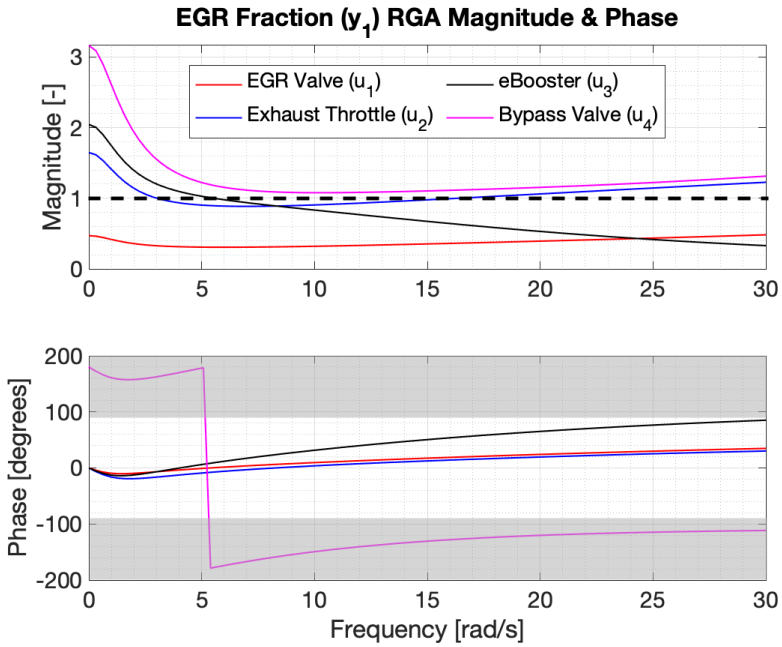

Figure 4.35. Linear model 2 RGA element analysis for EGR fraction output

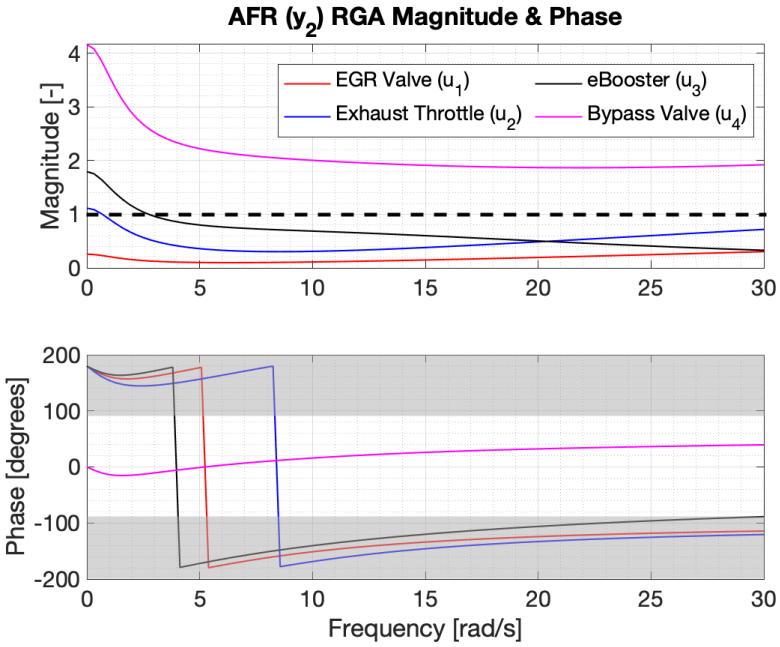

Figure 4.36. Linear model 2 RGA element analysis for AFR output

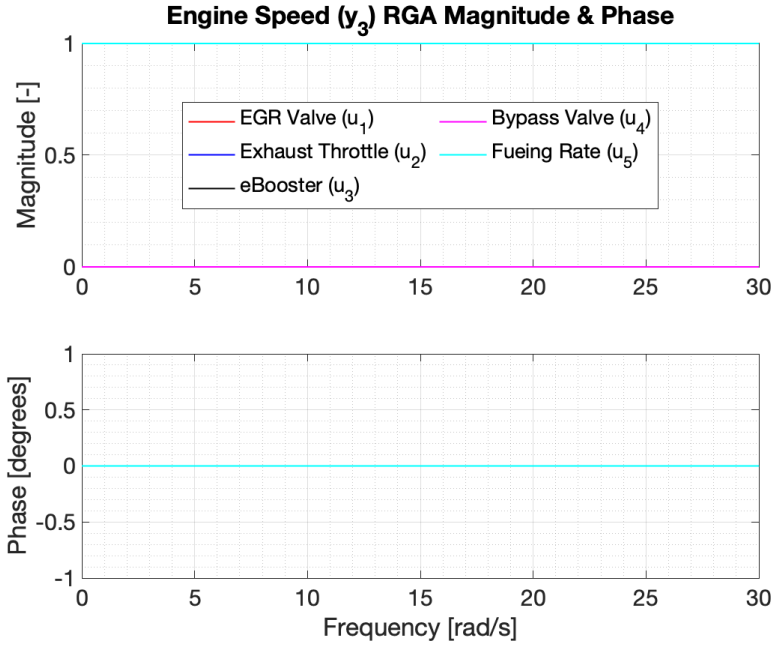

Figure 4.37. Linear model 2 RGA element analysis for engine speed output

4.4.3 Summary

The RGA analysis presented indicates that for EGR fraction and AFR control, no single actuator is an obvious choice for SISO control. Due to close coupling among these gas exchange parameters and the EGR valve, exhaust throttle, eBooster, and bypass valve, as well as the variation in pairing behaviour with frequency, this set of inputs and outputs is an excellent candidate for a coordinated MIMO control approach.

In contrast, fueling rate and engine speed appear to be an ideal pairing for SISO control, as fueling rate does not significantly influence EGR fraction and AFR, and the other actuators do not influence engine speed. However on the actual engine, AFR limits effect the allowable fueling rate, and a linear model cannot capture these inherently nonlinear considerations. As a result, during an aggressive torque step from 100 Nm to 500 Nm for example, the controller must increase airflow before or simultaneous to a fueling increase to avoid dropping AFR below an allowable bound, and this coupling, while not captured in the RGA analysis of the linear models, is more effectively handled when the controller can command fueling in conjunction with the gas exchange process.

Consequently, this analysis indicates that a coordinated MIMO controller is likely to be superior to independent SISO control loops for performance in tracking all three outputs, because the MIMO controller can manage both the coupling among actuators, and the variations in pairing behaviour with frequency.

5. CONCLUSIONS AND FUTURE WORK

5.1 Summary

In this thesis, two methods of hybridization are discussed: a series electric powertrain implemented in an on-highway class 8 truck, and a four cylinder diesel engine with an electrically driven supercharger for a hybrid wheel loader.

5.1.1 Series Hybrid Electric Powertrain Analysis for Class 8 Truck

The power flows in the series electric hybrid powertrain are analyzed to confirm that electrical components operate as expected, identify mechanisms through which the hybrid drivetrain can provide efficiency improvements over a conventional drivetrain, and demonstrate that potential efficiency improvements of the hybrid drivetrain merit further development. To this end, power flow data to and from the generator, battery and motor are examined from test data over highway routes on I-75 between Florence and Lexington, KY and on I-74 and I-70 near Indianapolis. From these data, the total energy contributions provided to and from each component are calculated and used to study battery operation, power electronics efficiency, regeneration energy capture percentage, and the fraction of drive energy provided by regenerative braking.

The power electronics are found to operate between 82% and 92% efficiency, which is the expected range for power electronics of this type. The battery efficiency is not explicity determined, but testing results show clear signs of battery wear that can reduce its ability to store energy with minimal thermal losses. However, it is still able to capture nearly all of the available regenerative braking energy theoretically available according to the drive profile test data and a simple physical model of the truck. No exact recapture percentage is identified, because unmeasured environmental factors such as wind and low temperatures affect these results significantly, but the model predicts that the recapture percentage is near 100% on average. Additionally, analysis indicates that during testing, between 2% and 12% of the total drive energy required to propel the vehicle comes from regenerative braking depending on the route grade and drive profile, and that improvements in rolling resistance

and aerodynamic drag consistent with a more modern truck could increase this percentage to between 8% and 18%.

5.1.2 Control Oriented Modeling of Diesel Engine

A physically-based mean value engine model is also developed for control of a turbocharged diesel engine with a high pressure EGR loop, an exhaust throttle, and an electric supercharger (eBooster) downstream of the turbocharger compressor. A nonlinear state space model with ten states is developed to model the effects of the EGR valve, exhaust throttle, eBooster, eBooster bypass valve, and fueling rate on EGR fraction, AFR, and engine speed, and this model is linearized about two operating points to generate two linear models which represent the engine over its entire operating range. The linear and nonlinear models are validated against the truth reference GT Power engine model, and relative gain array analysis is performed on the linear models which indicates that the engine exhibits significant coupling dynamics among actuators and outputs. As a result, it is concluded that that a SISO control approach is unsuitable for tracking EGR fraction and AFR, and that the planned MIMO control approach is necessary to take full advantage of the electrified air handling system to maximize the engine's transient performance.

5.2 Future Work

Both applications discussed are part of ongoing development efforts to reduce fuel consumption in vehicles with hybrid powertrains, and both applications require additional work at the supervisory control level.

5.2.1 Series Electric Hybrid Powertrain Analysis for Class 8 Truck

The architecture of the supervisory controller managing power flows in the hybrid class 8 truck powertrain was not accessible for the analysis presented, so further work to optimize the engine and battery operation will likely further increase its potential for fuel savings. Specifically, providing the supervisory controller with some indication of its future drive profile and power needs allows it to optimize power drawn from the genset to keep the IC

engine near its minimum BSFC while still providing sufficient power over the operational cycle. This optimization can also allow the controller to take advantage of a new power-optimized battery which is planned for the next iteration of the powertrain.

5.2.2 Control Oriented Modeling of Diesel Engine

The diesel engine modeled is ultimately designed as the replacement for a larger engine in a series electric hybrid wheel loader, and as such, the goal of the engine modeling and robust MIMO control development is to allow the engine to meet the performance goals of the larger engine it replaces, while reducing fuel consumption and tracking EGR fraction, AFR, and engine speed targets. The supervisory controller in this powertrain is also an effective tool for reducing fuel consumption and helping the engine meet these targets, because it can manage both the engine's steady state operating point and the severity of transient speed and load changes. Rule-based control strategies are an effective way of managing power flows within a series hybrid powertrain, because they are intuitive to design and tune, so initial efforts will focus on developing a rule-based supervisory controller, but additional work will focus on an optimization-based control strategy than can optimize power flows to and from the generator, battery, and motor, ultimately yielding the best fuel economy for the new drivetrain.

REFERENCES

[1] S. H. Rayasam, "Evaluation of fuel savings due to powertrain electrification of class 8 trucks," Master's thesis, Purdue University, 2018.

[2] C. Mi and M. Masrur, *Hybrid Electric Vehicles: Principles and Applications with Practical Perspectives, Second Edition*. John Wiley & Sons Ltd, Oct. 2017.

[3] H. Zhao, A. Burke, and L. Zhu, "Analysis of class 8 hybrid-electric truck technologies using diesel, lng, electricity, and hydrogen, as the fuel for various applications," presented at the 2013 World Electric Vehicle Symposium and Exhibition, Nov. 2013.

[4] L. Johannesson, N. Murgovski, E. Jonasson, J. Hellgren, and B. Egardt, "Predictive energy management of hybrid long-haul trucks," *Control Engineering Practice*, vol. 41, pp. 83–97, 2015.

[5] BorgWarner. (2021), [Online]. Available: https://www.borgwarner.com/technologies/electric-boosting-technologies.

[6] D. Zhao, E. Winward, Z. Yang, R. Stobart, B. Mason, and T. Steffen, "An integrated framework on characterization, control, and testing of an electrical turbocharger assist," *IEEE transactions on industrial electronics (1982)*, vol. 65, no. 6, pp. 4897–4908, 2018.

[7] M. Alshammari, F. Alshammari, and A. Pesyridis, "Electric boosting and energy recovery systems for engine downsizing," *Energies (Basel)*, vol. 12, no. 24, p. 4636, 2019.

[8] P. Dimitriou, R. Burke, Q. Zhang, C. Copeland, and H. Stoffels, "Electric turbocharging for energy regeneration and increased efficiency at real driving conditions," *Applied sciences*, vol. 7, no. 4, p. 350, 2017.

[9] B. Xiao, J. H. Buckland, and A. Karnik, "Frequency separation control of series sequential boosting system with electric supercharger and turbocharger," in *ASME 2017 Dynamic Systems and Control Conference, DSCC 2017*, vol. 3, 2017, ISBN: 0791858294.

[10] S. Baek, H. Lee, and K. Lee, "Fuel efficiency and exhaust characteristics of turbocharged diesel engine equipped with an electric supercharger," *Energy (Oxford)*, vol. 214, p. 119 049, 2021.

[11] C. Wu, K. Song, S. Li, and H. Xie, "Impact of electrically assisted turbocharger on the intake oxygen concentration and its disturbance rejection control for a heavy-duty diesel engine," *Energies (Basel)*, vol. 14, no. 15, p. 3014, 2019.

[12] K. Ekberg and L. Eriksson, "Improving fuel economy and acceleration by electric turbocharger control for heavy duty long haulage," in *IFAC PapersOnLine*, vol. 50, Elsevier Ltd, 2017, pp. 11 052–11 057.

[13] N. Terdich, R. F. Martinez-Botas, A. Romagnoli, and A. Pesiridis, "Mild hybridization via electrification of the air system: Electrically assisted and variable geometry turbocharging impact on an off-road diesel engine," *Journal of engineering for gas turbines and power*, vol. 136, no. 3, 31 703–np, 2014.

[14] A. Jain, T. Nueesch, C. Naegele, P. M. Lassus, and C. H. Onder, "Modeling and control of a hybrid electric vehicle with an electrically assisted turbocharger," *IEEE transactions on vehicular technology*, vol. 65, no. 6, pp. 4344–4358, 2016.

[15] D. Zhao, R. Stobart, and B. Mason, "Real-time energy management of the electric turbocharger based on explicit model predictive control," *IEEE transactions on industrial electronics (1982)*, vol. 67, no. 4, pp. 3126–3137, 2020.

[16] J. Villegas, B. Gao, K. Svancara, W. Thornton, and J. Parra, "Real-time simulation and control of an electric supercharger for engine downsizing," in *2011 IEEE Vehicle Power and Propulsion Conference*, IEEE, 2011, pp. 1–6, ISBN: 9781612842486.

[17] S. Ebbesen, M. Salazar, P. Elbert, C. Bussi, and C. H. Onder, "Time-optimal control strategies for a hybrid electric race car," *IEEE transactions on control systems technology*, vol. 26, no. 1, pp. 233–247, 2018.

[18] L. Eriksson and L. Nielsen, *Modeling and Control of Engines and Drivelines*. John Wiley & Sons Ltd, 2014.

[19] S. Skogestad and I. Postlethwaite, *Multivariable Feedback Control - analysis and design*, 2nd ed. John Wiley & Sons Ltd, 2005.

[20] D. Gu, P. Petkov, and M. Konstantinov, *Robust Control Design with MATLAB, Second Edition*. Springer, 2013.

[21] S.-Y. Cheong and M. G. Safonov, "Slow-fast controller decomposition bumpless transfer for adaptive switching control," *IEEE transactions on automatic control*, vol. 57, no. 3, pp. 721–726, 2012.

[22] H. Mahabadipour, K. Srinivasan, S. Krishnan, and S. Subramanian, "Crank angle-resolved exergy analysis of exhaust flows in a diesel engine from the perspective of exhaust waste energy recovery," *Applied energy*, vol. 216, pp. 31–44, 2018.

[23] M. Karlsson, K. Ekholm, P. Strandh, R. Johansson, and P. Tunestål, "Multiple-input multiple-output model predictive control of a diesel engine," *IFAC Proceedings Volumes*, vol. 43, no. 7, pp. 131–136, 2010.

[24] A. P. Vora, X. Jin, V. Hoshing, T. Saha, G. Shaver, S. Varigonda, O. Wasynczuk, and W. E. Tyner, "Design-space exploration of series plug-in hybrid electric vehicles for medium-duty truck applications in a total cost-of-ownership framework," *Applied energy*, vol. 202, no. C, pp. 662–672, 2017.

[25] V. Hoshing, A. Vora, T. Saha, X. Jin, G. Shaver, O. Wasynczuk, R. E. García, and S. Varigonda, "Comparison of economic viability of series and parallel phevs for medium-duty truck and transit bus applications," *Proceedings of the Institution of Mechanical Engineers. Part D, Journal of automobile engineering*, vol. 234, no. 10-11, pp. 2458–2472, 2020.

[26] T. Park and H. Lee, "Optimal supervisory control strategy for a transmission-mounted electric drive hybrid electric vehicle," *International journal of automotive technology*, vol. 20, no. 4, pp. 663–677, 2019.

[27] L. Serrao, A. Sciarretta, O. Grondin, A. Chasse, Y. Creff, D. Di Domenico, P. Pognant-Gros, C. Querel, and L. Thibault, "Open issues in supervisory control of hybrid electric vehicles: A unified approach using optimal control methods," *Oil & gas science and technology*, vol. 68, no. 1, pp. 23–33, 2013.

[28] D. Velmurugan, D. Lundberg, and T. McKelvey, "Look ahead based supervisory control of a light duty diesel engine," in *IFAC-PapersOnLine*, vol. 51, 2018, pp. 454–459.

[29] E. Koeberlein, L. Kocher, D. V. Alstine, K. Stricker, and G. Shaver, "Physics based control oriented modeling of exhaust gas enthalpy for engines utilizing variable valve actuation," in *ASME 2011 Dynamic Systems and Control Conference and Bath/ASME Symposium on Fluid Power and Motion Control, Volume 2*, ASMEDC, 2011, pp. 627–634.

[30] K. Stricker, L. Kocher, E. Koeberlein, D. V. Alstine, and G. Shaver, "Turbocharger map reduction for control-oriented modeling," *Journal of dynamic systems, measurement, and control*, vol. 136, no. 4, 2014.